High Resolution Simulations of Galactic Cannibalism

by

Timothy W. Connors

A Dissertation
Presented in fulfillment of the requirements
for the degree of
Doctor of Philosophy
at Swinburne University Of Technology

2008

Abstract

Throughout this dissertation, we will use numerical simulations to probe our understanding of Hierarchical Clustering within the local Universe. We make use of the chemodynamical simulation code GCD+, to simulate several high-resolution cosmological and galactic scale simulations. We describe a suite of analysis software used to transform the simulation data into the observer's plane, and apply it on a set of simulations that probe nearby objects being cannibalised by our own Milky Way Galaxy.

We first apply our codes to the interacting Magellanic and Milky Way system, to show that the Magellanic Stream is the result of the Magellanic Clouds being torn apart by the tidal forces between them and the Milky Way. To do this, we find the set of parameters that determine a best-fit model to the observed stream, and highlight how these parameters affect the final model. We find in particular, that the disc of the Small Magellanic Cloud is required to be larger than previous studies have shown, and we cast doubt on some recent measurements of the mass of the Large Magellanic Cloud. We also make the successful prediction of distances to some of the clouds in the stream, and several bifurcations in the stream that had not been observed prior to this work.

Applying our codes to cosmological scenarios, we find we are able to explain the existence of High Velocity Clouds as a natural byproduct of Hierarchical Clustering within the Λ–dominated Cold Dark Matter (ΛCDM) paradigm. We are able to produce sufficient quantities of H I gas in such High Velocity Clouds, reflecting the known spatial and kinematical distributions of those observed, and go some of the way to reproducing other gas concentrations as well. We are able to make predictions as to their distances, placing them in the halo of the Milky Way, that are consistent also with the limited observational information thus far available.

Acknowledgements

I thank my supervisors Brad Gibson, Daisuke Kawata and Glen Mackie for giving me the opportunity to work on such interesting projects. I have been very fortunate in having Daisuke as a great supervisor and friend. He is always helpful and very enthusiastic, and his knowledge of Japanese cuisine will be remembered fondly for a lifetime.

I also benefited from the close collaboration with Jeremy Bailin, Stuart Gill and Chris Brook who all offered excellent intellectual and moral support. Along similar lines, thanks to Sarah Brough, Katie Kern, Alina Kiessling (and the rest of the students!), XKCD and PhDComics and in particular Chris "Chrispy" Power for ensuring I knew I wasn't alone (and PhDComics, as much a distraction as it was, for recently pointing out that you get through it in the end anyway). And thanks to James Murray for picking up the mental pieces when necessary. I thank my colleagues at the Anglo Australian Observatory for their constant prodding, and in particular, my managers Chris Ramage and Steve Lee for keeping me honest.

Thank you to Sarah Maddison and Jarrod Hurley who also stepped in and proof-read everything. And thanks go to Paul Bourke, Stuart Gill and Daisuke Kawata for their codes and permission to modify them, and Masafumi Noguchi for kindly providing his code for the orbit calculation, and Mary Putman for the carefully flagged MS portion of the HIPASS HVC cubes. Thanks to Jeremy Bailin, Chris Power, Chris Thom, Virginia Kilborn, Lister Staveley-Smith and Geraint Lewis for helpful discussions, and Christian Brüns for an advance copy of his paper before publication.

Extra thanks go to Agostino Renda, Craig West and Stefan Harfst (who is responsible for the eclectic choice of music I am listening to now) for the music outings and beer, and Andrew Jameson, Willem van Stratan, Steve Ord, Aidan Hotan, Haydon Knight, Alexander Knebe, Annie Hughes, Mike Beasley, Dominic Argast, Janne Holopainen, Chris Blake, Lee Spitler and Trevor Mendel for introducing me to their favourite corners of Melbourne and the concept of a life. And of course, Mum for all her support over the years.

I am grateful to the Department of Education, Science and Training for their financial assistance in the form of an Australian Postgraduate Award. The simulations were run on the Beowulf clusters at the Centre for Astrophysics & Supercomputing, Swinburne University, and the Australian and Victorian Partnership for Advanced Computing. Thanks also to the Astronomical Society of Australia for the recognition and opportunity to present my work.

Contents

List of Figures

List of Tables

Declaration

This thesis contains no material that has been accepted for the award of any other degree or diploma. To the best of my knowledge, this thesis contains no material previously published or written by another author, except where due reference is made in the text of the thesis.

Science is a collaborative pursuit, and the studies presented in this thesis are very much part of a team effort. All work presented is primarily that of the candidate. The collaborators listed below have great experience and knowledge, and were all integral in obtaining the presented results. They have contributed ideas for the content and/or editing of the papers that have been adapted to this thesis.

In Chapter 2, I summarise the physics of GCD+ relevant to our simulations. My original contribution to the work presented in has been in the adaption of the CLOUDY94 (Ferland et al., 1998) ionisation model, and the creation of the full suite of analysis software.

Chapter 3 represents work published in Connors, T. W., Kawata, D. & Gibson, B. K., "N-body simulations of the Magellanic stream", MNRAS, 371, 108, 2006. Additionally, I present in more detail the production of the initial conditions, the tests I performed including tests with star formation, and I present additional figures for completeness. The code to integrate the orbit using a Runge-Kutta algorithm was kindly supplied by Masafumi Noguchi, which I then modified to account for varying masses and differing boundary conditions and to integrate into the future.

Chapter 4 represents work published in Connors, T. W., Kawata, D., Bailin, J., Tumlinson, J. & Gibson, B. K., "On the Origin of Anomalous Velocity Clouds in the Milky Way", ApJL, 646, 53, 2006. My contribution was of the analysis of the simulations, with Daisuke Kawata and Jeremy Bailin (Bailin et al., 2005) having run the simulations partially on the feedback received back from my analysis. Jason Tumlinson provided the ionisation models. Additional sections have been added for work on the highly ionised clouds that did not fit within the scope of the ApJ letter.

Minor alterations beyond those mentioned above have been made to maintain consistency within the thesis.

left

Tim W. Connors

23 June 2008

Publications

Refereed Journals

[3] **T. W. Connors**, D. Kawata, J. Bailin, J. Tumlinson, B. K. Gibson:
On the Origin of Anomalous Velocity Clouds in the Milky Way
Astrophys. J. Letter **646**, 53 (2006)

[2] **T. W. Connors**, D. Kawata, B. K. Gibson:
N-body simulations of the Magellanic stream
Mon. Not. R. Astron. Soc. **371**, 108 (2006)

[1] **T. W. Connors**, D. Kawata, S. T. Maddison, B. K. Gibson:
High-Resolution N-body Simulations of Galactic Cannibalism: The Magellanic Stream
Publ. of the Astron. Soc. of Australia **21**, 222 (2004)

Proceedings

[1] B. K. Gibson, D. Kawata, C. Brook, **T. W. Connors**
The Chemodynamical Evolution of Galaxies
in Elemental Abundances in Old Stars and Damped Lyman-α Systems
(25th meeting of the IAU, Joint Discussion 15)
22 July 2003, Sydney, Australia

Oral Presentations

[2] *On the origin of anomalous velocity clouds in the Milky Way*
at the Astronomical Society of Australia Annual Science Meeting,
Sydney, Australia, July 2005

[1] *Simulations of galactic cannibalism: Magellanic stream*
at the Astronomical Society of Australia Annual Science Meeting,
Brisbane, Australia, July 2004

Nomenclature

$\odot$	Denotes a solar quantity
LSR	(Velocity in the) Local (average solar neighbourhood) Standard of Rest
GSR	(Velocity in the) Galactic Standard of Rest
MW	Milky Way Galaxy
LG	Local Group containing the MW
MS	Magellanic Stream
ICR	Magellanic inter-cloud region
LAF	Magellanic Leading Arm Feature
MCs	Magellanic Clouds
SMC	Small Magellanic Cloud
LMC	Large Magellanic Cloud
HVC	High Velocity Cloud
VHVC	Very High Velocity Cloud
CHVC	Compact High Velocity Cloud
DM	Dark Matter
ΛCDM	Lambda Cold Dark Matter; CDM with cosmological constant $\Lambda = 0.7$
ISM	Interstellar medium
ZEA	Zenith Equal Area projection used in mapping
AIT	Hammer-Aitoff Equal Area projection used in mapping
H I	Un-ionised hydrogen emission
H II or H α	Ionised hydrogen emission or absorption
C IV	Absorption from carbon with 3 electrons stripped
O VI	Absorption from oxygen with 5 electrons stripped
O VII	Absorption from oxygen with 6 electrons stripped
σ	Statistics: Standard deviation.
$M_\odot$	Unit: solar mass (mass; 1.99×10^{30} kg)
yr	Unit: (terrestrial) year
pc	Unit: parsec (distance; 3.09×10^{16} m)
$L_\star$	The galaxy of "typical" luminosity, including the MW
[X/Y]	$\log_{10}(N_X/N_Y) - \log_{10}(N_X/N_Y)_\odot$, or the number ratio of two elements relative to solar. ie.
[O/H]	$\log_{10}(O/H) - \log_{10}(O_\odot/H_\odot)$, the abundance of oxygen relative to hydrogen, compared to solar ratio
$Z_\odot$	solar metallicity; 0.02 by number fraction

Chapter 1

Introduction

"I used to be better at logic problems, before I just dumped them all into TeX and let Knuth pick out the survivors."

— Plorkwort, 26 September 2004, *alt.religion.kibology*

"Back off, man. I'm a scientist."

— Dr. Venkman, *GhostBusters*

Throughout this thesis we will use numerical simulations to gain a better understanding of hierarchical structure formation within the Universe. In particular we aim to shed light on unanswered questions concerning the recent dynamics of Local Group galaxies including our own.

1.1 Motivation

1.1.1 Hierarchical Clustering and Galactic Cannibalism

With the release of the Wilkinson Microwave Anisotropy Probe (WMAP) results (Spergel et al., 2003; Komatsu et al., 2008), the Cold Dark Matter (CDM) model has essentially shifted from a "favoured" paradigm (White & Rees, 1978; White et al., 1993) to what is now referred to as the "concordance model". Distinct from

the "rapid collapse" scenario, in which the underlying physical process was of a monolithic collapse of gas over the dynamical free-fall time (e.g. Eggen et al., 1962; Larson, 1974, 1976), hierarchical clustering is an important component of CDM models, in which the models suggest that at an early stage in the Universe, small amplitude density perturbations driven initially by quantum fluctuations were imprinted upon a nearly uniform background field (Davis et al., 1985). These Dark Matter (DM) perturbations represent the seeds of galaxy formation, growing initially in consort with the expanding Universe, but collapsing later at a time related to their density contrast relative to the background density. The first objects to collapse in the Universe were small, with the subsequent merging of many of these objects coupling with the collapse on increasingly larger scales as the Universe ages. Such collapsed halos provided the gravitational potential well within which gas accumulated, ultimately leading to the formation of stars and galaxies. The interaction and merging of these galaxies is accompanied by the violent disruption of smaller galaxies by their larger companions. Such merger- and accretion-driven evolution appears to have peaked over the redshift range $z \sim 2 - 5$ (e.g. Murali et al., 2002), but continues to the present-day. Indeed, our own Local Group (LG) provides several spectacular examples of ongoing hierarchical clustering, including the disrupting Sagittarius dwarf (Ibata et al., 1994), the putative Canis Major dwarf (Martin et al., 2005), and perhaps the most striking of all, the H I debris associated with the interacting Large and Small Magellanic Clouds (LMC and SMC) stretching 180° across the sky—the so-called Magellanic Stream (MS) (Mathewson et al., 1974). Disrupting satellites such as these are the best local laboratory to understand the physical processes of "galactic cannibalism", as we have the luxury of obtaining detailed observations pertaining to the respective systems' star formation histories (e.g. Harris & Zaritsky, 2004; Zaritsky & Harris, 2004; Smecker-Hane et al., 2002) and internal chemical evolution via stellar abundance patterns for individual stars within the satellites (Tolstoy et al., 2003). Smecker-Hane et al. (2002) in particular, attribute periodic peaks in the LMC's star formation history, to the tidal forces the LMC experiences as it is being cannibalised.

1.1.2 Numerical Simulations

Two complementary approaches to undertaking cosmological simulations include (i) N-body+hydrodynamics simulations, and (ii) the prescriptive generation of merger-

trees, based on semi-analytical techniques. The former often involves the interaction of individual "particles" of dark matter or stars and includes gravity (e.g. Barnes & Hut, 1986), and in some cases for the baryons, the equations of hydrodynamics using grid-based schemes (e.g. Cen & Ostriker, 1993; Yepes et al., 1997; Gnedin, 1998; Kravtsov, 2003; Tasker & Bryan, 2008) or particle-based hydrodynamical schemes (e.g. Navarro & Benz, 1991; Katz & Gunn, 1991; Katz, 1992; Steinmetz & Mueller, 1993; Weinberg et al., 2008). The latter semi-analytical techniques adopt a probabilistic, or Monte-Carlo approach, with the collapse times for the subclumps of a host halo being distributed in a large merger-tree, which is then evaluated repeatedly (e.g. Baugh et al., 1998; Cole et al., 2000; Helly et al., 2003). These semi-analytic techniques simulate the outcomes of any mergers and their physics in a heuristic manner, based on the formalism of Press & Schechter (1974). The two methods enable us to calculate different parameters. The semi-analytic approach enables the calculation of average properties of classes of galaxies, and can be used for testing large ranges of parameters, such as those used in star formation models (Baugh et al., 1998). However, they lack a self-consistent treatment of dynamics. The N-body approach enables us to look at individual galaxies, providing insight into dynamics that the semi-analytics cannot. This thesis is concerned with employing gravitational N-body and hydrodynamical techniques to simulate the physics of hierarchical clustering within our own Galaxy.

N-body Simulations

A typical galaxy is composed of approximately 10^{11} stars. To simulate this fully is a classical N-body problem. Since we cannot even solve 3 body problems analytically, we resort to numerical solutions. Simulations of galactic interactions do not require the modelling of each star individually, and often gas can be treated as particles. Holmberg (1941) performed the first numerical simulations of interacting galaxies, utilising the inverse square nature of light intensity emitted by light bulbs falling on photocell receptors. He manually moved the 2000 particles according to the measured light intensity on each receptor, and noticed the tidal distortion of the two disc galaxies as they interacted. Over the years, as computing power has increased, various assumptions in the computations dealing with interactions of galaxies have been relaxed.

An example of the evolution of N-body simulations is those used to understand

the MS. The first simulations of the Magellanic Clouds (MCs) tidally interacting with the Milky Way (MW), constructed each of the bodies with multiple test particles to probe the tidal fields without mutual gravitational interaction between the particles (Lin & Lynden-Bell, 1977; Davies & Wright, 1977; Murai & Fujimoto, 1980; Gardiner et al., 1994, hereafter LL77, DW77, MF80 and GSF94), to limit the calculations to complexity $\mathcal{O}(N)$[1]. Gardiner & Noguchi (1996, hereafter GN96) implemented self gravitation within the SMC, since it was expected to be the most tidally stripped of the three galaxies, but kept the MW and LMC as single test particles. This self gravity increased the algorithm complexity to $\mathcal{O}(N \log N)$. Gardiner (1999, hereafter, G99) added initial attempts at modelling the drag created by the stream travelling through the MW's halo, simultaneously with the tidal interactions. Li (1999) modelled the gas and the drag from ram pressure, and with all three bodies being fully self gravitating, using a total of $\sim 120,000$ particles in their highest resolution simulation (one third of them are gas, of which less than 15%, or ~ 6000, are assigned to the SMC). Maddison et al. (2002), also modelling the gas physics, found that there was little need to model the LMC and MW as live, as little material in the stream originated from those bodies. Such a conclusion may be tempered however, since the simulations were performed at very low mass resolution compared to the N-body, SMC only case, because of the computational expense particularly of the full hydrodynamical treatment. Yoshizawa & Noguchi (2003, hereafter, YN03) then modelled the gas with star formation in a more complete manner, which did not alter the conclusions of the prior works, but did show that the gas stream was largely devoid of stars as required by observations. A very recent innovation is to perform a grid of simulations with an evolutionary learning algorithm. Genetic algorithms have been adopted by Růžička et al. (2007) and Howley et al. (2008) to model both the MS and the interaction of NGC205 and M31. These are able to search parameter space much faster than traditional methods, as long as a quantitative "goodness of fit" can be formulated. Such a method has yet to be applied to more than simple low resolution models.

[1] $\mathcal{O}$ represents an order-of-magnitude calculation to the costs involved in evaluating an algorithm as a function of the input data size, ignoring factors that remain constant independent of the data size.

1.2 Studies in This Thesis

Each study in this thesis aims to compare the predictions of our chemodynamical simulations with preexisting observational datasets. These observations are of the H I in the MS and full sky coverage of various species of gas as observed from various satellites and ground based telescopes. The overall goal of this work is to shed light on unanswered questions concerning the hierarchical growth of galaxies in the LG, which involves the continual cannibalism of the smaller objects.

1.2.1 Magellanic Stream

One of the most obvious manifestations of cannibalism within the LG is that of the aforementioned MS. While the plane of the MW is perhaps the most spectacular *visible* sight in the southern sky, to eyes sensitive to the radio emission of H I gas, the night sky would look very different. The MW would still cut a swath across the sky, running overhead from horizon to horizon from our vantage point in Australia, but the equally impressive gas stream of the MS (also running overhead from horizon to horizon, but perpendicular to the MW) would also become prominent.

The MS is a remarkably colinear band of (primarily) neutral hydrogen (H I) stretching from horizon-to-horizon through the South Galactic Pole (SGP), emanating from the MCs. Dieter (1965) first found anomalously high-velocity gas features near the SGP, followed by Kuilenburg (1972), who discovered a lengthy high-velocity gas stream nearby. Wannier & Wrixon (1972) noted that the feature had a large and smoothly varying velocity (from $v_{\rm LSR} \sim 0$ to $-400\,{\rm km\,s^{-1}}$, or $v_{\rm GSR} \sim 0$ to $-200\,{\rm km\,s^{-1}}$), and was over 60° long but only $\sim 4°$ wide. Mathewson et al. (1974) finally confirmed the connection between this feature and the MCs, and named it the Magellanic Stream, suggesting the stream was 180° in length, lying on a great circle. They showed the stream was clumpy, and gave the designations MS I to MS VI to the six dominant clumps (Mathewson et al., 1977).

Putman et al. (1998, hereafter, P98) showed what is now considered to be nearly the full extent of the MS, extending to $(l, b) = (90°, -37°)$, and additionally, made the identification of a continuous Leading Arm Feature (LAF) extending to at least $(l, b) = (305°, 0°)$, which they definitively associated with the MCs. These results had lead to the MS and LAF being commonly regarded as being at least 165° in total length, and generally less than 10° in width. However, using newer datasets

extending more than 30° above the galactic equator, Wakker (2001), Wakker et al. (2002) and Brüns et al. (2005) reveal the possibility of several large High Velocity Cloud (HVC) complexes with $b \sim 30°$ being directly connected to the LAF. These complexes were given the names LA II and LA III, with the LAF component discovered by P98 (nearest the MCs and only extending to the galactic equator) being named LA I. Indirect evidence that these complexes are connected to the MCs was provided by the detection of their similar chemical fingerprints to those of the MCs (Lu et al., 1998). Furthermore, Ben Bekhti et al. (2006) found HVCs apparently associated with these LAF components, and used their structure to estimate distances to them of $10 - 60\,\mathrm{kpc}$, again demonstrating their likely connection to the MCs. McClure-Griffiths et al. (2008) further refined this by demonstrating that a HVC within the LAF was interacting with the Galactic disc at a Galactocentric distance of $\sim 17\,\mathrm{kpc}$. It is interesting to note that the gas associated with the MS appears to be seen in absorption against the background quasars Mrk 335 and Mrk 1501 more than 20° away from the MS proper (Gibson et al., 2000). Braun & Thilker (2004) go on to show that the MS may extend as far north as $b = -20°$. It would appear that in previous analyses of the system, the comparisons of simulations against the observational data has not taken into account the full extent of the MS. These spatial data provide strong constraints on any putative model.

From the head of the MS to the tail, there is a smooth transition of velocities from $v_{\mathrm{LSR}} = +250\,\mathrm{km\,s^{-1}}$ (near the SMC) to $-400\,\mathrm{km\,s^{-1}}$ (P98; Brüns et al., 2005). The Leading Arm's velocity range is from $v_{\mathrm{LSR}} = +250\,\mathrm{km\,s^{-1}}$ (near the source) to $+450\,\mathrm{km\,s^{-1}}$ (at the termination point). Both the MS and LAF appear internally turbulent, yet still collimated on large scales. These kinematic information also strongly differentiate the models.

Early models of the MS from MF80 and Lin & Lynden-Bell (1982), supplemented with the more recent proper motion work from Jones et al. (1994), have provided us with an accurate representation of the present-day orbital characteristics of the MCs. The Galactocentric[2] radial velocities of the MCs are very small at $89\,\mathrm{km\,s^{-1}}$ (van der Marel et al., 2002; Kallivayalil et al., 2006b) and $23\,\mathrm{km\,s^{-1}}$ (Hardy et al., 1989; GSF94; Kallivayalil et al., 2006a) for the LMC and SMC respectively, compared with their respective Galactocentric tangential velocities in the Galactocentric frame of $367\,\mathrm{km\,s^{-1}}$ (van der Marel et al., 2002; Kallivayalil et al., 2006b) and $300\,\mathrm{km\,s^{-1}}$

[2]Galactocentric velocities are measured relative to rest at the Galactic centre, and should not be confused with the Galactic Standard of Rest, which is measured relative to the Sun.

(Lin et al., 1995; Kallivayalil et al., 2006a), demonstrating that the Clouds are not receding rapidly. The determination of the orbital sense of the system demonstrates clearly that the MS is trailing and not leading the MCs, and is stretching beyond the present Galactocentric distance of the MCs (Lin & Lynden-Bell, 1982; Lin et al., 1995), and also that the MCs are close to peri-Galacticon. The closest approach to date, both between the MCs and between the MCs and the MW, occurred ~ 200 Myr ago, and the orbital period of the SMC about the LMC is ~ 900 Myr, with the MCs as a pair orbiting the Galaxy with a period of order 1.5 Gyr (e.g. GSF94). Despite our knowledge of the current positions and velocities of the Clouds, the orbital details are still not well constrained because of uncertainties over the shape of the MW, and the magnitude of the dynamical frictional force on and between the MCs. Uncertainties over the current tangential velocities of the SMC and LMC are dominated more by our lack of understanding on whether the MW is oblate, spherical or prolate (Helmi, 2004a,b; Johnston et al., 2005; Růžička et al., 2007), and the magnitude of the effects of dynamical friction on the orbits of the MCs (Binney & Tremaine, 1987; Hashimoto et al., 2003; Just & Peñarrubia, 2005). The only simulation to date that has included the dynamical frictional forces between the MCs is that of Bekki & Chiba (2005), and it is not yet clear if such a friction term is valid or necessary. Claims that the MCs are on their first orbit of the MW (Kallivayalil et al., 2006a; Besla et al., 2007; Piatek et al., 2008) have to be viewed in light of these uncertainties.

Considerable debate has existed in the literature as to the exact origin of the gas stream, the implications of which touches upon fundamental issues concerning the formation mechanism of the MW and galaxies in general. In essence, two theories were put forth: (i) the relatively gentle action of frictional drag forces (the "ram pressure model") was predominant in pulling the gas from one of the MCs, with the friction being provided by an extended corona of gas associated with our own Galactic halo (Mathewson et al., 1987; Moore & Davis, 1994; Heller & Rohlfs, 1994; Sofue, 1994; Mastropietro et al., 2005), and (ii) the more violent disruption of one of the Clouds due to the tidal force field (the "tidal model") provided by the LMC–SMC–MW interaction lead to a tidal stream (DW77; LL77; MF80; GSF94; Lin et al., 1995; GN96; Li, 1999; YN03; Bekki et al., 2004; Růžička et al., 2007). The latter theory is a fundamental consequence of gravitational hierarchical clustering. Such scenarios predict that tidal destruction and debris absorption continues to the present-day, albeit at a lower rate than seen in the early Universe. The observations

of the LAF (P98; Brüns et al., 2005) show that tidal forces account for at least some fraction of the "force" shaping the existence of the MS, even as the observed Hα emission measured along the MS suggest that some additional ram pressure heating effects may be present (Weiner & Williams, 1996, but compare Putman et al., 2003a).

Criticisms of the tidal model have traditionally come from two fronts. Since tidal disruption is expected to result in both a trailing *and* leading stream, objections originally resulted from the apparent lack of a leading counter-arm in the observations of Mathewson et al. (1974). The leading arm was finally unambiguously observed by P98. The second was that no stars were observed in the stream, despite them being equally affected by tidal forces. Yoshizawa (1998) and Li (1999) first showed that the stellar disc of the SMC may be smaller than the gas disc, and thus would not be stripped as easily.

Understanding the MS is pivotal for our understanding of tidal streams in general, due to its (i) proximity, (ii) spatial coherence, and (iii) the decoupled stellar and gaseous structure. Adding to the uniqueness of the system, unlike the stellar Sagittarius Stream (Ibata et al., 1994), the H I gas stream is not a clean (independent) probe of the shape of the MW gravitational potential because it is shaped by both tidal *and* hydrodynamical forces (including drag). The gas stream is an indirect probe into the DM and gas of the MW's halo, and the nature of the physics involved in streams which are susceptible to gravitational, hydrodynamical and drag forces makes the study of the MS particularly challenging and interesting. YN03 have recently provided a significant improvement to the now canonical tidal model of GN96, via the inclusion of gas dynamics and star formation. In a prescient forebearer to YN03, G99 also provided important extensions to the earlier GN96 work using new constraints introduced by the recent discovery of the LAF, the addition of a drag term into the particle force equations, and an improved modelling of the LMC's disc potential. These latter modifications have the beneficial effect of mildly deflecting the orientation of the LAF with respect to the MCs in a manner more consistent with the observations of P98 and Brüns et al. (2005).

Encouraged by the success of these earlier studies, we undertake in Chapter 3 a computational study aimed at deconstructing this Rosetta Stone of hierarchical clustering—the disrupting MCs. Our first step, neglecting the complicated gas physics and mutual interaction between the MW, LMC and SMC (only modelling the SMC as "live" particles), was required in order to allow a fuller exploration

of orbital parameter space prior to the introduction of gas into the modelling. The reason for doing so is that current observational constraints on the system still allow for some flexibility in choosing a unique orbital configuration for the system, partly due to our less-than-optimal understanding and conflicting observational data on the LMC and SMC masses and their orbits. The spatial orientation and nature of any SMC disc is also poorly constrained. Since N-body only simulations are less computationally "expensive" than hydrodynamical simulations, we can survey different orbits for the MCs, and determine our best orbital configuration(s). We demonstrate the parameter space that is disallowed by comparisons against the current observations of the MS. We show that a simple model of hydrodynamics and star formation goes some of the way towards validating our models. The *ultimate* aim, of which this thesis is a stepping stone towards, is the construction of a model which includes all relevant physical processes, including the live treatment of particles in all three bodies in the system, gas dynamics, ram pressure, radiative cooling, star formation, and chemical enrichment, all treated *self-consistently*, in a hope to understand the physical processes of galactic cannibalism.

1.2.2 High Velocity Clouds

Besides the accretion of satellites, there is other evidence that the MW is still growing. Chiappini et al. (2001) present two indirect arguments suggesting that the growth of MW is still ongoing. At the current rate of star formation, which is not characterised as a burst, there is only enough gas in the Interstellar Medium (ISM) to last 1 Gyr. Secondly, the metallicities obtained from long lived stars shows a narrowness of the distribution that is best explained if the ISM is continually replenished by a constant supply of gas from outside the Galaxy of similar low metallicity. The inflow rate they predict is $\sim 1\,\mathrm{M_\odot yr^{-1}}$.

HVCs, which are primarily H I gas clouds that do not participate in differential Galactic rotation, represent another aspect of hierarchical clustering that we see today. Typically defined as clouds that have $|v_{\mathrm{LSR}}| \gtrsim 100\,\mathrm{km\,s^{-1}}$, they are seen to cover much of the sky in H I. The inflow rate contributed by a single HVC complex—Complex C—has been estimated at $0.1\,\mathrm{M_\odot yr^{-1}}$ (Thom et al., 2007), a significant fraction of that needed to sustain the ISM. Several clouds have had their metallicities determined, with metallicities ranging from $\mathrm{Z} \sim 0.1 - 1\,\mathrm{Z_\odot}$ (Wakker et al., 2008). Complex C is one of those measured, and abundance variations across

it have been found, with $Z \sim 0.1 - 0.3\,Z_{\odot}$ (Wakker et al., 1999; Richter et al., 2001; Gibson et al., 2001; Tripp et al., 2003; Sembach et al., 2004; Collins et al., 2007).

Recently, theory and observations have made progress in explaining the existence of HVCs. Oort (1966) first proposed a number of mechanisms for HVCs, some of which have survived to the present day. The HVCs were proposed to be large "mini-halos" distributed through the filaments on Mpc-scales, travelling towards the LG (Blitz et al., 1999). This model has fallen out of favour since similar clouds are not seen around other galaxies such as M31, despite extensive searches (Thilker et al., 2004; Pisano et al., 2004; Westmeier et al., 2005a). A supernovae (SNe) driven Galactic fountain, reaching as high as 10 kpc above the disc (de Avillez, 2000), may be responsible for some solar metallicity HVCs. Such a fountain is caused by SNe in the disc expelling gas that enters the halo, cools and returns in a cyclic flow (Bregman, 1980; Houck & Bregman, 1990; Gibson et al., 2001; Oosterloo et al., 2007). HVCs may also be condensing out of a hot MW halo (Maller & Bullock, 2004), up to 150 kpc away. In this situation, the condensing clouds may themselves be growing through accretion as they approach the disc (Peek et al., 2008), and so large HVC complexes would be close, with $d \lesssim 15$ kpc. Such HVCs would be low metallicity, $Z \sim 0.01 - 0.2\,Z_{\odot}$. HVCs have been associated with the tidal accretion of H I rich dwarf galaxies in the case of the MS and LAF, and there are also tenuous connections of HVCs with the Sagittarius Stream (Putman et al., 2004). Such clouds would appear as long streams and be at the distances of these accreting bodies, with $30\,\mathrm{kpc} \lesssim d \lesssim 50\,\mathrm{kpc}$. They would likely have intermediate metallicities.

The three dimensional nature of HVCs, and in particular, their distances, remain the most important unknowns. Many quantities scale relative to the unknown distances (Wakker & van Woerden, 1997). Their diameters scale as d, their mass as d^2, density and pressure as d^{-1} (with temperature remaining independent of distance). The only direct method of obtaining distance limits to HVCs is via detecting the presence of absorption in stars with known distance constraints themselves. The presence of absorption indicates a star is behind a HVC, and the absence indicates a star that is in front of a HVC. Few HVCs are bracketed by stars both in front of and behind them, but such HVCs are found close ($d \sim 10$ kpc) to the MW by virtue of how they are selected (Wakker, 2001; Thom et al., 2006; Wakker et al., 2007, 2008). However, other HVCs must also be within 40 kpc since they mostly have associated H α emission (Putman et al., 2003a).

We do not have the full required information on their velocity. Despite individual

clouds contributing to an inflow, it is not obvious that there is a net inflow. The solar motion around the Galaxy contributes partially to the high $v_{\rm LSR}$ velocities seen, and so a non-symmetrical distribution about the sky will mimic a net in- or out-flow if we are not careful to exclude the gas with high $v_{\rm LSR}$ that is still consistent with differential Galactic rotation (Wakker & van Woerden, 1997). The unseen tangential components of any velocities make it impossible to determine in general whether an individual cloud is travelling towards or away from the Galaxy.

The various formation scenarios can be differentiated via the determination of distances and metallicities to the HVC populations. Knowing the metallicity and distances, we would be able to estimate the rate of accretion of low metallicity gas as Thom et al. (2007) have done for Complex C. We would know the rate of circulation of the Galactic fountain (Wakker et al., 2008), and we could calibrate the fraction of ionising photons escaping from the MW disc, since we see H α in many HVCs (Bland-Hawthorn & Maloney, 1999).

Putman & Moore (2002) performed a purely N-body simulation of a LG analogue and found a population of HVCs which they compared to the MW. While they found some similarities between the simulation and the MW's HVC population, the conclusion was tempered by the realisation that the observed HVCs were likely decoupled from the DM they were simulating.

In Chapter 4, we engage in a study to find whether Λ–dominated Cold Dark Matter (ΛCDM) cosmological hydrodynamical simulations are able to generate galaxies with HVC distributions similar to the those of the MW. We furthermore set out to find whether generic MW-size disc galaxies are all likely to contain HVCs to some degree, resulting from hierarchical clustering. In doing so, we perform two high-resolution cosmological hydrodynamical simulations of systems similar to the MW. Immersing ourselves within the simulation to project the gas from the vantage point of a virtual observer at a position analogous to the Sun, we compare the HVCs positional, kinematic and chemical information against that of our own Galaxy and other galaxies for which HVC data exist. We track the origin and evolution of clouds as they form HVC like structures in the halo of the galaxies.

Chapter 2

Numerical Simulations

Summary

In this chapter, we give a summary of the underlying structure of the GCD+ software developed in Kawata (1999, 2001a,b) and Kawata & Gibson (2003a,b). We go on to describe how we can use the chemical information derived from the simulations to compare with absorption and emission line observations of various ionisation species, and the transformations necessary to convert the particle based simulation data into synthetic data cubes to compare with observations, in order to study the evolution of our systems.

2.1 Introduction

In simulating the immediate environment of the Milky Way (MW), Large and Small Magellanic Clouds (LMC and SMC), and the High Velocity Clouds (HVCs), this thesis utilises the galactic chemodynamical evolution software package GCD+. GCD+ is a parallel vectorised code that models self-gravity, hydrodynamics, star formation, radiative cooling, supernovae (SNe) feedback and metal enrichment. It was originally and primarily developed by Kawata (1999), and further detailed descriptions of GCD+ can be found in Kawata (2001a,b) and Kawata & Gibson (2003a,b). Improvements to this code have been ongoing as new software methodologies for simulating galaxy formation have been developed (e.g. Brook et al., 2004).

Projecting the simulations from the perspective of a virtual observer within the MW, we are able to compare the simulations directly against observations in a form observers are familiar with. This thesis develops a software package that can project an arbitrary particle simulation into the observer's plane.

In this chapter, we report on the two major components of software used in this thesis. Section 2.2 presents an overview of the relevant physics modelled in GCD+, Section 2.3 demonstrates the methods used to analyse both the simulations and pre-existing observational data sets in an identical fashion, and Section 2.4 shows how we analyse the simulations in an interactive fashion. In our study of the Magellanic Stream (MS), which we detail in Chapter 3, we use a simpler, cheaper mode of operation of GCD+, ignoring most of the gas physics. In our study of HVCs, detailed in Chapter 4, the full capabilities of GCD+ are used. The description of the generation of initial conditions for each of these will be left to their respective chapters.

2.2 GCD+

Galaxies are essentially comprised of Dark Matter (DM), stars, and gas, each of which can be modelled in GCD+. The code represents bodies by a large number, N, of point-like particles. Each particle is "tagged" with its own unique kinematic and physical properties that evolve with the particle over time.

Gravity is modelled using the tree method (Tree; Barnes & Hut, 1986), and the hydrodynamics is modelled using the Smooth Particle Hydrodynamical (SPH) algorithm (TreeSPH; Gingold & Monaghan, 1977; Lucy, 1977). Both the hierarchical tree method and the SPH algorithm are fully Lagrangian, gridless, and adaptive in both time and space. The operation of the SPH algorithm is very similar to that of Tree codes. In each timestep, the characteristic size of an SPH particle will be determined by searching for an approximately fixed number of neighbouring particles. Once the characteristic length is determined, hydrodynamical calculations are performed only over those neighbouring particles. The effective resolution of the simulation is given by this characteristic length, decreasing with overall number of particles in a simulation, and smaller features cannot be resolved. This effective length leads naturally to a combination of SPH and Tree N-body methods, where the dynamics of DM and stars are calculated using a Tree N-body scheme and gas dynamics are simulated using SPH. Our code, GCD+, is based on earlier numerical models for galaxy formation that combine the N-body techniques with the SPH method (e.g. Hernquist & Katz, 1989; Navarro & White, 1993; Katz et al., 1996; Steinmetz, 1996; Carraro et al., 1998). It is a code that can be switched easily

between TreeSPH to include hydrodynamics, and a pure Tree N-body implementation to just model gravity. When the hydrodynamical forces in a system are much smaller than the gravitational forces, such as in a tidal stream, it is valid to model the system with purely gravitational particles, but we cannot calculate properties of the gas such as metallicity and temperature, nor model star formation. We can thus turn off the hydrodynamics when we wish to perform faster gravitational-only surveys of parameter space. We use this cheaper mode of operation of GCD+ for the majority of our MS study involving the LMC-SMC-MW system, reserving the more expensive SPH mode for fine tuning of the model and performing detailed cosmological simulations of a Local Group sized environment around the host MW.

2.2.1 Modelling Dark Matter and Stellar Dynamics: the N-body Method

Both DM and star particles (or gas particles in the non-hydrodynamical, N-body-only case) are collisionless in GCD+ and are modelled using a tree N-body technique. In a collisionless N-body simulation, the gravitational potential is calculated by summing the forces for each particle. The gravitational force of the i-th particle is calculated by the sum of the contributions from DM, star and gas particles as follows

$$\nabla_i \Phi = -G \sum_j \frac{m_j \mathbf{x}_{ij}}{(r_{ij}^2 + \epsilon_{ij}^2)^{3/2}}, \tag{2.1}$$

where $r_{\rm ij} = |\mathbf{x}_{ij}|$, $\mathbf{x}_{ij} = \mathbf{x}_i - \mathbf{x}_j$ and $\epsilon_{ij} = (\epsilon_i + \epsilon_j)/2$ is the mean softening length of the i-th and j-th particles. A softening parameter, ϵ, is introduced for several reasons (Aarseth, 1963; Dehnen, 2001). Collisionless simulations of galaxies are performed with a number of particles, N, that is far less than the number of stars in the systems we are concerned with, and as such, collisions between the particles do not represent physical collisions. These particles are a Monte Carlo representation of the underlying continuous Distribution Function (DF), and this information is hence incomplete. Instead of representing each particle by δ functions, leading to the divergence of the gravitational force when the separation between particles becomes small, we assume a smooth distribution of mass, and soften the forces at small particle separations. Such a softening has the effect of minimising artificial two body encounters, but more importantly, we only require an estimated force field computed with approximate, and hence cheaper, methods than direct summation.

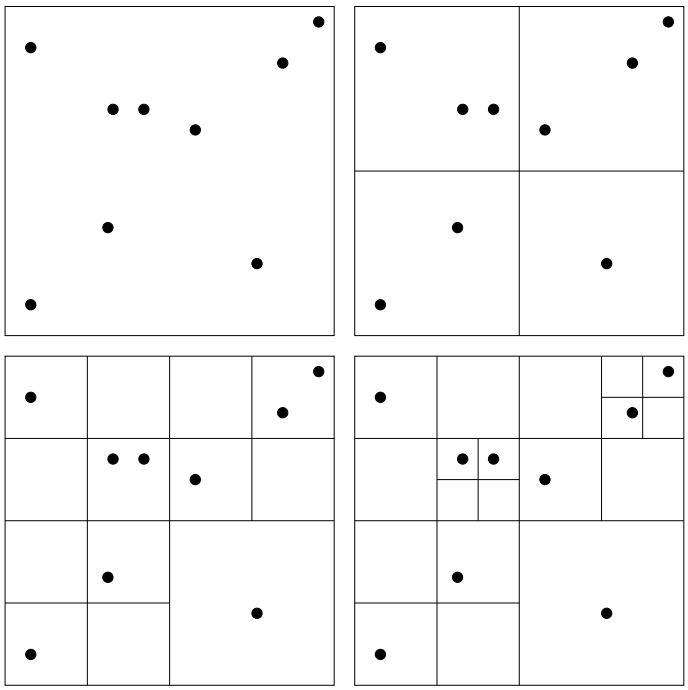

Figure 2.1: Step-by-step division of space for a simple 2-D particle distribution from top-left to bottom-right. Each cell is repeatedly divided into 4 more cells, until only one particle remains in a cell.

Without softening, the large forces due to a close encounter lead to a large change in the velocities of the particles involved, which require extremely small timesteps in the numerical integration of the equations of motion. The softening parameter mitigates the large accelerations accompanying such close encounters, which are a numerical rather than physical in nature.

Computationally, the gravitational force calculation used is based upon the hierarchical tree formalism (e.g. Barnes & Hut, 1986; Pfalzner & Gibbon, 1997). This scheme starts with a single cubic "cell" which encloses all the particles of the system. In three dimensions, this cell is divided in half in each dimension to yield eight daughter cells. Then the tree algorithm asks the question: how many particles are there in the cell — 0, 1, or > 1? If the cell is empty, it is ignored. If there is one particle in the cell (either gas, DM or star), this is stored and then left alone. If there are more particles in a cell, this cell is subdivided in the next level. This subdivision process continues until there are no cells with more than one particle left.

Figure 2.1 shows this step by step division for a two dimensional particle distribution for ease of illustration. The purpose of the algorithm is to reduce the time

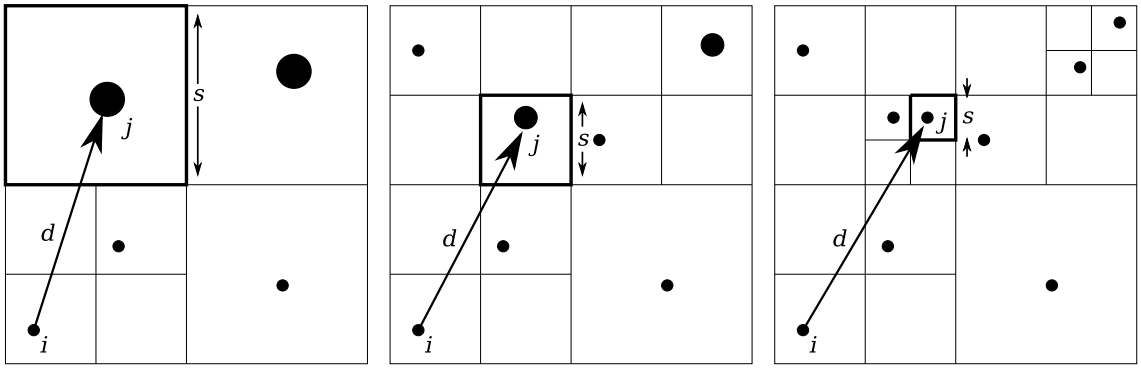

Figure 2.2: The relation s/d for different levels of the tree. The number of particles added together is dependent on the distance from the i-th particle. The total mass and centre of mass of the particles in the cells are shown in these different levels, and the size of the symbol is proportional to the mass of the pseudo-particle.

taken to compute the gravitational potential for all the particles from $\mathcal{O}(N^2)$ to $\mathcal{O}(N \log N)$ by including contributions from near particles by a direct sum, whereas the influence of remote particles is taken into account only by including larger cells.

Figure 2.2 shows how the particles can be successively added together to produce pseudo-particles with the general properties of the individual particles the associated cell contains. The number of particles added together is dependent on the distance from the i-th particle. The choice of when to group particles together is made first by establishing the "size", s, of the cell containing the j-th particle. This is then compared with the distance d from particle i. If the criterion

$$s/d \leq \theta \tag{2.2}$$

is fulfilled, where θ is a fixed tolerance parameter, then the force calculated from Equation (2.1) is added to the particle. If not, then cells at the next level are taken, as illustrated in each successive plot in Figure 2.2, and the calculation is done again until the criterion of Equation (2.2) is satisfied. The tolerance parameter in GCD+ is $\theta = 0.8$ with expansions to the quadrupole order (Pfalzner & Gibbon, 1997).

This generalisation is justified because with all cosmological–scale N-body simulations there is a certain amount of error introduced due to round-off, truncation, and discreteness effects in both space and time, which makes it unnecessary to compute the potential field to extremely high precision. The tree structure means that distinguishing between close particles and distant particles without actually

calculating the distance between every particle is simplified.

2.2.2 Modelling Gas Dynamics: the SPH Method

The gas dynamics in GCD+ are calculated using SPH (Gingold & Monaghan, 1977; Lucy, 1977). In SPH, the gas is treated as a continuous fluid that is approximated by a collection of interpolation points, each moving with the local fluid velocity. In GCD+ each gas particle acts as a small volume of fluid. The forces on a particle exerted by neighbouring particles approximate the work done upon the original volume of fluid by pressure forces. Frictional forces between particles correspond to the fluid viscosity. Each particle carries as well as its position and velocity, properties such as mass, density and internal energy, so forces such as self-gravity become relatively simple to calculate.

It is assumed that the mass density of the fluid is roughly proportional to the particle mass density. In order to reduce the local statistical fluctuations in particle number, a smoothing kernel is introduced. GCD+ employs the spherically symmetric cubic spline kernel of Steinmetz (1996):

$$W(r,h) = \frac{8}{\pi h^3} \begin{cases} 1 - 6(r/h)^2 + 6(r/h)^3 & \text{if } 0 \leq r/h \leq 1/2, \\ 2[1-(r/h)]^3 & \text{if } 1/2 \leq r/h \leq 1, \\ 0 & \text{otherwise,} \end{cases} \tag{2.3}$$

where r is the distance from the particle and h is an individual particle's smoothing length. The smoothing length of each particle is dynamic in GCD+, and the algorithm employed within GCD+ is based upon that of Thacker et al. (2000), which ensures that the number of particles within this variable smoothing length remains roughly constant (Figure 2.3). Hence, all points in the fluid have smoothed quantities computed to the same level of mass resolution.

Initially, the neighbours of the i-th particle are counted using the smoothing kernel,

$$W_{\rm nn}(r,h_i) = \begin{cases} 1 & \text{if } 0 \leq r/h_i \leq 3/4, \\ \frac{\pi h_i^3}{8} W(4(r/h_i - 3/4)) & \text{if } 3/4 \leq r/h_i \leq 1, \end{cases} \tag{2.4}$$

where r is the distance between the i-th particle and its neighbour, and $W(\mathbf{x})$ is the spline kernel given by Equation (2.3). The evolution of the smoothing length is determined by the smoothing length h^n and the number of neighbours $N^n_{{\rm nb},i}$ contained

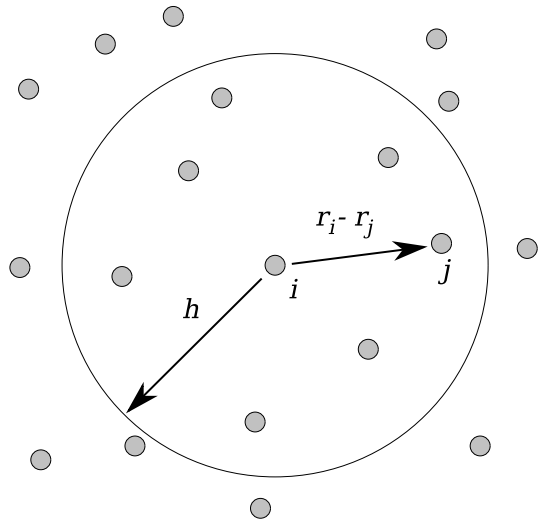

Figure 2.3: The definition of smoothing length h and neighbour particles. In SPH, the smoothing length is dynamic so that the number of neighbour particles contained within the smoothing length remains roughly constant.

within the previous, n, timestep

$$h_i^{n+1} = h_i^n \left[1 - a + a \left(\frac{N_\mathrm{s}}{N_{\mathrm{nb},i}^n} \right)^{1/3} \right], \tag{2.5}$$

where N_s is the specified number of neighbours (Hernquist & Katz 1989). The adopted value $N_\mathrm{s} = 40$ provides acceptable accuracy as demonstrated by their one–dimensional shock tube tests. $N_{\mathrm{nb},i}$ is the actual number of neighbours and a is a variable that changes as a function of the parameter $s = (N_\mathrm{s}/N_{\mathrm{nb},i}^n)^{1/3}$, as

$$a = \begin{cases} 0.2(1+s^2) & \text{if } s < 1, \\ 0.2(1+1/s^3) & \text{if } s \geq 1. \end{cases} \tag{2.6}$$

All the physical parameters are calculated for each gas particle using the smoothing kernel given by Equation (2.3). The density, ρ, is calculated by

$$\rho_i = \sum_j m_j W(r_{ij}, h_{ij}), \tag{2.7}$$

where $h_{ij} = (h_i + h_j)/2$ is the averaged smoothing length between a pair of particles.

The kinematics of the i-th particle are traced using Euler's equation in the form

of

$$\frac{d\mathbf{v}_i}{dt} = -\frac{1}{\rho_i}\nabla_i(P + P_{\rm visc}) - \nabla_i\Phi_i, \tag{2.8}$$

where Φ is the gravitational potential, P is the pressure and $P_{\rm visc}$ is the artificial viscous pressure. The gravitational force, $\nabla_i\Phi_i$, is calculated as in Equation (2.1).

The smoothed estimate of the pressure gradient term (e.g. Steinmetz, 1996) can be written as

$$\frac{1}{\rho_i}\nabla_i(P + P_{\rm visc}) = \sum_j \left(\frac{P_i}{\rho_i^2} + \frac{P_j}{\rho_j^2} + Q_{ij}\right)\nabla_i W(\mathbf{x}_{ij}, h_{ij}), \tag{2.9}$$

where Q_{ij} is the artificial viscosity. The artificial viscous pressure term allows for the presence of shock waves in the flows to be included computationally (Gingold & Monaghan, 1983). Shock fronts generate energy and transform kinetic energy into internal energy, preferably with minimum post-shock oscillations to the hydrodynamical variables. The form taken for the artificial viscosity follows (Navarro & Steinmetz, 1997)

$$Q_{ij} = \begin{cases} \dfrac{-\alpha v_{{\rm s},ij}\mu_{ij} + \beta\mu_{ij}^2}{\rho_{ij}} & \text{if } \mathbf{x}_{ij}\cdot\mathbf{v}_{ij} < 0, \\ 0 & \text{otherwise,} \end{cases} \tag{2.10}$$

with

$$\mu_{ij} = \frac{0.5 h_{ij}\mathbf{v}_{ij}\cdot\mathbf{x}_{ij}}{r_{ij}^2 + \eta^2}, \tag{2.11}$$

where $\mathbf{v}_{ij} = \mathbf{v}_i - \mathbf{v}_j$. The parameters $\alpha = 1.0$ and $\beta = 2$ control the amplitude of the post-shock oscillation. They are set to reproduce features of the one–dimensional shock tube experiment. The parameter $\eta = 0.05 h_{ij}$ is introduced to prevent numerical divergences.

In order to reduce the shear component of the artificial viscosity, a correction is included for a "shear-free" viscosity, following the form given in Balsara (1995)

$$\tilde{Q}_{ij} = Q_{ij}\frac{f_i + f_j}{2}, \tag{2.12}$$

$$f_i = \frac{|\langle\nabla\cdot\mathbf{v}\rangle_i|}{|\langle\nabla\cdot\mathbf{v}\rangle_i| + |\langle\nabla\times\mathbf{v}\rangle_i| + 0.0002 v_{{\rm s},i}/h_i} \tag{2.13}$$

where $v_{\rm s}$ is the sound velocity. The velocity divergence and rotation are calculated

by

$$\langle \nabla \cdot \mathbf{v} \rangle_i = -\frac{1}{\rho_i} \sum_j m_j \mathbf{v}_{ij} \cdot \nabla_i W(\mathbf{x}_{ij}, h_{ij}), \tag{2.14}$$

$$\langle \nabla \times \mathbf{v} \rangle_{i,x} = -\frac{1}{\rho_i} \sum_j m_j [v_{ij,z} \nabla_{i,y} W(\mathbf{x}_{ij}, h_{ij}) - v_{ij,y} \nabla_{i,z} W(\mathbf{x}_{ij}, h_{ij})], \tag{2.15}$$

where $v_{ij,x} = v_{i,x} - v_{j,x}$. If the flow is shear-free and compressive, the corrected viscosity term is identical to the uncorrected term.

In order to calculate the velocity and position of each particle, Equation (2.8) is integrated using a leap-frog algorithm with individual timesteps (e.g. Hernquist & Katz, 1989; Makino, 1991). The timestep of the i-th particle is chosen to be

$$\Delta t_i = \min(0.3\Delta t_{\mathrm{CFL},i}, 0.1\Delta t_{\mathrm{f},i}), \tag{2.16}$$

where Δt_{CFL} is determined by the Courant-Friedrichs-Lewy condition as

$$\Delta t_{\mathrm{CFL},i} = \frac{0.5 h_i}{v_{\mathrm{s},i} + 0.6(\alpha v_{\mathrm{s},i} + \beta \max_j |\mu_{ij}|)}, \tag{2.17}$$

and Δt_{f} is determined by the requirement that the force should not change significantly from one timestep to the next, which would result in poor energy conservation. This is achieved by

$$\Delta t_{\mathrm{f},i} = \sqrt{\frac{h_i}{2} \left| \frac{d\mathbf{v}_i}{dt} \right|^{-1}}. \tag{2.18}$$

In a dense region, the smoothing length may become shorter than the softening length of Equation (2.1). In order to avoid this, a lower limit for the smoothing length is set to be $h_{min} = \epsilon/2$. For collisionless DM and star particles, the timestep is determined by

$$\Delta t = \min[0.16(\epsilon/v), 0.4(\epsilon/|dv/dt|^{1/2})]. \tag{2.19}$$

This implies that decreasing the characteristic masses in the system by increasing the mass resolution, requires us to increase the time resolution, and hence acts as the limiting factor in the simulations we can perform. This limits us in the current thesis to simulating 400,000 N-body-only particles with mass resolution of 7.5×10^3 $\mathrm{M}_\odot$ and 100,000 timesteps of approximately 25,000 years each (using 1 CPU-year of compute time across 16 CPUs), or alternatively using the full hydrodynamical capabilities of GCD+, ∼400,000 total particles (composed of ∼200,000 DM, ∼100,000 gas and

$\sim$100,000 star particles) in SPH simulations, with mass resolution of $\sim 10^6\,\mathrm{M}_\odot$.

The leap-frog method then involves integrating the position and velocity as follows

$$\mathbf{v}^{n+1/2} = \mathbf{v}^n + 0.5\left(\frac{d\mathbf{v}}{dt}(\mathbf{x}^n, \tilde{\mathbf{v}}^n, \ldots)\right)^n \Delta t^{n\rightarrow n+1}, \tag{2.20}$$

$$\mathbf{x}^{n+1} = \mathbf{x}^n + \mathbf{v}^{n+1/2}\Delta t^{n\rightarrow n+1}, \tag{2.21}$$

$$\tilde{\mathbf{v}}^{n+1} = \mathbf{v}^{n+1/2} + 0.5\left(\frac{d\mathbf{v}}{dt}(\mathbf{x}^n, \tilde{\mathbf{v}}^n, \ldots)\right)^n \Delta t^{n\rightarrow n+1}, \tag{2.22}$$

$$\mathbf{v}^{n+1} = \mathbf{v}^{n+1/2} + 0.5\left(\frac{d\mathbf{v}}{dt}(\mathbf{x}^{n+1}, \tilde{\mathbf{v}}^{n+1}, \ldots)\right)^{n+1} \Delta t^{n\rightarrow n+1}, \tag{2.23}$$

where $\Delta t^{n\rightarrow n+1}$ represents a time interval between steps n and $n+1$.

The smoothed form of the thermal energy equation used in GCD+ to determine the evolution of the internal energy, u_i, is

$$\frac{du_i}{dt} = \frac{P_i}{\rho_i}\sum_j m_j \mathbf{v}_{ij}\cdot\nabla_i W(\mathbf{x}_{ij}, h_{ij}) + \frac{1}{2}\sum_j m_j Q_{ij}\mathbf{v}_{ij}\cdot\nabla_i W(\mathbf{x}_{ij}, h_{ij}) - \frac{\Lambda_i}{\rho_i} + H_i. \tag{2.24}$$

The first term in Equation (2.24) corresponds to the adiabatic expansion of the gas, the second term to the heating and cooling from the artificial viscosity, the third term to radiative cooling, and the fourth term to the heating via SNe feedback.

When the evolution of the internal energy of each particle is integrated, the minimum of the above calculated timesteps is used and the energy equation is integrated semi-implicitly using the trapezoidal rule (Hernquist & Katz, 1989)

$$u^{n+1} = u^n + 0.5\left[\left(\frac{du}{dt}\right)^n + \left(\frac{du}{dt}\right)^{n+1}\right]\Delta t^{n\rightarrow n+1}. \tag{2.25}$$

Since $(du/dt)^{n+1}$ depends on u^{n+1}, this equation must be solved iteratively. First, a prediction for the thermal energy $\tilde{u}^{n+1}$ is obtained by assuming that $(du/dt)^{n+1} = (du/dt)^n$. The predicted value, $\tilde{u}^{n+1}$ is combined with the predicted velocity $\tilde{\mathbf{v}}^{n+1}$ from Equation (2.22), to estimate the adiabatic term, including the artificial viscosity and the heating in Equation (2.24). Only the cooling term, Λ^{n+1}, is estimated iteratively using the corrected internal energy, once the adiabatic term is obtained. A convergent solution is found using the bisection technique. Additionally, in order to ensure numerical stability, the radiative cooling is damped (e.g. Katz & Gunn,

1991

$$\left(\frac{du}{dt}\right)_{\rm rad}^{\rm damped} = \frac{a(du/dt)_{\rm rad}}{\sqrt{a^2 + [(du/dt)_{\rm rad}]^2}}, \tag{2.26}$$

$$a = 0.5\frac{u}{\delta t} + \left(\frac{du}{dt}\right)_{\rm ad}. \tag{2.27}$$

where $(du/dt)_{\rm ad}$ is the change in thermal energy, excluding the contribution from the undamped radiative cooling, $(du/dt)_{\rm rad} = \Lambda/\rho_{\rm g}$ in Equation (2.24).

The final equation describing the evolution of the fluid determines the pressure, P, of each particle using the equation of state for an ideal gas

$$P = (\gamma - 1)\rho u, \tag{2.28}$$

where u is the specific internal energy and $\gamma = 5/3$ for mono–atomic gas such as atomic hydrogen.

2.2.3 Radiative Gas Cooling

To model gas cooling in GCD+, the cooling function of the gas assumed to be in ionisation equilibrium was calculated for various metallicities using MAPPINGS III (the successor of MAPPINGS II described in Sutherland & Dopita, 1993). Because of the strong role metals play in the cooling of gas radiatively (e.g. Källander & Hultman, 1998; Kay et al., 2000), it is important to use metallicity-dependent models when calculating the cooling rate. Figure 2.4 shows the cooling curves employed in GCD+. The cooling rates of the gas as a function of temperature at metallicities [Fe/H] < -3 and [Fe/H] > 0.5 are assumed to be the same as the rates at [Fe/H] $= -3$ and [Fe/H] $= 0.5$ respectively. Linear interpolation between the cooling curves at the given temperature is used at intermediate metallicities.

The temperature for each gas particle in GCD+ is derived by

$$T_i = P_i \mu m_{\rm p}/(k_{\rm B}\rho_i) \tag{2.29}$$

where P_i is the pressure and ρ_i is the density of the i-th particle, μ is the mean molecular weight, $k_{\rm B}$ is Boltzmann's constant and $m_{\rm p}$ is the proton mass. For simplicity, the mean molecular weight is fixed at $\mu = 0.6$, independent of metallicity. The lower limit to the calculated temperature is $T_{\rm lim} = 100\,{\rm K}$.

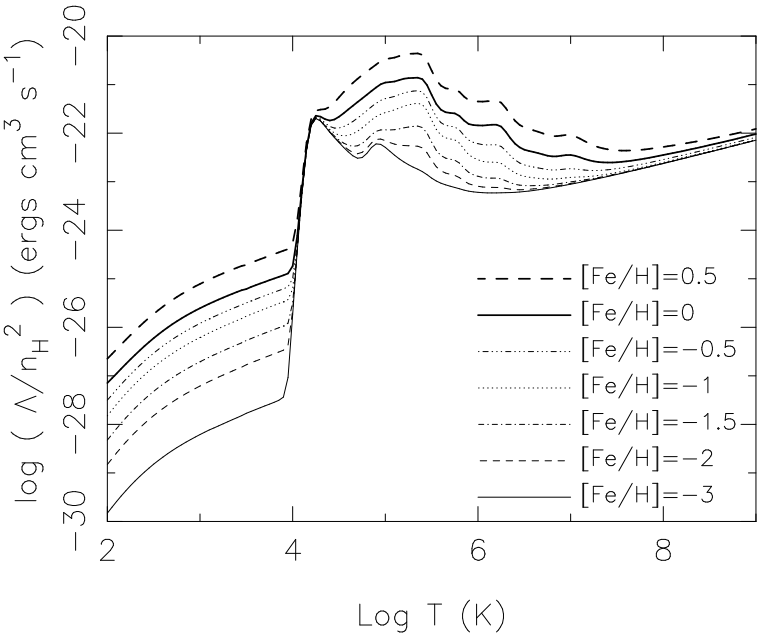

Figure 2.4: Cooling rates, plotted as a function of temperature, for the metallicities indicated (Kawata & Gibson, 2003a). Linear interpolation of these curves is used to calculate cooling rates as a function of temperature and metallicity.

2.2.4 Star Formation

Star formation is modelled in GCD+ using a method similar to those suggested by Katz (1992) and Katz et al. (1996). A gas particle can be converted into a star particle if the three main criteria for star formation are met:

1. The gas density is greater than a critical density:
   $\rho_{\rm crit} = 2 \times 10^{-25}\,{\rm g\,cm^{-3}}$ (Katz et al., 1996).

2. The gas velocity field is convergent: $\nabla \cdot v_i < 0$.

3. The gas is Jeans unstable, i.e. $h/v_{\rm s} > \tau_{\rm g}$, where h is the smoothing length, $v_{\rm s}$ is the speed of sound and $\tau_{\rm g} = \sqrt{3\pi/16G\rho_{\rm g}}$ is the dynamical time of the gas.

When a gas particle satisfies these conditions and is eligible to form stars, its star formation rate (SFR) is given by

$$\frac{d\rho_*}{dt} = -\frac{d\rho_{\rm g}}{dt} = \frac{c_*\rho_{\rm g}}{\tau_{\rm g}} \tag{2.30}$$

where $\tau_{\rm g}$ is the dynamical time, which is longer then the cooling time-scale in the region eligible to form stars. Equation (2.30) corresponds to the Schmidt law that

states that the SFR is proportional to $\rho_{\rm g}^{1.5}$. The star formation efficiency is parameterised by the dimensionless parameter c_*.

A probabilistic approach is used to avoid creating an intolerably large number of new star particles with different masses by ensuring that the one gas particle transforms into one star particle. The newly created star particle behaves dynamically as a collisionless particle as described in Section 2.2.1. Equation (2.30) implies that the probability p_*, that one gas particle entirely transforms into a star particle during a discrete timestep, Δt, is

$$\mathrm{p}_* = 1 - \exp(-c_* \Delta t / \tau_{\rm g}). \tag{2.31}$$

2.2.5 Initial Mass Function

Stars are represented as particles in GCD+ with a typical mass around $10^5 - 10^6\,\mathrm{M}_\odot$. Each star particle therefore represents many stars of varying masses, with the relative number distribution of stellar masses within a star particle at its birth being governed by the assumed initial mass function (IMF) as described by Salpeter (1955). The Salpeter IMF is written (by number) as

$$dn = \Phi(m)dm = Am^{-(1+x)}\,dm, \tag{2.32}$$

where $x = 1.35$ is the Salpeter index corresponding to an IMF by mass proportional to m^{-x}. The coefficient A is determined by normalising the IMF to unity over the specified range of stellar masses. The upper and lower mass limits are set to $M_{\rm u} = 60\,\mathrm{M}_\odot$ and $M_{\rm l} = 0.1\,\mathrm{M}_\odot$ respectively.

2.2.6 Feedback

GCD+ takes account of energy feedback and metal enrichment from SNe, as well as metal enrichment from intermediate-mass stars. Both Type II (SNe II) and Type Ia (SNe Ia) supernovae are considered. GCD+ uses the IMF and assumed stellar lifetimes to calculate the event rates and metal yields of SNe II and SNe Ia, and the metal yields of intermediate mass stars for each star particle at each timestep. The stellar lifetimes are those described by Kodama (1997) and Kodama & Arimoto (1997).

Supernovae

In GCD+, the mass, energy and heavy elements released by SNe are smoothed over the neighbouring gas particles using the SPH kernel (Katz, 1992). For example, in the timestep where the i-th star particle has a SNe event and a mass, $M_{\mathrm{ej},i}$, is ejected, the increment of mass that the j-th particle receives is

$$\Delta M_{\mathrm{ej},j} = \frac{m_j}{\rho_{\mathrm{g},i}} M_{\mathrm{ej},i} W(r_{ij}, h_{ij}), \tag{2.33}$$

where

$$\rho_{\mathrm{g},i} = \langle \rho_{\mathrm{g}}(x_i) \rangle = \sum_{j \neq i} m_j W(r_{ij}, h_{ij}), \tag{2.34}$$

and $W(r_{ij}, h_{ij})$ is the SPH kernel given by Equation (2.3). The code assumes that each massive star ($\geq 8\,\mathrm{M}_\odot$) explodes as a SNe II. The rates for SNe Ia follow the model proposed by Kobayashi et al. (2000, hereafter, KTN00). This model assumes that SNe Ia occur in binary systems which consist of primary and companion stars with appropriate masses. The model also assumes that SNe Ia do not occur in low metallicity stars with [Fe/H] < -1.1 (although this is implemented in GCD+ as the total metallicity ratio, rather than the iron abundance: [Z/H] < -1.1).

In this formalism, primary stars have a main-sequence mass with the lower and upper limits given by $m_{\mathrm{p,l}} = 3\,\mathrm{M}_\odot$ and $m_{\mathrm{p,u}} = 8\,\mathrm{M}_\odot$ respectively. These stars evolve into C + O white dwarfs (WDs). The mass range of companion (donor) stars is restricted to $m_{\mathrm{d,RG,l}} = 0.9\,\mathrm{M}_\odot$ and $m_{\mathrm{d,RG,u}} = 1.5\,\mathrm{M}_\odot$ for low mass red giants (RGs). KTN00 designate this binary system as a "RG + WD" system. Slightly evolved main sequence companions with masses ranging between $m_{\mathrm{d,MS,l}} = 1.8\,\mathrm{M}_\odot$ and $m_{\mathrm{d,MS,u}} = 2.6\,\mathrm{M}_\odot$ are designated as a "MS + WD" system by KTN00.

The total number of SNe Ia is a function of the age, t, of a star particle with a mass of m_{s}, and is given by

$$\begin{aligned} N_{\mathrm{SNeIa}}(t) &= m_{\mathrm{s}} \left(\int_{m_{\mathrm{p,l}}}^{m_{\mathrm{p,u}}} m^{-(1+x)} dm \right) \left(\int_{M_{\mathrm{l}}}^{M_{\mathrm{u}}} m^{-x} dm \right)^{-1} \\ &\quad \times \left[b_{\mathrm{MS}} \frac{\int_{\max(m_{\mathrm{d,MS,l}}, m_t)}^{m_{\mathrm{d,MS,u}}} \Phi_{\mathrm{d}}(m) dm}{\int_{m_{\mathrm{d,MS,l}}}^{m_{\mathrm{d,MS,u}}} \Phi_{\mathrm{d}}(m) dm} + b_{\mathrm{RG}} \frac{\int_{\max(m_{\mathrm{d,RG,l}}, m_t)}^{m_{\mathrm{d,RG,u}}} \Phi_{\mathrm{d}}(m) dm}{\int_{m_{\mathrm{d,RG,l}}}^{m_{\mathrm{d,RG,u}}} \Phi_{\mathrm{d}}(m) dm} \right], \end{aligned} \tag{2.35}$$

where m_t is the mass of the star whose lifetime is equal to t, and $x = 1.35$ is the Salpeter index of the IMF. The first term in Equation (2.35) indicates the number of C + O WDs, i.e. primary stars. The second term determines how many of the

C + O WDs evolve into SNe Ia from the MS + WD systems. The final term determines how many of the C + O WDs evolve into SNe Ia from RG + WD systems. Following KTN00, the main sequence and red giant binary fractions used in GCD+ are $b_{\rm MS} = 0.05$ and $b_{\rm RG} = 0.02$ respectively.

Heavy Elements

GCD+ follows the evolution of the abundances of several chemical elements: ^{1}H, ^{4}He, ^{12}C, ^{14}N, ^{16}O, ^{20}Ne, ^{24}Mg, ^{28}Si, ^{56}Fe and Z, where Z is the total metallicity. The solar abundances of Woosley & Weaver (1995, hereafter, WW95) are used. WW95 also provides SNe II yields for stellar masses between 11 and 40 $\rm M_{\odot}$, and metallicities between 0 and 1 $\rm Z_{\odot}$. Three different models are considered for $m \geq 30\,\rm M_{\odot}$ in WW95, each differing in the amount of energy imparted by the piston in their models at explosion initiation. Following Timmes et al. (1995), GCD+ uses the "B" models from WW95, which offer a compromise between being too energetic, or having all of the heavy elements fall back onto the star. For masses above $m \geq 40\,\rm M_{\odot}$, the same abundance ratios are assumed for the yields and the same mass fraction for the remnants as those for a 40 $\rm M_{\odot}$ star. For $\rm Z \geq Z_{\odot}$, a simple scaling formula is used, e.g. for the yield of carbon from a star with mass, m, and metallicity, Z, is given by

$$m_{\rm ej,C}({\rm Z}, m) = m_{\rm ej,C}({\rm Z}_{\odot}, m) + m_{\rm ej}({\rm Z}_{\odot}, m){\rm Z}_{\rm C,\odot}\left(\frac{\rm Z}{{\rm Z}_{\odot}} - 1\right), \qquad (2.36)$$

where $m_{\rm ej,C}$ is the total mass of ejected carbon, including newly synthesised and initial carbon, $m_{\rm ej} = m_{\rm ej,H} + m_{\rm ej,He} + m_{\rm ej,Z}$ indicates the total ejected mass and $\rm Z_{C,\odot}$ is the solar abundance of carbon. The yields of WW95 are metallicity dependent and GCD+ makes linear interpolations between different metallicities to calculate the yields.

The nucleosynthesis prescription for SNe Ia is taken from Iwamoto et al. (1999), using the faster deflagration model, W7, widely used in galactic chemical evolution calculations. The yields and remnant masses for intermediate-mass stars ($\leq 8\,\rm M_{\odot}$) are taken from van den Hoek & Groenewegen (1997, hereafter vdHG97). vdHG97 present yields of ^{1}H, ^{4}He, ^{12}C, ^{13}C, ^{14}N and ^{16}O for stars with initial masses between 0.8 and 8 $\rm M_{\odot}$ and initial metallicities between Z = 0.001–0.04. GCD+ does not use the ^{13}C yields. Initial abundances for ^{20}Ne, ^{24}Mg, ^{28}Si and ^{56}Fe are scaled to the solar abundance set. For stars with Z > 0.04, the same scaling as Equation (2.36) based on Z = 0.04 yields is used. Yields for stars with mass 8–11 $\rm M_{\odot}$ remain uncertain, so

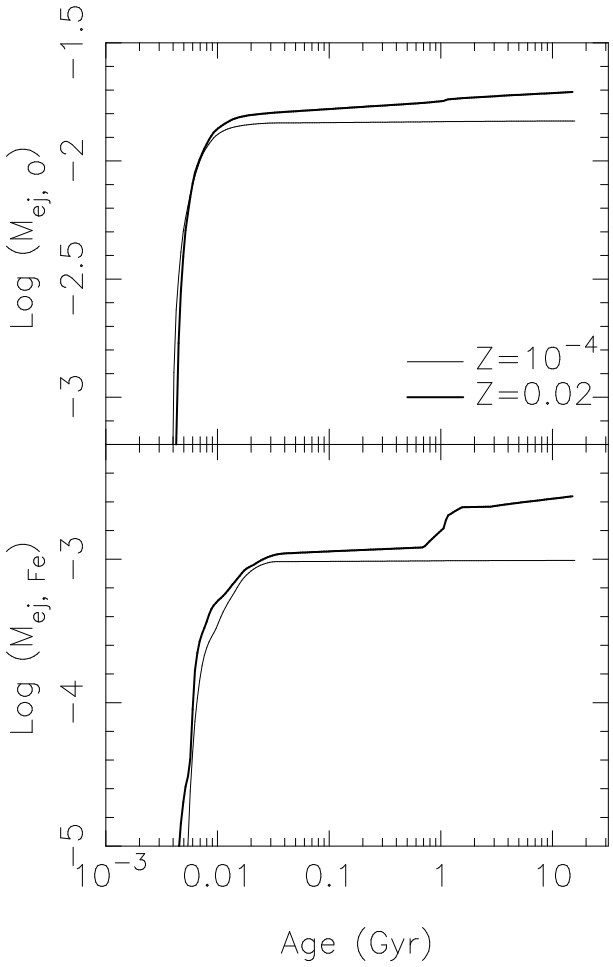

Figure 2.5: Chemical yields resulting from a burst of star formation as a function of time (Kawata & Gibson, 2003a). The upper (lower) panel shows the mass fraction of the initial star forming burst ejected as oxygen (iron). The history of a star particle is shown for two metallicities, Z = 0.02 (Solar; thick line) and Z = 10^{-4} (thin line).

linear interpolation is used between yields of the most massive stars in the tables of vdHG97 and the lowest mass stars in the tables of WW95.

A further uncertainty exists in the yields from zero metallicity stars. GCD+ assumes the yields from the lowest metallicity stars in the vdHG97 tables. Although this simple assumption may overestimate the ejected metals, this should not dramatically affect the final metallicity (Limongi & Chieffi, 2003).

The total amount of oxygen and iron ejected from a burst of star formation as a function of time is shown in Figure 2.5. Metals are initially ejected by SNe II, which produce most of the oxygen. This continues until 8 $M_\odot$ stars die (after ~ 0.04 Gyr in the case of Z = $Z_\odot = 0.02$). After SNe II production ceases, any additional oxygen

ejection is due to intermediate-mass stars. The timescale for iron production is set by the lifetime of the secondary in the binary systems which lead to SNe Ia.

GCD+ possesses look-up tables of the yields of all the chemical elements, remnant masses and number of SNe as a function of the age and metallicity. The values relevant to each star are calculated at each timestep.

Energy Feedback

One of the most difficult and most critical processes to model in galaxy formation simulations is the way in which the energy feedback from SNe affects the surrounding gas. GCD+ adopts a simple model which assumes that the energy produced by SNe affects only the temperature and velocity field of the surrounding gas, and its effect is implemented by increasing the thermal ($E_{\rm th}$) and kinetic ($E_{\rm kin}$) energy of the gas neighbours of each star particle that has an SNe event, by an amount corresponding to the energy released by SNe (Kawata & Gibson, 2003a). A parameter $f_v = E_{\rm kin}/(E_{\rm kin} + E_{\rm th})$ defines the fraction of the energy available to perturb the gas velocity field, and the rest of the energy of the SNe contributes to the increase in the thermal energy of the gas (Kawata, 2001a). It is known that kinetic feedback affects the history of star formation more strongly than thermal feedback, which quickly dissipates due to efficient radiative cooling where the gas density is high enough to form stars. We assume that each SN yields an energy of $\epsilon_{\rm SN} \times 10^{51}\,{\rm erg}$, and that

$$E_{\rm kin} = f_v \epsilon_{\rm SN} 10^{51}\,{\rm erg}, \tag{2.37}$$

where the parameters $\epsilon_{\rm SN}$ and f_v control the magnitude of the size and effect of SNe (Kawata, 2001a; Navarro & White, 1993). Since an initial SN energy has not been established quantitatively, the available SN energy, $\epsilon_{\rm SN}$, as well as f_v, are treated as free parameters.

2.2.7 Collisional Ionisation Equilibrium

GCD+ follows the elemental abundances but not the ionisation fractions of each element. Observations, however, are made only of the fractional absorption of various ionisation species, such as O VI, O VII and C IV obtained from Far Ultraviolet Spectroscopic Explorer (FUSE) data (Fox et al., 2004, 2005, 2006), and the emission of H I from the H I Parkes All-Sky Survey (HIPASS) survey (Putman et al., 1998).

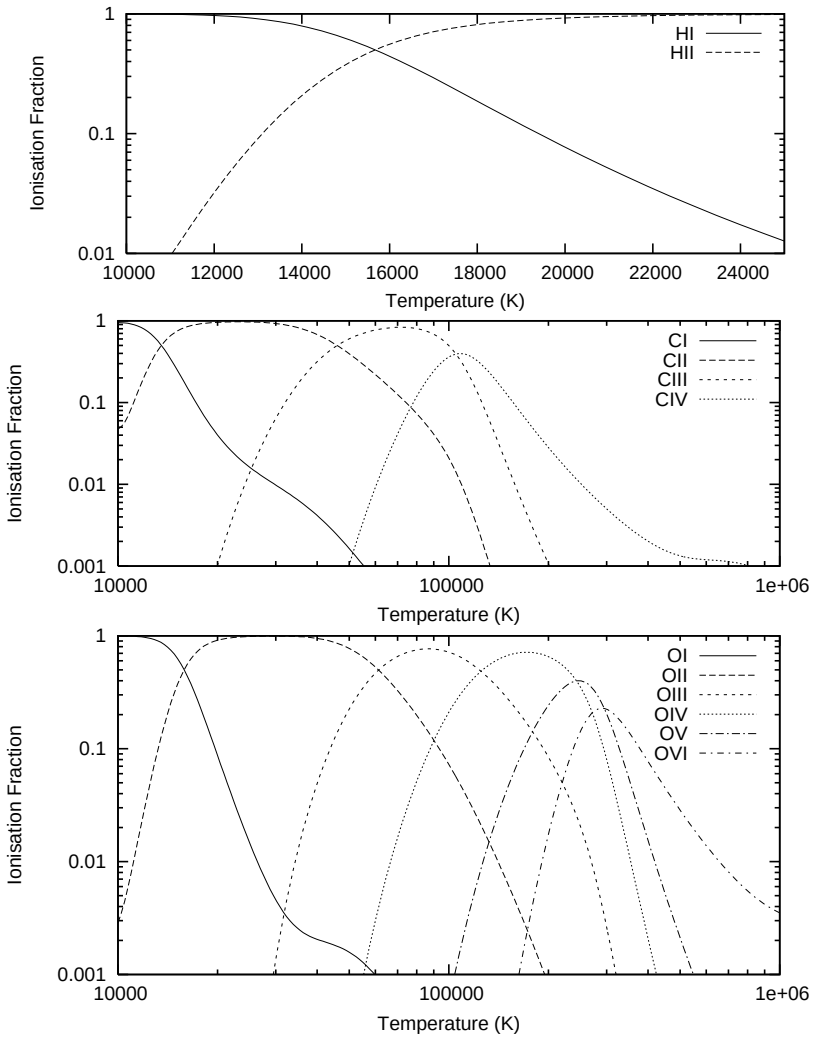

Figure 2.6: Ionisation fractions of hydrogen, carbon and oxygen up to H II, C IV and O VI respectively, calculated using the collisional ionisation models of CLOUDY94.

However, we can determine ionisation fractions indirectly from the simulations. Using CLOUDY94 (Ferland et al., 1998), we assume collisional ionisation equilibrium (CIE) and since ionisation fractions within CIE depend only on the temperature of the gas, we are able to calculate abundances of individual ionisation species after a GCD+ simulation using the temperature of each gas particle and the abundance ratios of the elements of interest. Figure 2.6 shows the ionisation fractions of each species of hydrogen, carbon and oxygen, as a function of gas temperature.

2.3 Analysis Techniques: Moment Maps

2.3.1 Conversion Between Observational and Simulation Domains

The output of GCD+ is a list of particles and their physical quantities in a Cartesian coordinate system. In our MS simulations (Chapter 3), this coordinate system is centred on the SMC, and in our HVCs simulations (Chapter 4), the coordinate system is centred on the MW. We need to convert this into a form that can be compared to observed H I data cubes. Previous work on the MS (Murai & Fujimoto, 1980; Moore & Davis, 1994; GSF94; GN96; G99; Maddison et al., 2002; YN03; Mastropietro et al., 2005) mainly concentrated on the qualitative distribution of simulation particles and only looked at the total mass contained within the simulated Leading Arm Feature (LAF) and MS. We opt to instead smooth the particle distribution into a form that can be "observed" and perform a more quantitative analysis, comparing features as consistently as possible.

In both the HVCs and MS simulations, we project each particle in the snapshot corresponding to the current time onto the Galactic coordinate system, along with any fiduciary markers, such as the grid markers and the orbits of the Magellanic Clouds (MCs) and Galaxy. We then obtain the moment we are interested in, and smooth the discrete particle distribution using a variable length smoothing kernel.

Because of difficulties in producing all-sky maps using conventional data visualisation routines (Marquarding, 2004), and in order to facilitate comparisons with our simulations, we convert the voxels (pixels with a depth corresponding to velocity) in FITS data-cubes obtained from observations of the MS into a list of "particles" and pass them through exactly the same analysis path as our simulations. For all plots we generate, this process also removes the effect of the differences in mass resolution between the simulations versus observations.

The steps in our pipeline are illustrated in Figure 2.7. Each of these steps is described in the following sections.

2.3.2 Observational Data

MS H I observational data is obtained from the HIPASS survey, both in the form of a carefully flagged cube mosaic comprising the main portion of the MS and leading

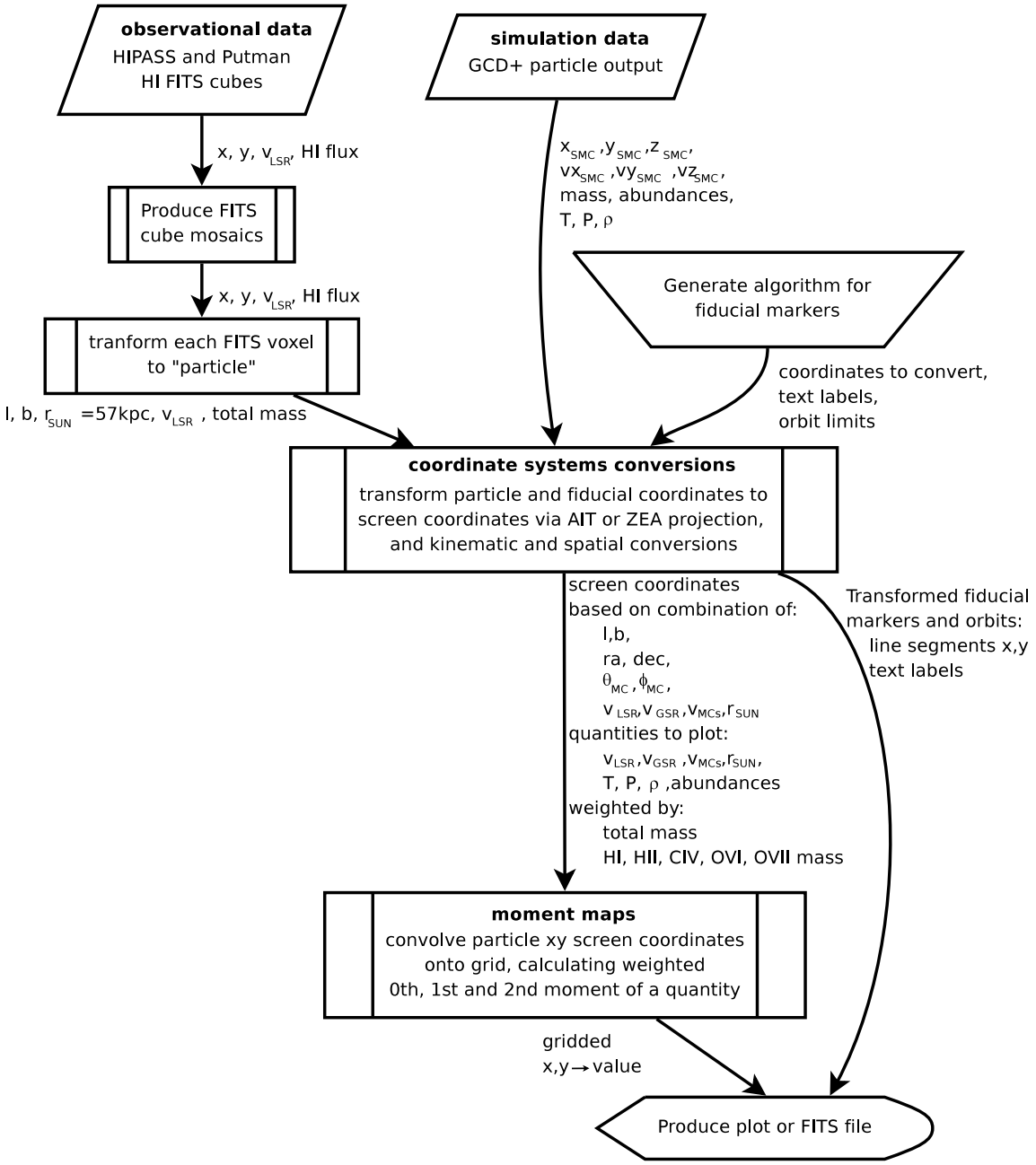

Figure 2.7: Pipeline showing how both the observational cubes and GCD particle outputs are processed through an identical pipeline, allowing precise comparisons between the two datasets input into the top of the diagram. Quantities propagated from one process to the next are shown. The meaning of the symbols is discussed in the following text.

portion of LAF (Putman et al., 2003b), and from additional cubes surrounding the LAF (Barnes et al., 2001). In order to aid comparisons between the observational data and simulations, from each voxel containing flux within the HIPASS position–position–velocity cubes, we wish to obtain a "particle" that we can pass through our analysis pipeline in an identical fashion to our simulation particles. We thus wish to synthesise a sensible distance to each voxel and obtain a mass corresponding to the flux within a voxel at this synthesised distance.

At the edge of each HIPASS cube is an increased noise level due to the nature of the observations. However, each cube overlaps with the other nearest cubes, and so to minimise noise, we construct a mosaic of each of the cubes using conventional data reduction techniques prior to converting to particles. A mosaic of these data extends across the South Galactic Pole (SGP) and reaches North of the equator, presenting difficulties for standard analysis and data visualisation in either MIRIAD or AIPS++ (Marquarding, 2004), since the corners of the created images do not correspond to valid world coordinates in the projection used in the observational data (Calabretta & Greisen, 2002).

In creating the mosaic, we first regrid the existing mosaic from the Zenith Equal Area (ZEA) projection to the Sansom-Flamsteed (SFL, identical to the "GLS" projection of Calabretta & Greisen, 2002, in this case) projection using AIPS++, since MIRIAD does not have the capability to deal with ZEA cubes. All other HIPASS cubes are individually inspected visually to find velocity ranges that are likely to correspond to the LAF, with careful exclusion of all likely Galactic gas emission. We then import the cubes into MIRIAD and smooth between the velocity channels to remove noise alternating in sign between each velocity channel, and apply a filter to only include the velocity ranges determined above, using the MIRIAD tasks HANNING and IMMASK. Using the regridded original mosaic as a template, we then regrid all cubes individually to the GLS projection using the MIRIAD task REGRID. Finally, all cubes including the original mosaic can be mosaiced using the IMCOMB task in MIRIAD. This final cube mosaic cannot be displayed with fiducial marks within any of the KARMA visualisation suite, AIPS++ or DS9, since the cube corners are again not valid world coordinates. Additionally, a bug in the REGRID task results in large amounts of flux being found outside the valid regions of the sky defined by the GLS projection. Despite these problems, we can however analyse the resultant raw FITS cube.

The GLS projection is best defined by its inverse for our purposes, following

Calabretta & Greisen (2002),

$$l = \frac{x}{\cos y} \tag{2.38}$$

$$b = y. \tag{2.39}$$

Due to the aforementioned bug in REGRID, many voxels in the mosaiced cube are found to have flux outside of the valid area defined by Equation (2.38), which requires that $|x| \leq 180\cos(y)$. It is found that these locations can be mapped back to valid coordinates via the subtraction from l of an integral number of 360° turns. We find in performing a test mosaic that adding the flux back into valid regions of the image results in the original flux being obtained.

Assuming optically thin H I (an assumption expected to break down at high column densities $N_{\rm HI} \gtrsim 10^{21}\,{\rm cm}^{-2}$; Dickey & Lockman, 1990), we convert the H I flux for each voxel into a H I mass following Wakker & van Woerden (1991),

$$M_{\rm HI} = 0.235 D_{\rm kpc}^2 S_{\rm tot}, \tag{2.40}$$

where the H I mass $M_{\rm HI}$ is in $\mathrm{M}_\odot$, the total H I flux $S_{\rm tot}$ is in Jy km s^{-1}, and the distance from observer to each synthesised particle is taken to be $D_{\rm kpc} = 57$ kpc, with the same distance being assumed when converting back to fluxes at the culmination of the visualisation pipeline. The fluxes in the FITS cube are stored with units Jy/beam. We obtain from this the total flux per voxel $S_{\rm tot} = \frac{A_{\rm p}}{A_{\rm b}}\Delta v$. The pixel size of the mosaic is $p_{\rm x} = p_{\rm y} = 8$ arcmin, giving a pixel area of $A_{\rm p} = p_{\rm x}p_{\rm y} = 64\,{\rm arcmin}^2$. The beam size is obtained by adding in quadrature the average beam size in the HIPASS survey of 14.3 arcmin with a 6 arcmin smoothing kernel to give $b_{\rm maj} = b_{\rm min} = 15.5$ arcmin, giving a beam area of $A_{\rm b} = 1.13 \times b_{\rm maj} \times b_{\rm min} = 271\,{\rm arcmin}^2$ (Barnes et al., 2001), although it is strictly variable according to source brightness and size. The width of the velocity channels in the cube is $\Delta v = 13.2\,{\rm km\,s}^{-1}$. To both minimise noise in the moment maps and limit the amount of data we have to manipulate, we place a lower limit on the amount of flux in any individual voxel of $200\,\mathrm{M}_\odot$ per voxel, or equivalently, 85 mJy/beam or $\sim 6\sigma$. Finally, we assume a H I mass fraction of 0.76, and convert the H I mass of each synthesised particles into a total gas mass. Analysis on all synthesised particles is then performed identically to the simulation particles.

2.3.3 Coordinate Systems Conversion

Coordinate Systems Used in the Magellanic Stream Simulations

For the display of our MS simulations, we choose a projection that creates minimal shape distortion at the area of interest while preserving flux. When looking at the main portion of the MS, the full sky ZEA is such a projection. In the ZEA projection, the x and y image coordinates are obtained from the galactic coordinates (l, b) following Calabretta & Greisen (2002),

$$x = -R_\theta \sin(l) \tag{2.41}$$

$$y = -R_\theta \cos(l), \tag{2.42}$$

where $R_\theta = \frac{360}{\pi} \sin\left(\frac{90-b}{2}\right)$.

To minimise distortion, we re-project the area of interest to the centre of the image. The observed MS is roughly centred on the SGP and stretches along the 90° and 270° meridians. We hence rotate the coordinate system, before applying Equations (2.41) and (2.42), such that the SGP rather than the North Galactic Pole is the projection centre, and the MS stretches horizontally across the image. This is done simply by inverting the galactic sphere, negating both the galactic longitude and latitude of each particle, such that the new coordinates become $(l', b') = (-l, -b)$. When focusing on just the LAF, the point defined by $(l_p, b_p) = (295°, 0°)$ is chosen to define the pole of a new coordinate system, and hence the new projection centre. By choosing a point 90° away and perpendicular to the approximate plane of the stream, at $(l_0, b_0) = (25°, 0°)$, we can define the origin of the new coordinate system. Prior to applying the projection defined by Equations (2.41) and (2.42), we re-project the coordinates (l, b) to new coordinates (l', b') following Calabretta & Greisen (2002),

$$\sin(b') = \sin(b_p)\sin(b) + \cos(b_p)\cos(b)\cos(l_p - l) \tag{2.43}$$

$$\tan(l') = \frac{\sin(a)\cos(b) - \cos(a)\sin(b)}{\cos(a)\cos(b) + \sin(a)\sin(b)}, \tag{2.44}$$

where

$$\sin(a) = \frac{\sin(l_p - l)\cos(b)}{\cos(b')} \tag{2.45}$$

$$\cos(a) = \frac{\sin(b) - \sin(b')\sin(b_p)}{\cos(b')\cos(b_p)} \tag{2.46}$$

$$\sin(b) = \sin(l_p - l_0)\cos(b_0) \quad (2.47)$$

$$\cos(b) = \sin(b_0)/\cos(b_p). \quad (2.48)$$

In a similar way, analogous to Wannier & Wrixon (1972), we define a Magellanic coordinate system such that the MS lies approximately along the equator (Wakker, 2001). The Magellanic longitude can then be used to quantify the variation of quantities such as velocity along the MS. Since the MS lies approximately along the great circle defined by $l = 90°$ and $l = 270°$, this is chosen to form the equator of the Magellanic coordinate system. Formally, this is done by defining the pole of the new system (l_p, b_p) as $(l, b) = (180°, 0°)$, the origin as the location on the new equator with same galactic longitude as the LMC, $(l, b) = (270°, b_{\rm LMC})$, and performing the conversion from galactic coordinates to the Magellanic coordinate system via Equations (2.43) and (2.44).

Coordinate Systems Used in the HVC Simulations

For the display of our HVC simulations, we choose to match the HVCs literature by using a full sky Hammer-Aitoff (AIT) projection, which is an equal area projection more suitable for full sky coverage of the Galactic system than the ZEA projection used traditionally for the MS. This projection is defined following Calabretta & Greisen (2002),

$$x = -2\gamma\cos(b)\sin(l/2) \quad (2.49)$$

$$y = \gamma\sin(b), \quad (2.50)$$

where $\gamma = \frac{180}{\pi}\sqrt{\frac{2}{1+\cos(b)\cos(l/2)}}$. We also use the AIT projection when focussing on the whole of the MS and LAF.

Conversion Between Velocity Frames

Observations of gas in both the MS and HVCs sample only one dimension of velocity information, that is, along the line of sight. We thus reduce the 3 dimensional velocity information of the particles in the simulations to a line of sight velocity in the Local Standard of Rest (LSR), relative to the solar system. Thus $v_{\rm LSR} = \Delta\mathbf{v} \cdot \frac{\Delta\mathbf{d}}{|\Delta\mathbf{d}|}$, where $\Delta\mathbf{d} = \mathbf{d} - \mathbf{d}_\odot$ and $\Delta\mathbf{v} = \mathbf{v} - \mathbf{v}_\odot$ are the distance and velocity vectors between the Sun and the particle we are interested in, and the current solar position and

velocity is taken to be $\mathbf{d}_\odot = (-8.5, 0, 0)\,\mathrm{kpc}$ and $\mathbf{v}_\odot = (0, 220, 0)\,\mathrm{km\,s^{-1}}$ (Kerr & Lynden-Bell, 1986).

The motion of the Sun introduces a spurious velocity gradient across the sky unrelated to the motion of the MCs or any bulk motion of the HVCs. By removing the line of sight motion of the Sun from the line of sight velocity vector, we can trivially remove the effects of this motion. Thus converting from the LSR to the Galactic Standard of Rest (GSR) is performed by

$$v_{\mathrm{GSR}} = v_{\mathrm{LSR}} + 220 \sin l \cos b \tag{2.51}$$

which removes the motion of the Sun, but does not attempt to compensate for the displacement of the Sun from the Galactic centre.

Even in the GSR, the MS exhibits a very large range in velocities. In order to be able to compare subtle velocity differences between models and between observations, we remove the bulk velocity gradient from the MS. By fitting the velocity v_{GSR} of the observations as a function of Magellanic longitude θ_{MC}, we can obtain a simple trend using just the first two harmonics, and subtract it from v_{GSR} of the observations and simulations, using

$$\begin{aligned} v_{\mathrm{sub}} &= v_{\mathrm{GSR}} - v_{\mathrm{MS,avg}} && (2.52)\\ &= v_{\mathrm{GSR}} - A_1 \sin(\theta_{\mathrm{MC}} + B_1) - A_2 \sin(2(\theta_{\mathrm{MC}} + B_2)), && (2.53) \end{aligned}$$

where the fits obtained are $A_1 = 86$, $A_2 = -92$, $B_1 = 2.5°$ and $B_2 = -26°$.

2.3.4 Moment Maps

From both the simulations and MS observations, we wish to obtain a two or three dimensional map with either position–position, position–velocity or position–position–velocity information, from a list of particles. The observations contain two dimensions of high mass resolution, high spatial resolution information and one dimension of low resolution velocity, whereas the simulations are of lower mass resolution, and contain the six dimensions of phase space.

In the MS observations, each particle represents a voxel, and they have been sampled on a regular grid, although regridded via the projections performed in the above sections. Voxels corresponding in mass to $200\,\mathrm{M}_\odot$ (or equivalently, 85 mJy/beam) can be discerned from the noise at the $\sim 6\sigma$ level. The voxel size is 8 arcmin in

angle and $13.2\,\mathrm{km\,s^{-1}}$ in velocity. This leads to 7×10^5 voxels with flux above the 6σ noise cutoff, 4×10^5 of which are in the MS and LAF, which together measure $\sim 180^\circ \times 20^\circ$ in total size.

The simulations have not been sampled on any such grid, but are instead composed of sparse discrete particle data that sample an underlying, smooth DF. The mass resolution is at best $7,500\,\mathrm{M_\odot}$ in our highest resolution MS simulations, and 55,000 of the 200,000 H I particles are found in the MS and LAF, which occupy $\sim 180^\circ \times 40^\circ$ on the sky in the simulations. Thus we can expect ~ 7 particles per square degree, compared to the ~ 100 particles per square degree in the observed stream when the velocity dispersion is $\sim 20\,\mathrm{km\,s^{-1}}$.

Despite the differing resolutions of the observed and simulated datasets, we can equally successfully bin the discretised particles from each onto a regular pixilated grid (or cube in the three dimensional case), smoothing the discrete data by a variable width Gaussian as we construct the image. To reduce the observed spatial resolution to manageable levels, and ensure that we are not attempting to oversample the original observed data, we limit the pixel size to no less than 0.3° in angular size and $6.6\,\mathrm{km\,s^{-1}}$ in velocity. Doubling the velocity resolution compared to the original observational data stops the Gaussian filter from removing fine velocity features present in the cubes. The same spatial resolution suffices to show all detail in the simulations, although we are able to increase the velocity resolution further to $1.5\,\mathrm{km\,s^{-1}}$.

Each particle is first binned onto the image grid, and for every pixel, a link is stored back to all the particles occupying that pixel. Since the number of particles in a pixel is highly variable and the image has large portions that aren't occupied by the MS or HVCs, we avoid storing a constant amount of memory per pixel and executing costly loops on parts of the image that don't have any flux. Thus the references back to the particles are stored in a hash table that uses the image coordinates and particle index number within that pixel as a key into the hash table.

For each pixel in the image, a smoothing kernel is required such that within a box centred on that pixel, with sides the diameter of the smoothing kernel, at least three particles are found including any in that pixel (Figure 2.8). To limit the size of very low density features, the kernel size is limited to 31 pixels across (or a smoothing radius r_s of 16 pixels), and the minimum size and radius are 1 pixel to ensure that the flux from one particle can still be distributed over a small range of pixels. The box size is found by executing a spiral search pattern (seen in Figure 2.8) while

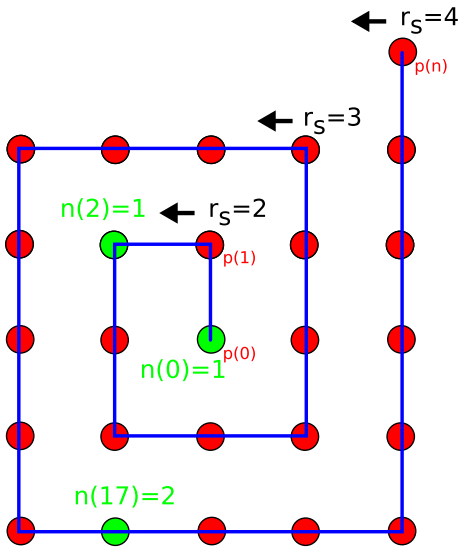

Figure 2.8: The search pattern executed in two dimensions to find the size of the box needed to enclose 3 particles. In this example, the first two pixels with any particles in them are found to have 1 particle each in them, and the third point has two particles. Thus to obtain the necessary three particles for smoothing, we have searched 18 pixels to determine that we need a smoothing radius of $r_s = 3$.

recording the numbers of particles found in each pixel encountered, until the box size needed to enclose at least three particles is known (or the maximum box size is reached). Although the searching box is shaped as a square, once the smoothing radius r_s is obtained for that pixel the applied Gaussian kernel will be circularly symmetrical. The error between the smoothing radius found and the true distance to the third closest particle is at most $\sqrt{2}$, which is not of importance when we are simply attempting to fill the gaps left by the discrete sampling of the underlying DF.

The above scheme has been generalised for the three dimensional case to deal with voxels within a cube. In this case, for voxel (i, j, k), that voxel is first examined for particles, then starting from $R = 2$, and incrementing in steps of 1, spiral searches are performed with a maximum radius of R in each of the two dimensional planes surrounding that voxel, R voxels distant. More precisely, in each of the two–dimensional $y - z$, $x - z$ and $x - y$ planes centred on the voxels $(i \pm (R-1), j, k)$, $(i, j \pm (R-1), k)$ and $(i, j, k \pm (R-1))$ respectively, spiral searches are performed with maximum radius R until the required number of particles are found. Care has to be taken when the second and third axes are being searched, in order to not double count particles within the edge voxels. This is done simply on the $x - z$ axis

by not searching those voxels where x is either of $i \pm (R-1)$, and for the $x-y$ axis by reducing the maximum size of the spiral search to radius $R-1$. Once three particles have been obtained in total within the cube, r_s is set to the obtained R.

Having obtained a smoothing radius associated with every pixel, we can iterate over all particles, ignoring those that have already been dealt with, and find the pixel corresponding to that particle, and then in turn, find all of the particles stored in the hash table corresponding back to that pixel. From each of those particles in the pixel, we sum the flux (column density) from an element or ion species contributed by that particle, and obtain a flux weighted average of the first and second velocity moments and possibly moments of any other quantity associated with them. Those quantities are then distributed around the surrounding area according to the smoothing kernel associated with that pixel. The column density N (in units of cm^{-2}) associated with a single simulation particle is the number of particles of the species of interest contained in a line of sight column of area $1\,\mathrm{cm}^2$, and is obtained by

$$N = M \frac{\mathrm{N_A}}{\mu} \frac{1}{A_\mathrm{p}}, \tag{2.54}$$

where $\mathrm{N_A} = 6.02 \times 10^{23}/\mathrm{mol}$ is Avogadro's constant, μ is the molar mass of the species of interest (for H I column density, hydrogen has a molar mass of $1\,\mathrm{g/mol}$, for C IV and O VI, the molar mass of carbon and oxygen is 12 and $16\,\mathrm{g/mol}$ respectively, and the ionisation fraction of C IV and O VI are taken to vary as a function of temperature; see Figure 2.6). M is the mass in grams contributed by that species within that simulation particle (for N-body–only simulations, a fixed hydrogen mass fraction of 0.76 is assumed, and in some cases, we obtain the oxygen mass by assuming a minimum $[\mathrm{O/H}] = -0.5$, where $(\mathrm{O/H})_\odot = 5.45 \times 10^{-4}$; Holweger, 2001), and A_p is the area of the pixel in square centimetres at the distance $d\,\mathrm{cm}$ to the particle, and is calculated with reference to the geometry of the projection used (see Figure 2.9). From Equations (2.41) and (2.42) for the ZEA projection, the 4π steradians of the sky are bound in the image plane by

$$\sqrt{x^2 + y^2} \leq 360/\pi, \tag{2.55}$$

giving an area in the image plane of

$$A_\mathrm{s} = 360^2/\pi, \tag{2.56}$$

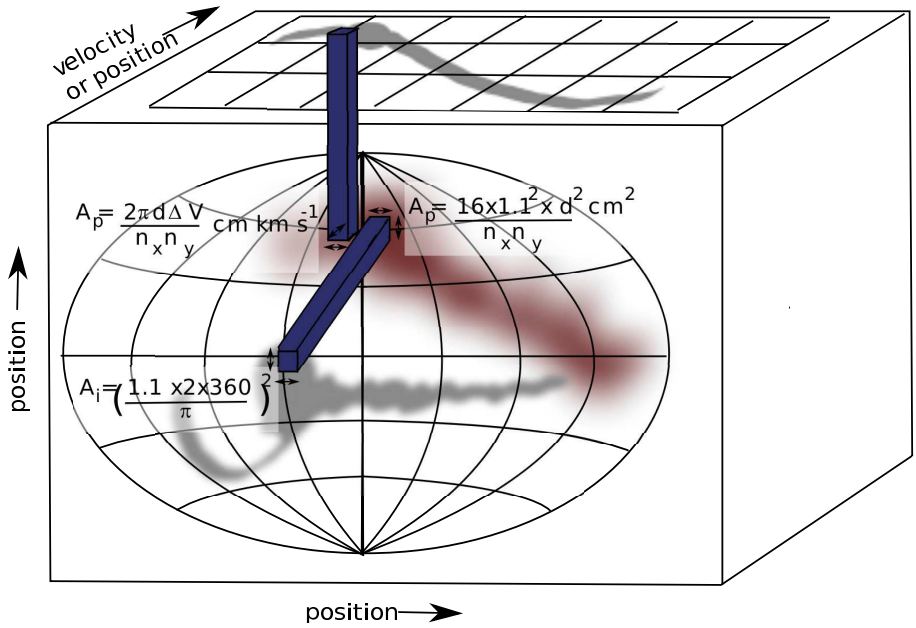

Figure 2.9: A schematic view of how the simulation or observational cube is projected in order to obtain moment maps in two dimensions. In this case, the three-dimensional object (in either position–position–velocity or position–position–position space) being projected is shown in red, and is either projected onto the sky in position–position space, or projected to yield a position–velocity map. The physical area A_p of each pixel (projected in blue) to the location of the object is shown in both cases from Equations (2.62) and (2.67), and this area is able to yield the column density via Equation (2.54).

and in physical space of

$$A = 4\pi d^2 \,\mathrm{cm}^2. \tag{2.57}$$

We choose for the sky to be completely enclosed within the (square) image with a 10% margin in order to be able to smooth the image, to give bounds of

$$-\frac{360}{\pi} \times 1.1 < x < \frac{360}{\pi} \times 1.1 \tag{2.58}$$

$$-\frac{360}{\pi} \times 1.1 < y < \frac{360}{\pi} \times 1.1, \tag{2.59}$$

giving an image area of

$$A_\mathrm{i} = \left(\frac{1.1 \times 2 \times 360}{\pi}\right)^2. \tag{2.60}$$

The image is divided into n_x by n_y pixels, and thus the number of pixels covering the actual sky within the image is

$$n = \frac{A_\mathrm{s}}{A_\mathrm{i}} n_\mathrm{x} n_\mathrm{y}, \tag{2.61}$$

giving a physical area per pixel at distance d cm of

$$A_{\rm p} = \frac{A}{n} = \frac{4\pi d^2}{n_{\rm x} n_{\rm y}} \frac{A_{\rm i}}{A_{\rm s}} = \frac{16 \times 1.1^2 d^2}{n_{\rm x} n_{\rm y}} \,{\rm cm}^2. \tag{2.62}$$

Similarly for the AIT projection, from Equations (2.49) and (2.50), the sky is bound in the image plane by

$$\sqrt{\left(\frac{x}{2}\right)^2 + y^2} \leq \frac{180\sqrt{2}}{\pi} \tag{2.63}$$

and the image bounds are chosen to be

$$-\frac{360\sqrt{2}}{\pi} \times 1.1 < x < \frac{360\sqrt{2}}{\pi} \times 1.1 \tag{2.64}$$

$$-\frac{180\sqrt{2}}{\pi} \times 1.1 < x < \frac{180\sqrt{2}}{\pi} \times 1.1 \tag{2.65}$$

leading to both $A_{\rm s}$ and $A_{\rm i}$ being unchanged from Equations (2.56) and (2.60) in the ZEA projection, and resulting in the same pixel area $A_{\rm p}$ from Equation (2.62). An analogous procedure is performed to obtain a surface density of gas, stars or DM, instead of column density, in units of $\,{\rm M}_\odot/\,{\rm pc}^2$.

We can also produce moment maps of unconventional dimensions. A position-velocity map and position-radius map can be produced to show the trend of velocity or distance across the MS (the latter only within simulations). By adopting the Magellanic longitude as one image axis and radial velocity as the other, the image area in physical space for the given particle at distance d cm, is

$$A = 2\pi d \Delta V \,{\rm cm\,km\,s^{-1}}, \tag{2.66}$$

where d is the distance to the particle in cm, and ΔV is the velocity range of the map in $\,{\rm km\,s^{-1}}$. Thus the physical area per pixel is

$$A_{\rm p} = \frac{2\pi d \Delta V}{n_{\rm x} n_{\rm y}} \,{\rm cm\,km\,s^{-1}}, \tag{2.67}$$

where $n_{\rm x}$ and $n_{\rm y}$ are again the image dimensions. This yields a column density in Equation (2.54) in units of $({\rm cm\,km\,s^{-1}})^{-1}$.

If the radial distance d, was made the second dimension in the moment maps,

the image area in physical space is

$$A = 2\pi d \Delta D \, \mathrm{cm}^2, \tag{2.68}$$

where d is the distance to the particle in cm, and ΔD is the range in radial distances in cm, in the map. The physical area per pixel is

$$A_\mathrm{p} = \frac{2\pi d \Delta D}{n_\mathrm{x} n_\mathrm{y}} \, \mathrm{cm}^2, \tag{2.69}$$

yielding a conventional column density in Equation (2.54), with the map being viewed essentially side-on.

The column density and moments from each of the particles in Equation (2.54) are added into the resultant moment maps or cube via a Gaussian smoothing kernel, defined as

$$G(r, \sigma) = \frac{1}{(2\pi\sigma^2)^{D/2}} e^{-r^2/(2\sigma^2)}, \tag{2.70}$$

where D is the number of dimensions in the output image or cube (2 or 3 respectively), σ is the smoothing radius in number of pixels and r is the distance in pixels, from where the flux originates from to the pixel where the flux is being distributed to. We limit the maximum distance that flux is distributed to, to a circle or sphere of radius 3σ, thereby ensuring that 99% of flux is accounted for in the final image.

To apply this smoothing kernel, for each moment map, a temporary image is constructed such that for every pixel (i, j), with its associated smoothing radius r_s, a box is obtained with sides $2 \times 3r_\mathrm{s} - 1$ pixels long centred on that pixel (except at the edges where the box is truncated). For each pixel $(i_\mathrm{g}, j_\mathrm{g})$ in that box, the temporary image for that moment map is incremented by

$$\left(\sum_{l \in (i,j)} q_l^m N_l \right) G(\sqrt{(i_\mathrm{g} - i)^2 + (j_\mathrm{g} - j)^2}, r_\mathrm{s}), \tag{2.71}$$

where m is the moment number wanted of any quantity q_l (such as velocity, metallicity or temperature), which is weighted by the sum of column density N_l over all particles l within pixel (i, j) obtaining the column density from Equation (2.54). For the column density map, or equivalently the 0th moment, the result is the temporary map with $m = 0$. For other moments, the result is the temporary image divided by the 0th moment map. This can yield a flux weighted velocity map from

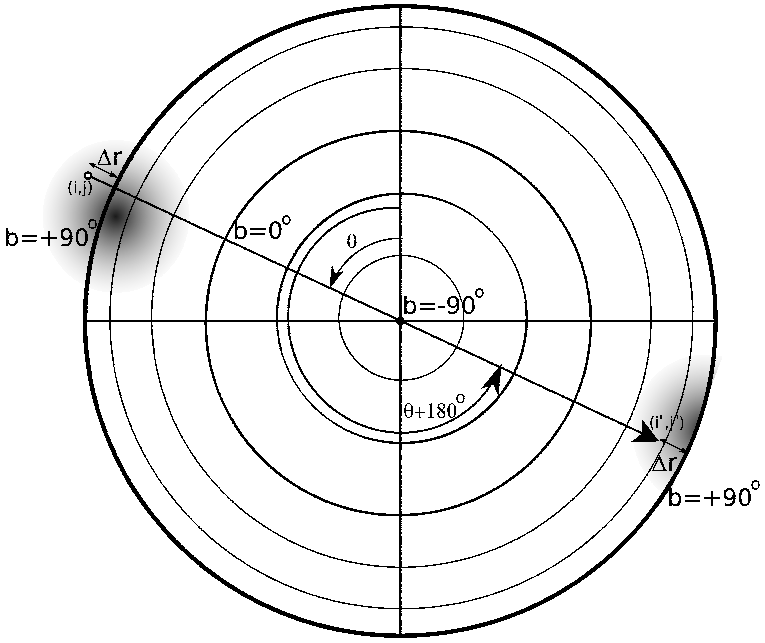

Figure 2.10: Any flux spilled outside valid image areas are remapped back onto valid coordinates approximately corresponding to an identical region of sky. In this example, the flux from one pixel near the edge of the sky in a ZEA projection is smoothed by the Gaussian kernel over the edge of the boundaries at $b = +90°$ on the left, and the flux from outside this area is wrapped back over the $b = +90°$ pole to the right.

the 1st moment of velocity, a flux weighted velocity dispersion map from the 2nd moment, or a flux weighted metallicity or temperature map from the 1st moment of gas metallicity or temperature. Using a variable length smoothing kernel gives us the additional property that the statistical noise in the moment maps are minimised since the kernel always includes within it approximately the same number of particles and hence flux, and individual particles are not able to unduly bias the moments of associated pixels.

Near the outer boundary of the sky, any pixels that contained particles would result in flux being spilled via smoothing into regions without valid sky coordinates according to Equations (2.55) or (2.63). After smoothing the image but prior to dividing the temporary moment maps by the 0th moment, for any pixel (i, j) with non-zero flux found with invalid sky coordinates, the flux is mapped back into a valid region (i', j') that is geometrically adjacent to the closest boundary, as seen in Figure 2.10. For the ZEA projection, where the valid image boundary is defined by $r = 360/\pi$, for a pixel beyond the boundary with location in polar coordinates $\left(\sqrt{x^2 + y^2}, \tan^{-1}[y/x] - 90°\right) = (r, \theta) = (\frac{360}{\pi} + \Delta r, \theta)$ where $\Delta r > 0$, the flux and

moments from that pixel are remapped onto $(\frac{360}{\pi} - \Delta r, 180 + \theta)$. For the AIT projection, where the boundary is defined by $\sqrt{(x/2)^2 + y^2} = \frac{180\sqrt{2}}{\pi}$, a pixel beyond the boundary at location $\left(\sqrt{(x/2)^2 + y^2}, \tan^{-1}[2y/x] - 90^\circ\right) = (\frac{180\sqrt{2}}{\pi} + \Delta r, \theta)$ is remapped onto $(\frac{180\sqrt{2}}{\pi} - \Delta r, -\theta)$.

2.4 Analysis Techniques: Interactive 3D Analysis

2.4.1 Particle Tagging

As well as attempting to reproduce the MS and HVC distributions as observed at the current time, we wish also to track individual features through time to ascertain their origin. We have developed an application that allows the user to select particle groupings in a two dimensional distribution using any pair of quantities, with a mouse pointer. The most common use of this feature is to select particles as they appear on the sky in two dimensions, but we have also used this application to select particles based on their radial distance from the Sun, their velocity, their temperature, or the flux emitted from individual particles, as a function of their location in one spatial dimension. To aid the selection of particles in high density regions, a corresponding moment map can be underlaid below the particle data on the screen.

Once the user selects a polygon, a point–in–polygon algorithm (Haines, 1994) is applied to find all particles within that polygon, and all pixels within the polygon in the optional moment map, as illustrated in Figure 2.11. The particle ID of such particles are then recorded and the user can toggle whether or not to plot these newly flagged particles and/or pixels.

In both the MS and HVC simulations, we categorise all particles at the final timestep into non-overlapping sets based on their geometrical properties, recording the criteria used to delineate each set. These criteria are reused on each MS model in the parameter survey, in order to quantitatively find the model that best reproduces the stream. In the hydrodynamic HVC simulations, particles can be both converted between gas and star particles. Thus tagging of gas particles based on their configuration at the final time will lead to some particles that can't be tagged if they are converted to stars before the final timestep. These "lost" particles are all given another categorisation that can be tracked throughout the timesteps.

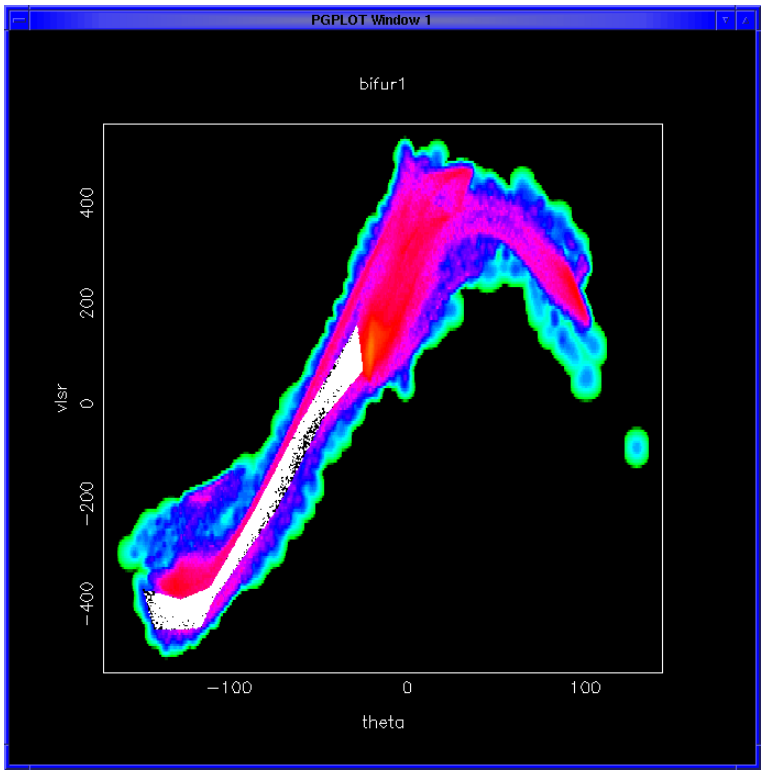

Figure 2.11: Tagging of the points (and pixels) within a polygon selected by the user, showing how we select components of the systems being studied. Shown is one selected component (highlighted in white) of the final output of a simulation, which is then tagged and analysed separately.

2.4.2 Interactive Time Evolution

While projecting particles onto the sky as moment maps allows an approximate understanding of the distribution of the gas, one often wants to inspect the simulations using three–dimensional visualisation. There are two main ways in which we can inspect the simulations using 3D visualisations. Ray tracing (or volume rendering) software can be used to construct a realistic transfer function that mimics the result of looking through semi-opaque gas. Using ray tracing visualisation software such as XRAY (Gooch, 1996), OPENDX (OpenDX.org, 2003), or DVR (Beeson et al., 2003) is very expensive in terms of both memory and CPU power required, and the rendered results are often too complicated to enable the ready interpretation of features when looking at just one timestep, and require far too high processing requirements to be able to look at time evolution of the dataset. The second method of projecting the particles onto the two–dimensional screen in an interactive fashion allows an approximate understanding of the distribution of gas using much fewer resources. We use a simple but powerful OPENGL interface instead (Gill et al., 2004).

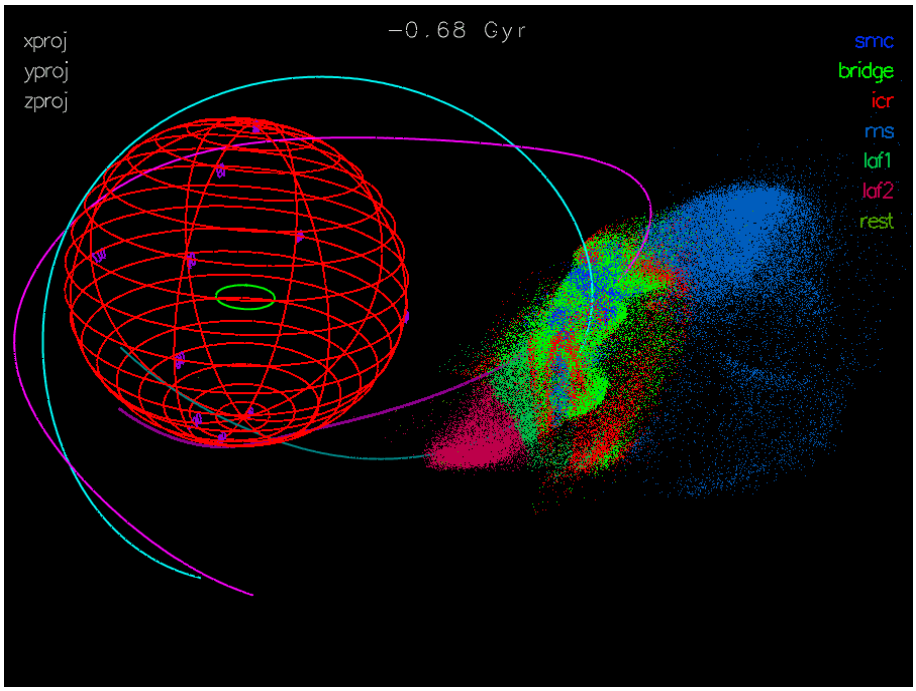

Figure 2.12: Screengrab of a movie produced from an interactive particle visualisation with tagging applied. All components in the final output of the example simulation had been tagged as in Figure 2.11, and the simulation was interactively shown (or converted to a movie) with this tagging applied (a legend is shown on the right hand side of the image, briefly labelling each component). In this case, a grid is shown corresponding to the galactic latitude and longitude at a projected radius of 50 kpc from the Sun, and the orbit of the Sun in the Galactic disc is shown as a green circle. The orbits of the LMC and SMC are denoted by a magenta and cyan lines, respectively.

Used on sufficiently powerful hardware, all particles can be loaded into linked lists stored on the graphics card itself. A separate list of particles is kept for all timesteps, and swapping between timesteps is a trivial operation of swapping pointers to the relevant particle list, and hence is very fast. Tagged particles can be turned on and off to highlight the evolution of the components of the simulation we are interested in. With the aid of interactively added keyframes which encode the positioning of the "camera" relative to the simulation and the time within the simulation, a movie can be generated linking the keyframes via smooth motion in time and space. A screengrab from such a movie is shown in Figure 2.12.

In this chapter, we have discussed the GCD+ code and the analysis software used to study the simulation output. We have also discussed the analysis techniques used

on both the observational and simulation data to enable direct comparison between the two. In the next two chapters, we will apply these codes to two important examples of hierarchical clustering in action in the Local Group.

Chapter 3

N-body Simulations of the Magellanic Stream

Summary

A suite of high-resolution N-body simulations of the Magellanic Clouds (MCs)–Milky Way (MW) system are presented and compared directly with newly available data from the H I Parkes All-Sky Survey (HIPASS). We show that the interaction between Large and Small Magellanic Clouds (LMC and SMC) results in a spatial and kinematical bifurcation of both the Stream and the Leading Arm. The spatial bifurcation of the Stream is readily apparent in the HIPASS data, and the kinematical bifurcation is also tentatively identified. This correct prediction of the observed bifurcation provides strong support for the tidal disruption origin for the Magellanic Stream. A fiducial model for the MCs is presented upon completion of an extensive parameter survey of the potential orbital configurations of the MCs and the viable initial boundary conditions for the disc of the SMC. The impact of the choice of these critical parameters upon the final configurations of the Stream and Leading Arm is discussed. A preliminary model including star formation physics is also presented.

3.1 Introduction

The progressive collapse and merging associated with hierarchical clustering within a Cold Dark Matter (CDM) cosmology, while dominated by activity at early epochs (redshifts $z \sim 2$ – 5; e.g. Murali et al., 2002), continues to the present-day and is readily observable in the local Universe. In our own Milky Way (MW), ongoing satellite disruption and accretion events include the Sagittarius dwarf (Ibata et al.,

1994), the Canis Major dwarf (Martin et al., 2005, and references therein), and perhaps the most spectacular of all, the Large Magellanic Cloud (LMC) and Small Magellanic Cloud (SMC). The disruption and accretion of the Magellanic Clouds (MCs) is perhaps best appreciated through the Magellanic Stream (MS), an arc of gas stretching 180° across the sky on a polar orbit, emanating from the MCs (Mathewson et al., 1974; Putman et al., 1998, hereafter P98).

Two primary, competing, scenarios have been postulated to explain the origin of the MS: (i) ram pressure stripping of LMC and SMC gas due to the motion of the MCs through the tenuous coronal gas in the Galactic halo (Moore & Davis, 1994; Mastropietro et al., 2005), and (ii) the tidal disruption of the SMC (Murai & Fujimoto, 1980). The "drag" scenario of the ram pressure stripping model faces difficulty in explaining the Leading Arm Feature (LAF) observed by P98, which shows a leading stream of gas stretching at least 30° in front of the MCs towards the Galactic plane. The ability of the tidal disruption model to simultaneously produce both trailing and leading streams of gas has caused it to gather considerable support in the literature (Gardiner & Noguchi, 1996; Gardiner, 1999; Yoshizawa & Noguchi, 2003, hereafter, GN96, G99 and YN03 respectively), although the existence of bright Hα emission within the MS (Weiner & Williams, 1996; Putman et al., 2003a) is evidence that there must at least be some additional effect from ram pressure stripping.

Constraints upon theoretical models of the MS have improved dramatically with the release of the H I Parkes All-Sky Survey (HIPASS; Barnes et al., 2001) dataset. The extent and fine-scale structure of the MS can now be appreciated to a level not previously possible, in particular the unequivocal evidence for the existence of the LAF (P98). Motivated by HIPASS, we have initiated a program of high-resolution N-body modelling of the MS aimed at de-constructing the temporal evolution of the MCs–MW interaction. Here, we use ~ 30 times higher resolution than previous models such as GN96, G99 and YN03[1], giving us a H I mass resolution of $\sim 5600\,\mathrm{M}_{\odot}$ and a H I flux resolution of $7\,\mathrm{Jy\ km\,s^{-1}}$. In addition, we construct a detailed H I map to compare with the HIPASS data directly and quantitatively. The combination

[1]Bekki & Chiba (2005) have presented high-resolution simulations of the MS, focusing exclusively on the internal dynamics and star formation history of the LMC by fixing the potentials of both the MW and SMC- i.e., predictions concerning the formation and evolution of the MS and LAF were not part of their work. The mass resolution employed in our work is approximately a factor of ten greater, and the softening length a factor of two less than that of Bekki & Chiba (2005).

of a higher resolution simulation and the simulated H I map enables us to study more detailed features in the MS and the LAF. As a result, this work shows more convincingly that the observed LAF and MS can be produced by the leading and trailing streams of the SMC, induced by tidal interactions with the MW and LMC.

Our fiducial model is found after an extensive parameter search of the potential orbital configurations of the MCs and the different possible initial conditions of the SMC. Based on our parameter search, we also demonstrate how the final features of the MS and the LAF are sensitive to the initial configuration of the SMC in a parameter survey surrounding this fiducial model. Our new, high-resolution simulations also reveal that the tidal interactions create spatial and kinematical bifurcation in the MS and LAF. We present this prediction based on our simulations, and go on to demonstrate that the existing HIPASS data also show such bifurcations. We do not concentrate on the gas physics involved in the interaction of the MCs and we do not model either of the MW or LMC with "live" particles, since Li (1999), Maddison et al. (2002) and YN03 demonstrate that the overall features of the streams are unchanged by the addition of such physics. However, we show that the fiducial N-body model can be extended to include gas physics and star formation, such that the modelled streams retain the same basic shape.

The layout of this chapter is as follows: In Section 3.2, we give the procedure used in generating initial conditions and identifying a best "fiducial" model for the MC simulations in a parameter search, as well as examining how the parameters affect the modelled stream in a parameter survey. We provide a description of the suite of simulations generated to date, and how they were generated. Here, we concentrate mostly upon the effects of gravity, describing the SMC disc with collisionless particles, and ignore the baryon physics (including hydrodynamics, star formation, energy feedback, and chemical enrichment) in all but two models. Despite being modelled by collisionless particles, the gas is expected to behave realistically in regions of low density, i.e., in the bulk of the MS and LAF. In Section 3.3, we show the results from our best model, and compare them with the observational data. In Section 3.4, we demonstrate how the final features of the MS and LAF depend upon the orbits of the MCs and the initial properties of the SMC disc. In Section 3.5, we highlight a possible future direction of this research by showing some preliminary Smooth Particle Hydrodynamical (SPH) gas models of the MS. Finally, in Section 3.6, the discussion and future directions for our work are presented.

3.2 Numerical Simulation

The framework upon which our simulations are based parallels that described by GN96 and YN03. In our models, we set up a three galaxy system containing the MW, LMC and SMC. The MW and LMC are taken to be fixed potentials, while the SMC is treated as an ensemble of self-gravitating particles, in recognition of the fact that the MS is thought to originate from the tidal disruption of the SMC disc (e.g. Gardiner et al., 1994, hereafter GSF94; GN96; Maddison et al., 2002; YN03; Růžička et al., 2007; but see also Mastropietro et al., 2005). The SMC is assumed to consist of a gaseous and stellar disc and a Dark Matter (DM) halo. The orbits of the MW and LMC with respect to the SMC are pre-calculated, the procedure for which is outlined in Section 3.2.1 and GSF94. This section also deals with the search for, and production of initial boundary conditions for the "live" SMC model, set up using GalactICs (Kuijken & Dubinski, 1995). We test for the stability of these models in Section 3.2.2. Their evolution using the GCD+ tree N-body code (Kawata & Gibson, 2003a) is explored in Section 3.2.3.

3.2.1 Initial conditions

The Orbits of the LMC and SMC

In order to prescribe the orbits of the MCs, we first need to set up the potentials of the central MW and the LMC. The halos of both the MW and LMC are assumed to be invariant for the duration of the simulation (2.5 Gyr—i.e., a lookback time corresponding to redshift $z \sim 0.2$ in the concordance cosmology). There is little disc contribution to the MW potential at the typical Galactocentric distances of the LMC and SMC (~ 50 kpc), and so we assume a spherically symmetric halo potential. CDM models predict that halos both have central cusps and that the outer regions drop off faster than the isothermal sphere (Navarro et al., 1997), however the MCs sample a volume of the halo where the gravitational potential is insensitive to these effects. We hence assume a constant rotational velocity of $V_{\rm c} = 220\,{\rm km\,s^{-1}}$ within the MW halo. These assumptions allow us to describe the potential by

$$\phi_{\rm G}(r) = -V_{\rm c}^2 \ln r \tag{3.1}$$

with a mass enclosed within r kpc of

$$M_{\rm G}(<r) = 5.6\times10^{11}\left(\frac{V_{\rm c}}{220\,{\rm km\,s^{-1}}}\right)^2\left(\frac{r}{50\,{\rm kpc}}\right)\,{\rm M}_\odot. \tag{3.2}$$

Plummer potentials are adopted for both the LMC and SMC—i.e.,

$$\phi_{\rm L,S}(\mathbf{r}) = GM_{\rm L,S}/\left[(\mathbf{r}-\mathbf{r}_{\rm L,S})^2 + K_{\rm L,S}^2\right]^{1/2}, \tag{3.3}$$

where $\mathbf{r}_{\rm L,S}$ are the positions of each of the MCs relative to the MW centre, and $K_{\rm L,S}$ are the core radii, set to 3 and 2 kpc for the LMC and SMC, respectively. We treat the masses of the LMC and SMC as free parameters, however in the fiducial model, we assume a constant mass of $M_{\rm L} = 2\times10^{10}\,{\rm M}_\odot$ for the LMC, and $M_{\rm S} = 3\times10^{9}\,{\rm M}_\odot$ for the SMC. In some models, we also test the effect of varying the mass of the SMC $M_{\rm S}$ linearly with time to approximate mass lost from the SMC, but this does not affect the orbit noticeably.

The equations of motion of the MCs about the stationary MW are

$$\ddot{\mathbf{r}}_{\rm L} = \frac{\partial}{\partial\mathbf{r}_{\rm L}}\left[\phi_{\rm S}\left(|\mathbf{r}_{\rm L}-\mathbf{r}_{\rm S}|\right) + \phi_{\rm G}\left(|\mathbf{r}_{\rm L}|\right)\right] + \mathbf{F}_{\rm L} \tag{3.4}$$

and

$$\ddot{\mathbf{r}}_{\rm S} = \frac{\partial}{\partial\mathbf{r}_{\rm S}}\left[\phi_{\rm L}\left(|\mathbf{r}_{\rm S}-\mathbf{r}_{\rm L}|\right) + \phi_{\rm G}\left(|\mathbf{r}_{\rm S}|\right)\right] + \mathbf{F}_{\rm S}, \tag{3.5}$$

where the potentials $\phi_{\rm L}$, $\phi_{\rm S}$ and $\phi_{\rm G}$ refer to the LMC and SMC, and the Galaxy, respectively (Murai & Fujimoto, 1980). Since we do not model the MW with live particles, dynamical friction is modelled as per GSF94 via a dampening force. $\mathbf{F}_{\rm L}$ and $\mathbf{F}_{\rm S}$ are the dampening force between the Galaxy and each of the MCs:

$$\begin{aligned}\mathbf{F}_{\rm L,S} &= \frac{-GM_{\rm L,S}}{\left|\mathbf{r}_{\rm L,S}\right|^2}\ln(\Lambda)\,\frac{\dot{\mathbf{r}}_{\rm L,S}}{\left|\dot{\mathbf{r}}_{\rm L,S}\right|} \\ &\quad\times\left\{\frac{2\left[\int_0^x \exp(-y^2)dy - \exp(-x^2)x\right]}{\pi^{1/2}x^2}\right\}_{x=\left|\dot{\mathbf{r}}_{\rm L,S}\right|/V_{\rm c}},\end{aligned} \tag{3.6}$$

where $\ln(\Lambda)$ is the Coulomb logarithm.

Although Equation (3.6) is a simple analytical formulation for dynamical friction that fails to model accurately the orbit of the MCs for more than 5 Gyr, according to recent studies (Hashimoto et al., 2003; Just & Peñarrubia, 2005), it gives a good approximation to the predictions of full N-body simulations over the $\sim$ 2.5 Gyr

Table 3.1: Present-day orbital parameters for the SMC and LMC synthesised from the literature, and values we have adopted in this work.

Parameter	LMC		SMC	
	Literature	This work	Literature	This work
$v_{\rm r,GSR}$ [a]	80±3 [1,2]	80.1	14.3±0.6 [3,4,5,6]	7.1
$v_{\rm t,GSR}$ [b]	369±18 [1,2]	287	300±50 [6,7]	255
l [c]	280°.46 [8]	280°.46	302°.79 [8]	302°.79
b [d]	−32°.89 [8]	−32°.89	−44°.30 [8]	−44°.30
d [e]	49.43 [9]	49.43	57.02 [9]	57.02

[a] Radial velocity ($\rm km\,s^{-1}$) in the Galactic Standard of Rest, [b] Tangential velocity ($\rm km\,s^{-1}$) in the Galactic Standard of Rest, [c] Galactic longitude, [d] Galactic latitude, and [e] Distance (kpc).
[1] van der Marel et al. (2002), [2] Kallivayalil et al. (2006b), [3] Hardy et al. (1989), [4] GSF94, [5] Harris & Zaritsky (2006), [6] Kallivayalil et al. (2006a), [7] Lin et al. (1995), [8] Tully (1988), and [9] Feast & Walker (1987).

lookback times focused on in this work. We note also the strong effect the Coulomb logarithm has on the orbits. Binney & Tremaine (1987) advocate for the MCs, $\ln(\Lambda) = 3$, although Hashimoto et al. (2003) suggest that this is perhaps too large for the LMC, causing the system to evolve too fast. We set $\ln(\Lambda) = 3$ to enable direct comparisons with the previous works, although we experiment with other values from $\ln(\Lambda) = 1.5$ to 6.

Adopting these parameters, we backwards integrate (and forwards integrate to obtain orbits into the future) the orbits of the SMC and LMC with a Runge-Kutta algorithm, using as boundary conditions the current tangential and radial velocities and positions of the MCs listed in Table 3.1 (see also Murai & Fujimoto, 1980; GSF94; GN96; Lin et al., 1995; Bekki et al., 2004). The values we adopted for our work were chosen to match those of GN96 while remaining largely consistent with the extant literature within the errors of the observations. Some of the newer proper motions of the LMC are deviating somewhat, leading some to propose that the MCs are only on their first orbit (Kallivayalil et al., 2006a; Besla et al., 2007; Piatek et al., 2008), although other uncertainties, such as the shape of the MW halo (whether it is oblate, spherical or prolate; Helmi, 2004a,b; Johnston et al., 2005; Růžička et al., 2007), the magnitude of any dynamical friction between the MCs and the MW (Hashimoto et al., 2003), and the magnitude of any dynamical friction between the MCs themselves (Bekki & Chiba, 2005), may dominate. We note that these unconstrained parameters that affect the orbit will also affect the stream, and thus such parameters of the orbit are still largely free for us to determine with a

best fit to the observed stream.

Our fiducial model is initiated at a lookback time of 2.5 Gyr when the MCs are at apo-Galacticon (with the tidal forces between all three bodies being minimised). The subsequent orbit appears in Figure 3.1, and the distance between the MCs and Galaxy is shown in Figure 3.2. From the distances between the three bodies, illustrative tidal forces calculated from the inverse cube of the distance are also shown in Figure 3.2, showing a strong peak in the tidal field between the LMC and SMC in the most recent encounter. The tidal forces on the SMC are increased further than illustrated here, as it expands during the evolution of the system.

Construction of the Initial Conditions

It is important that the initial conditions for the SMC are in equilibrium, and that the potentials of the disc and halo used to establish the particle configuration are self consistent. In our N-body simulations, any transient instabilities when the SMC is placed in the tidal field of the fixed LMC and MW potentials may result in artificial heating. There is also the opportunity for artificial transients to occur when gravitational softening is employed, as detailed in Section 2.2.1, as the forces are modified from those assumed in the calculation of the initial conditions. Any bar instabilities resulting from inadequate numerical resolution should not overwhelm the SMC disc. In SPH simulations, we also require a disc with a stellar component in equilibrium with the gas component, such that the disc does not suffer from a spike of star formation at the start of the simulation. Such a spike may lead to catastrophic artificial heating of the disc, or result in artifacts in the chemodynamical evolution of the system. In all simulations herein, after generating the initial conditions, we verify (in Section 3.2.2) that any initial transients do not overwhelm the subsequent simulation.

We construct the SMC particle initial conditions using GalactICs (Kuijken & Dubinski, 1995). GalactICs implements a three component model of a galaxy consisting of a bulge, disc, and halo. In simulating the SMC dwarf irregular galaxy, we neglect a bulge component as no such component is observed. We can observationally constrain properties of the gas disc, but are free to experiment with properties of the DM halo within a reasonable range. Since it is hypothesised that the inter-cloud region (ICR), MS and LAF components all originated from the SMC, the initial H I mass of the SMC prior to encounters with the MW and LMC is taken to be the sum

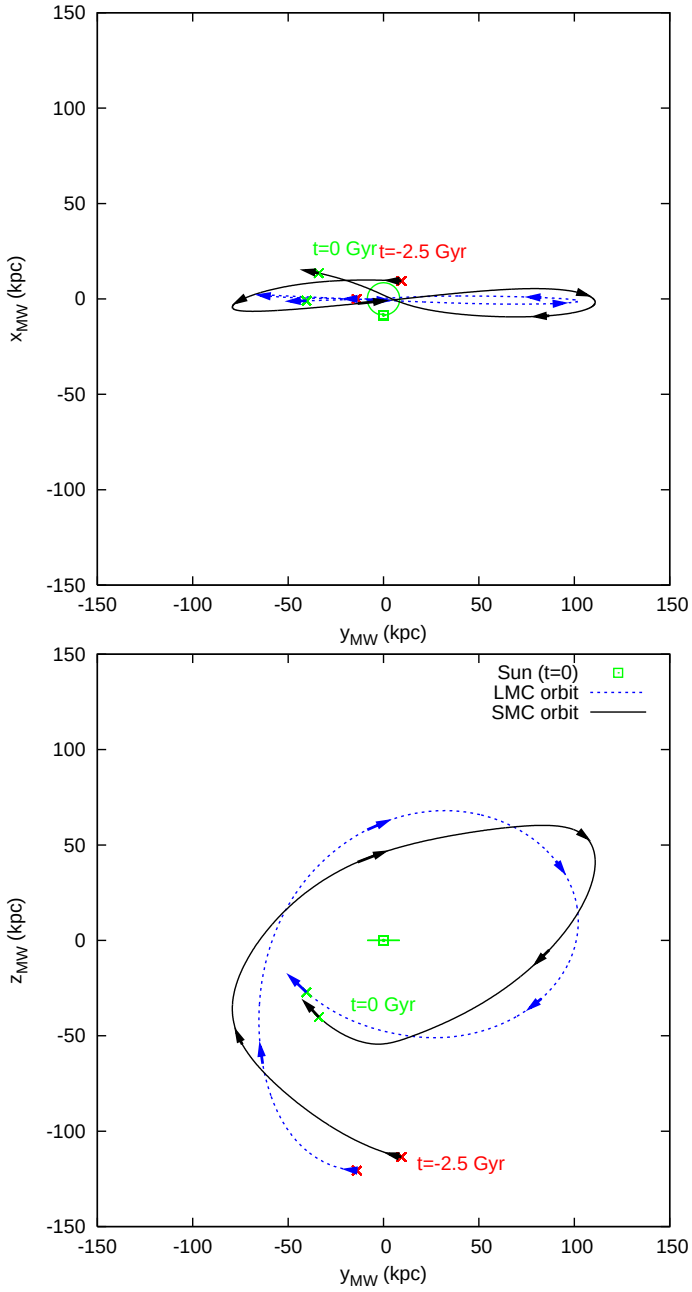

Figure 3.1: The three dimensional orbit projected into the x-y plane (top) and z-y plane (bottom) of the SMC (black line) and the LMC (blue dashed line) around the Galaxy. The rotation axis of the MW is assumed to be the z-axis, and the disc plane is centred on $z = 0$. The orbits, which are derived by backwards integrating to $T = -2.5\,\mathrm{Gyr}$, are plotted with arrows indicating each $0.5\,\mathrm{Gyr}$ between $T = 0$ and $-2.5\,\mathrm{Gyr}$. The green crosses denote the current position of the SMC and LMC. The solar radius at $8.5\,\mathrm{kpc}$ is also shown, and the current position of the Sun at $T = 0$ is marked by the open square.

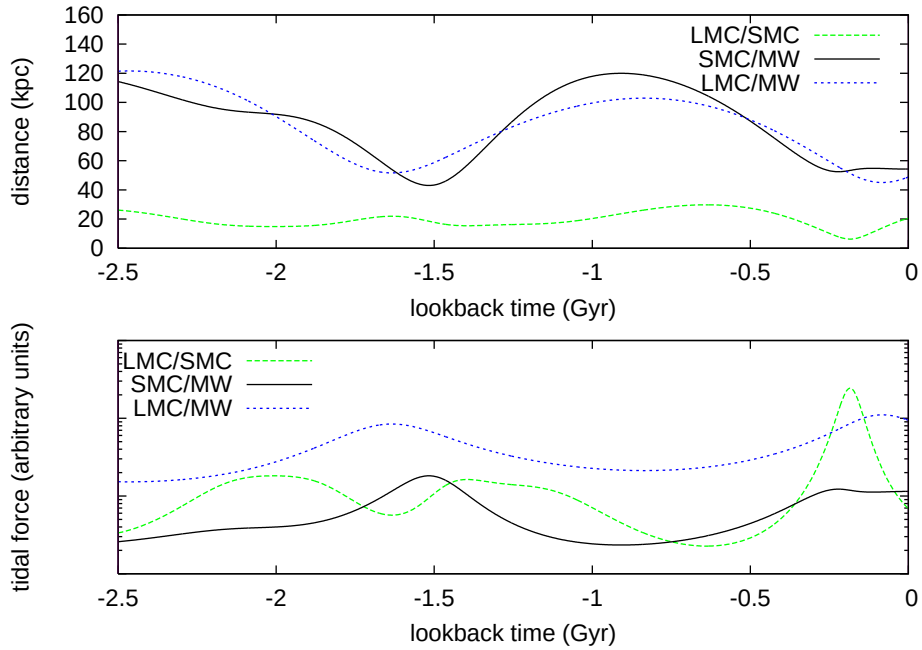

Figure 3.2: Distance (upper) and approximate tidal forces (lower; on a logarithmic scale in arbitrary units, neglecting the increase in size of the SMC as it evolves) between the three interacting bodies in our fiducial model.

of the current H I masses within the SMC, MS, LAF and ICR. A summary of observational constraints for the original SMC (as well as associated parameter space searched in our parameter survey) are presented in Table 3.2. We add this H I mass to the current stellar mass and find that an initial disc mass of $1.5 \times 10^9\,\mathrm{M}_\odot$ is well within the allowable range. The initial total mass is obtained similarly, substituting the current total dynamical mass of the SMC in place of the current H I and stellar masses of the SMC, giving a typical initial total mass of $3.0 \times 10^9\,\mathrm{M}_\odot$. We thus adopt these disc and total mass parameters for our fiducial SMC model.

Using GalactICs (see the full details in Kuijken & Dubinski, 1995), the combined potential of the disc and halo is constructed according to Poisson's equation, with

$$\nabla^2\Psi(R,z) = 4\pi G[\rho_{\mathrm{halo}}(R,\Psi) + \rho_{\mathrm{disc}}(R,\Psi,\Psi_z)]. \tag{3.7}$$

The Distribution Function (DF) of the DM halo is constructed using the lowered Evans (1993) flattened generalisation (Kuijken & Dubinski, 1994) of the King (1962) profile. The lowering process imposes a maximum energy on the particles in the halo allowing a halo of finite size unlike the usual Evans profile. The first term in

Table 3.2: Empirical and simulated (both in the fiducial model, and the ranges surveyed over in the parameter searches and survey) characteristics of the SMC. In the fiducial model, the simulated characteristics in brackets are those derived from the output of the simulation at the current time, with the non-bracketed parameters being those input into the simulation. To set realistic initial conditions pre-encounter, some empirical properties have been taken from isolated SMC-like dwarfs.

Parameter	Fiducial model	Surveyed range	Observation	References
H I mass within SMC ($10^9\,M_\odot$)	(0.49)	–	0.35 – 0.56	(1),(2),(3),(4)
H I mass within MS ($10^9\,M_\odot$)	(0.24)	–	0.1 – 0.5	(5),(6)
H I mass within LAF ($10^9\,M_\odot$)	(0.07)	–	0.03 – 0.06	(7),(8)
H I mass within ICR ($10^9\,M_\odot$)	(0.32)	–	0.05 – 0.65	(9),(10),(11)
Stellar mass within SMC ($10^9\,M_\odot$)	–	–	0.58 – 1.8	(12),(13)
Initial disc (H I) mass ($10^9\,M_\odot$)	1.5	1.1 – 2.0	$1.0 - 2.3^a$	
Total mass within SMC ($10^9\,M_\odot$)	(1.5^b)	–	0.9 – 2.4	(14),(15),(16),(17)
Initial total mass ($10^9\,M_\odot$)	3	3.0 – 3.6	$1.1 - 3.6^c$	
Initial radius of H I disc ($r_{\rm d,95}{}^d$; kpc)	7	3 – 7	$10 - 12^e$	(18)
Initial scale length of H I disc (kpc)	$0.5 \times r_{\rm d,95} = 3.5$	$0.2 - 0.5 \times r_{\rm d,95}$	$1.5 - 4.5^e$	(19)
Initial scale height of H I disc (kpc)	$0.05 \times r_{\rm d,95} = 0.35$	$0.025 - 0.075 \times r_{\rm d,95}$	–	
Initial vel. disp. of H I disc^f ($\sigma_{R,0}$; $\mathrm{km\,s^{-1}}$)	32	25 – 50	~ 25	(20)
Initial radius of DM halo ($r_{\rm h,95}$; kpc)	$1 \times r_{\rm d,95} = 7$	$1 - 1.3 \times r_{\rm d,95}$	–	

References: (1) Brüns et al. (2005), (2) Stanimirović et al. (1999), (3) Stanimirović et al. (2004) who includes He mass, (4) Putman et al. (2003b), (5) Putman et al. (2003b), (6) Brüns et al. (2005), (7) Brüns et al. (2005), (8) Upper limit is obtained by summing LAF ($b < 0°$) mass in P98 with EP and WD (but not WE, since already included in P98) High Velocity Cloud complexes in Wakker & van Woerden (1991), (9) Muller et al. (2003), (10) Putman et al. (2003b), (11) Brüns et al. (2005), (12) Stanimirović et al. (2004), (13) YN03, (14) Dopita et al. (1985), (15) Hardy et al. (1989), (16) Hatzidimitriou et al. (1997), (17) Stanimirović et al. (2004), (18) Swaters et al. (2002), (19) Swaters et al. (2002), (20) this work (Figures 3.12 and 3.13)

[a] The sum of the current observed H I masses within the SMC, MS, LAF and ICR, and stellar mass within the SMC.

[b] DM and gas particles bound within the tidal radius of 9 kpc

[c] The sum of the current total mass within the SMC (obtained dynamically) and H I masses of MS, LAF and ICR. This is likely underestimated because some DM may have been stripped from the SMC.

[d] $r_{\rm d,95}$ is taken to be a basic scaling length of the initial conditions, and is defined by the radius initially containing 95% of the disc particles.

[e] The observed values for SMC-like dwarfs (see text for discussion).

[f] Initial central radial velocity dispersion in simulations, but line of sight velocity dispersion in observation.

Equation (3.7) is the density corresponding to this DF, and is given by

$$\begin{aligned}\rho_{\rm halo}(R,\Psi) &= \tfrac{1}{2}\pi^{3/2}\sigma_0^3(AR^2\sigma_0^2+2B)\mathrm{erf}(\sqrt{-2\Psi}/\sigma_0)\exp(-2\Psi/\sigma_0^2)\\ &\quad+(2\pi)^{3/2}\sigma_0^3(C-B-AR^2\sigma_0^2)\mathrm{erf}(\sqrt{-\Psi}/\sigma_0)\exp(-\Psi/\sigma_0^2)\\ &\quad+\pi\sqrt{-2\Psi}[\sigma_0^2(3A\sigma_0^2R^2+2B-4C)+\tfrac{4}{3}\Psi(2C-A\sigma_0^2R^2)],\end{aligned} \tag{3.8}$$

where $A=\frac{8(1-q^2)G\rho_1^2}{\pi^{1/2}q^2\sigma_0^7}$, $B=\frac{4R_c^2G\rho_1^2}{\pi^{1/2}q^2\sigma_0^5}$ and $C=\frac{(2q^2-1)\rho_1}{(2\pi)^{3/2}q^2\sigma_0^3}$. This DF is thus parameterised uniquely by the potential well depth, Ψ_0, the velocity and density scales, σ_0 and ρ_1, the flattening parameter, q, and the halo core radius, $R_{\rm c}$. In place of the density scale ρ_1, a characteristic halo radius, $R_{\rm a}=\left(\frac{3}{2\pi G\rho_1}\right)^{1/2}\sigma_0 e^{\Psi_0/2\sigma_0^2}$, is used in our calculations. The halo core radius $R_{\rm c}$ is set so that the central density is $\rho_{\rm c}=9k^2\sigma_0^2/4\pi GR_{\rm c}^2$, where the ratio k of the core radius $R_{\rm c}$ (the core radius of the potential prior to lowering the DF) to the King radius $R_{\rm K}$ (the core radius of the density profile corresponding to the Binney potential; Kuijken & Dubinski, 1994) lies between 0.3 and 1. In place of the core radius $R_{\rm c}$, we use the core smoothing parameter, $c=(r_{\rm c}/r_{\rm K})^2=k^2$. These 5 parameters, summarised in Table 3.3 for our chosen models, form the GalactICs input parameters for the SMC halo in our simulations. Since the halo model is not determined simply from the mass profile, but instead from the DF, the input parameters can not be chosen as a simple linear function of the desired halo properties. We must evaluate halo models consistently with the disc using GalactICs manually, iterating in a process described below, until we obtain a model with halo and disc properties that resemble the initial conditions we are seeking (i.e., those in Table 3.2).

The second term in Equation (3.7) is the density of the disc, which is iteratively adjusted when solving for the self-consistent disc+halo potential, until it is approximately radially exponential with scale length $R_{\rm d}$, and with a smooth truncation in radius from $R_{\rm t}$ to $R_{\rm t}+\delta R_{\rm t}$. Thus the disc DF is approximated by (Kuijken & Dubinski, 1995)

$$\rho_{\rm disc}(R,z)=\frac{M_{\rm d}}{8\pi R_{\rm d}^2z_{\rm d}}e^{-R/R_{\rm d}}\mathrm{erfc}\left(\frac{r-R_{\rm t}}{2^{1/2}\delta R_{\rm t}}\right)\exp\left[-0.8676\frac{\Psi_{\rm z}(R,z)}{\Psi_{\rm z}(R,z_{\rm d})}\right], \tag{3.9}$$

where $\Psi_{\rm z}(R,z)=\Psi(R,z)-\Psi(R,0)$, and is typically arranged such that the vertical light profile is similar to the $\mathrm{sech}^2(z)$ dependence expected of a vertically isothermal, self-gravitating sheet. The vertical profile is arranged to drop from the mid-plane value by a factor of $\mathrm{sech}^2(1)\approx e^{-0.8676}$ at a height of $z_{\rm d}$. $R_{\rm t}$ is an artificial truncation

Table 3.3: Dimensionless GalactICs input parameters (see the accompanying text and Kuijken & Dubinski, 1995 for more details on parameters), with scaling factors, for models explored in the parameter survey. Each model is described below, and the outputs for each model are shown in Table 3.4.

Model	Disc						Halo					Scaling multipliers		
	$M_{\rm d}$	$R_{\rm d}$	$R_{\rm t}$	$z_{\rm d}$	$\delta R_{\rm t}$	$\sigma_{\rm R,0}$	Ψ_0	σ_0	q	c	$R_{\rm a}$	Radius	Speed	Mass
	(1)	(2)	(3)	(4)	(5)	(6)	(7)	(8)	(9)	(10)	(11)	(kpc)	($\mathrm{km\,s^{-1}}$)	($10^9\,\mathrm{M_\odot}$)
MW-A	0.87	1.0	5.0	0.1	0.5	0.47	−4.60	1.00	1.0	0.1	0.80	1.1	42.8	0.47
fiducial	1.75	2.0	4.0	0.2	0.6	0.6	−1.65	0.50	1.0	0.1	0.55	1.8	58.9	1.41
very conc.	1.75	0.8	4.0	0.2	0.6	0.6	−3.10	0.81	1.0	0.1	0.82	1.8	46.7	0.89
concen.	1.75	1.4	4.0	0.2	0.6	0.6	−2.21	0.60	1.0	0.1	0.62	1.8	52.0	1.10
thin	1.75	2.0	4.0	0.1	0.6	0.6	−1.58	0.50	1.0	0.1	0.60	1.8	59.2	1.43
hot	1.75	2.0	4.0	0.2	0.6	1	−1.65	0.50	1.0	0.1	0.55	1.8	58.9	1.41
3kpc	1.75	2.0	4.0	0.2	0.6	0.6	−1.65	0.50	1.0	0.1	0.55	0.8	90.0	1.41
5kpc	1.75	2.0	4.0	0.2	0.6	0.6	−1.65	0.50	1.0	0.1	0.55	1.2	69.7	1.41
6kpc	1.75	2.0	4.0	0.2	0.6	0.6	−1.65	0.50	1.0	0.1	0.55	1.5	63.6	1.41
6.5kpc	1.75	2.0	4.0	0.2	0.6	0.6	−1.65	0.50	1.0	0.1	0.55	1.6	61.1	1.41
extended	1.75	2.0	4.0	0.2	0.6	0.6	−1.43	0.49	1.0	0.1	0.79	1.8	59.0	1.42
halo	1.75	2.0	4.0	0.2	0.6	0.6	−2.37	0.63	1.0	0.1	0.55	1.8	50.3	1.03
disc	1.75	2.0	4.0	0.2	0.6	0.6	−1.01	0.39	1.0	0.1	0.76	1.8	69.3	1.95
heavy	1.75	2.0	4.0	0.2	0.6	0.6	−1.65	0.50	1.0	0.1	0.55	1.8	62.7	1.60
v. heavy	1.75	2.0	4.0	0.2	0.6	0.6	−1.65	0.50	1.0	0.1	0.55	1.8	64.5	1.70

Models: "**MW-A**": MW-A model from Kuijken & Dubinski (1995) with bulge excluded, as a starting point in the parameter search prior to survey; "**fiducial**": fiducial model; "**very conc.**": disc strongly concentrated towards centre; "**concen.**": disc mildly concentrated towards the centre; "**thin**": thin disc; "**hot**": high velocity dispersion of disc; "**3kpc**": 3kpc disc radius; "**5kpc**": 5kpc disc radius; "**6kpc**": 6kpc disc radius; "**6.5kpc**": 6.5kpc disc radius; "**extended**": extended halo; "**halo**": massive halo dominated; "**disc**": massive disc dominated; "**heavy**": heavy initial SMC; "**v. heavy**": very heavy initial SMC;

Parameters: [1] disc mass, [2] disc scale radius, [3] disc truncation radius, [4] disc scale height, [5] disc truncation width, [6] disc central radial velocity dispersion, [7] halo central potential, [8] halo velocity dispersion, [9] halo potential flattening, [10] halo core smoothing parameter, $c = R_{\rm c}^2/R_{\rm K}^2$, and [11] characteristic halo radius.

Table 3.4: GalactICs output parameters for all SMC models used in parameter survey, demonstrating those variables we attempt to control for.

Model	Disc						Halo				Total
	$M_{\rm d,o}$	$R_{\rm d,95}$	$\frac{R_{\rm d}}{R_{\rm d,95}}$	$z_{\rm d}$	$Q_{0.5}$	$\sigma_{\rm R,0}$	$M_{\rm h}$	$R_{\rm h,95}$	$\frac{R_{\rm K}}{R_{\rm h,95}}$	σ_0	M
	$(10^9\,{\rm M}_\odot)$	(kpc)		(kpc)		$({\rm km\,s^{-1}})$	$(10^9\,{\rm M}_\odot)$	(kpc)		$({\rm km\,s^{-1}})$	$(10^9\,{\rm M}_\odot)$
	(1)	(2)	(3)	(4)	(5)	(6)	(7)	(8)	(9)	(10)	(11)
MW-A	0.42	4.4	0.25	0.11	2.79	20.1	2.58	5.4	0.13	37.6	3.00
fiducial	1.49	7.0	0.50	0.35	1.08	32.1	1.51	6.8	0.13	25.9	3.00
very conc.	1.49	5.6	0.25	0.35	1.51	24.9	1.51	7.0	0.13	34.4	3.00
concen.	1.51	6.7	0.37	0.35	1.09	23.7	1.49	6.8	0.13	27.0	3.00
thin	1.50	7.0	0.50	0.17	1.09	33.2	1.50	6.8	0.12	25.2	3.00
hot	1.49	7.0	0.50	0.35	1.81	47.3	1.51	6.8	0.13	25.9	3.00
3kpc	1.49	3.0	0.50	0.15	1.88	47.4	1.51	2.9	0.13	39.5	3.00
5kpc	1.49	5.0	0.50	0.25	1.15	37.9	1.51	4.8	0.13	31.7	3.00
6kpc	1.49	6.0	0.50	0.30	1.03	34.5	1.51	5.8	0.13	27.9	3.00
6.5kpc	1.49	6.5	0.50	0.33	1.03	33.0	1.51	6.3	0.13	26.8	3.00
extended	1.48	7.0	0.50	0.35	1.09	30.8	1.52	8.2	0.14	25.9	3.00
halo	1.11	7.0	0.50	0.35	1.21	28.1	1.89	7.0	0.13	26.5	3.00
disc	2.01	7.0	0.50	0.35	1.00	34.4	0.99	6.8	0.15	26.5	3.00
heavy	1.68	7.0	0.50	0.35	1.08	34.2	1.72	6.8	0.13	27.5	3.40
v. heavy	1.78	7.0	0.50	0.35	1.08	35.2	1.82	6.8	0.13	28.3	3.60

Parameters: [1] disc mass after truncation at $R_{\rm t}$, [2] disc extent, as measured by the radius containing 95% of disc particles, [3] concentration of disc, measured by the scale radius relative to the disc extent, [4] scale height of disc, [5] Toomre Q at the disc half mass radius, [6] radial velocity dispersion of the disc at the centre, [7] halo mass, [8] halo radial extent, as measured by the radius containing 95% of halo particles, [9] concentration of halo, measured by the king-profile radius relative to the halo extent, that we keep approximately constant since its consequences are not readily observable, [10] velocity dispersion of the halo at the centre, and [11] total mass of the SMC.

(with width $\delta R_{\rm t}$) mimicking the tidal radius of the disc, $R_{\rm d}$ is the scale length of the disc, and $M_{\rm d}$ sets the mass of the disc prior to truncation at $R_{\rm t}$ assuming the vertical structure does not deviate far from $\mathrm{sech}^2(z/z_{\rm d})$. The radial velocity distribution of the disc is constructed independent of the density, and is roughly Gaussian with dispersion $\sim \sigma_{\rm R,0}$ at the mid-plane. These input parameters for the disc are summarised in Table 3.3 for our chosen models.

Parameter Search and Surveys

In a search for a fiducial model of the MS, as well as searching the parameter space affecting the orbits of both MCs in Equations (3.4) and (3.5), we vary a set of parameters characterising the density function of the SMC. Rather than searching the parameter space described by the more abstract dimensionless parameters characterising the DF in GalactICs, the set of parameters we search over are derived from the output of GalactICs. These scaled outputs of GalactICs are detailed in Table 3.4. The disc parameters we vary are the mass $M_{\rm d,o} < M_{\rm d}$, calculated after the disc is truncated and after the potentials are evaluated self consistently, the central radial velocity dispersion $\sigma_{\rm R,0}$, the scale length and scale height $R_{\rm d}$ and $z_{\rm d}$, and the radius of the disc $R_{\rm d,95}$, defined by the radius containing 95 per cent of the disc particles. We also vary the halo quantities of mass $M_{\rm h}$, velocity dispersion σ_0, and radial extent $R_{\rm h,95}$ (defined analogously to $R_{\rm d,95}$). The employment of gravitational softening during simulations relaxes the disc and halo slightly, so these parameters are evaluated after allowing the galaxy model to attain equilibrium in a run in the absence of the MW or LMC potentials (see below for more detail on this equilibrium run).

We adopt an *ad-hoc* algorithm to adjust the GalactICs input parameters until we obtain an output parameter set that approximates our desired parameters for a candidate fiducial model, and then test that model in a simulation in order to see if it produces a MS that resembles the observed MS. We call this phase the parameter search. Starting from the MW-A model detailed in Kuijken & Dubinski (1995), after removing the unwanted bulge component, we adjust the parameters using the fact that the halo tidal radius divided by the core radius $R_{\rm h,t}/R_{\rm c}$ is proportional to $(-\Psi_0/\sigma_0^2)^x$ for some power x, for a large range of potentials (see Figure 2 of Kuijken & Dubinski, 1995). Increasing the depth of the central potential of the halo, $-\Psi_0$, tends to increase $R_{\rm h,t}/R_{\rm c}$. Thus increasing the depth of the potential of

the halo leads to a more massive halo relative to the disc, a higher central density, larger halo tidal radius and smaller King radius of the galaxy, therefore tending to increase the concentration of the halo. The central velocity dispersion of the halo is σ_0, and $v_0 = \sqrt{2}\sigma_0$ is the approximate peak of the halo rotation curve. The higher this velocity, the smaller the tidal radius. The scaling radius of the halo, $R_{\rm a}$, is the radius where the halo rotation curve would reach v_0 if extrapolated from the initial slope. The higher this value, the more massive the halo is relative to the disc, and the larger the halo tidal radius. These parameter dependencies are coupled, and thus the process of finding a suitable initial model is necessarily iterative. After a suitable fiducial model is obtained in the parameter search, we perform a parameter survey to determine how the set of parameters affect the evolution of the MS. In this parameter survey, we adopt the same algorithm to adjust properties of the SMC halo and disc, starting from the fiducial model as a base for each parameter varied.

3.2.2 Equilibrium Run

We verify that the initial conditions generated by GalactICs are in equilibrium before evaluating them in the "simulation run". To do this, we perform stability tests on all initial SMC models, in the absence of any external potential (the "equilibrium run"), to ensure the initial models were indeed relatively stable.

Equilibrium Run – N-body

Adopting the same parameters for our simulated SMC galaxy as in the simulation run, we evaluate a "dummy" orbit of the SMC, such that the mass of the LMC and rotation velocity of the MW in Equations (3.1) and (3.3) are set to zero. This dummy orbit and SMC initial conditions were input into our standard GCD+ code as normal. The model SMC galaxy was found to drift primarily in the z direction when evolved in such a fashion in the $\sim 2\,$Gyr timescales we are interested in. The drift was likely caused by statistical fluctuations in the random velocities chosen for each particle. A minor modification was performed on the GalactICs code documented in Kuijken & Dubinski (1995), to force each particle with a (position, velocity) tuple $(x, y, z, v_{\rm x}, v_{\rm y}, v_{\rm z})$ to have a partner with the (position, velocity) tuple $(-x, -y, -z, -v_{\rm x}, -v_{\rm y}, -v_{\rm z})$, forcing the resultant galaxy to have no net linear momentum, but preserving any rotational momentum. An improved pseudorandom number generator was also substituted in place of the custom random number gen-

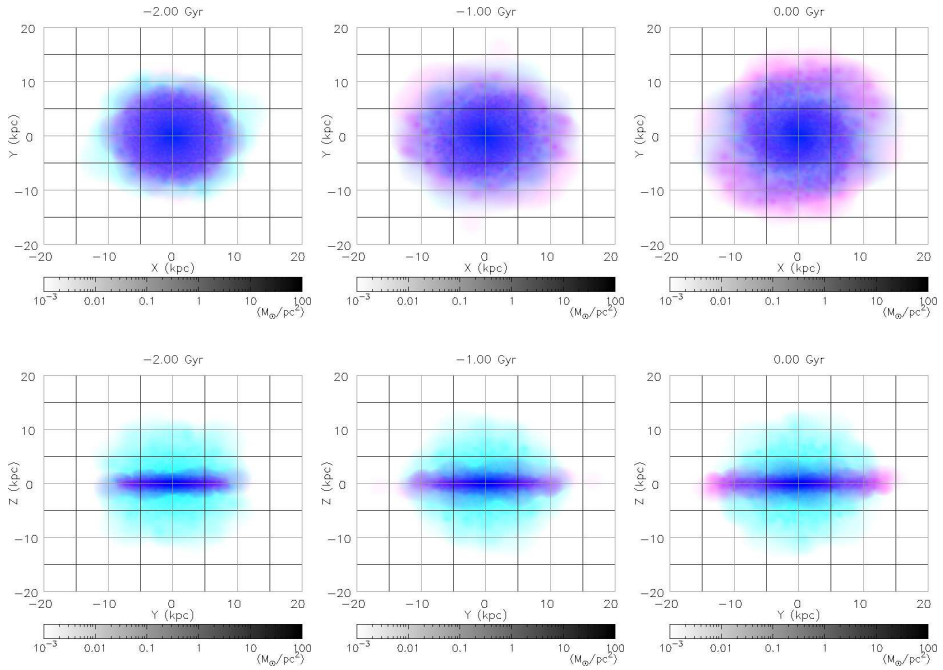

Figure 3.3: Face on (top) and edge on (bottom) views of the surface density of the SMC DM halo (cyan) and SMC disc (magenta; overlapping areas add to give blue), at the start of the equilibrium run at $t = -2\,\mathrm{Gyr}$ (left), at $t = -1\,\mathrm{Gyr}$ (middle), and at $t = 0\,\mathrm{Gyr}$ (right), for the fiducial model.

erator existing in the code. After these modifications, the SMC was found not to drift in either equilibrium or simulation runs. In Figure 3.3, we display the evolution of the disc and halo of our fiducial model over 2 Gyr in the absence of any external gravitational field. We encounter only a minimal degree of artificial disc heating and newly-introduced spiral structure (generally with two symmetric arms), after 2 Gyr. The density (ρ), velocity dispersion (σ), surface density (Σ) and disc rotational velocity (V_{rot}) profiles in Figure 3.4 are unchanged out to two disc scale lengths, $2R_{\mathrm{d}}$, after the same time period.

Equilibrium Run – Smooth Particle Hydrodynamics

When hydrodynamics and star formation are modelled, the initial conditions will not be in equilibrium because we assume that no stars exist in the disc initially, and so a burst of star formation results suddenly heating the disc. Figures 3.5 and 3.6 show the evolution of the gas and stellar discs, as well as the DM halo in the equilibrium stability test without supernovae (SNe) feedback, and with SNe feedback, respectively. It can be seen from Figure 3.5 that the gas disc experiences some heating in an equilibrium run when no SNe feedback is included, and so the

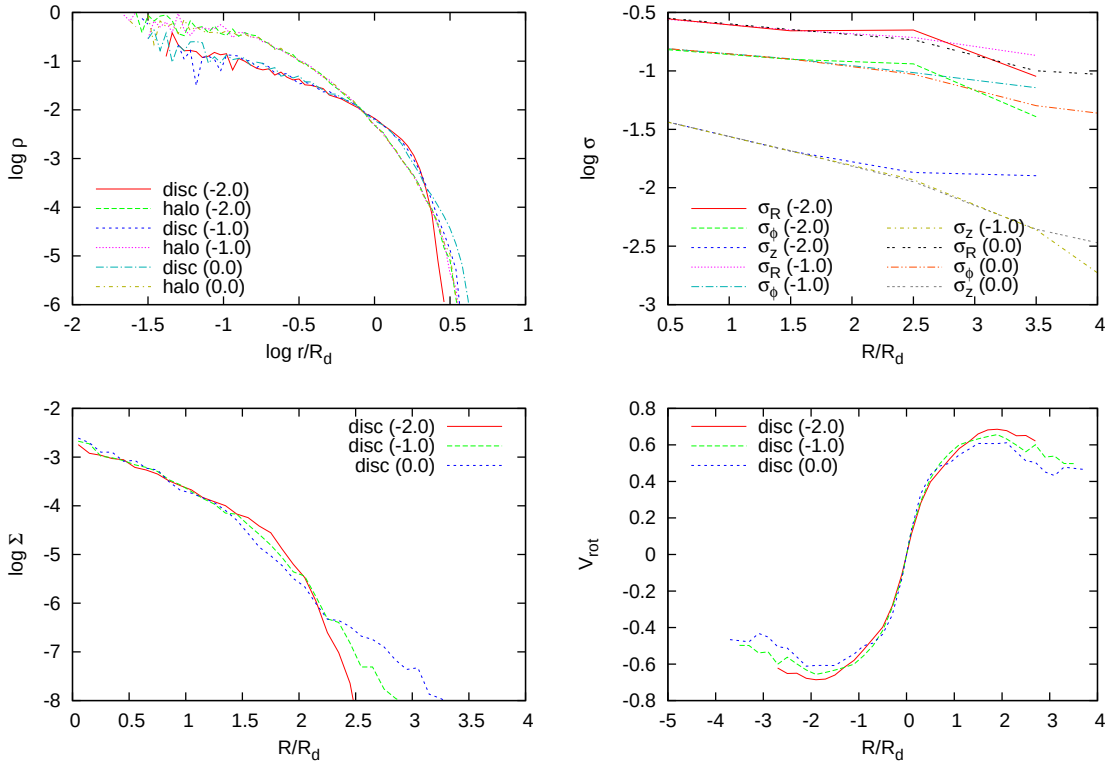

Figure 3.4: Evolution of various distribution profiles at $t = -2\,\mathrm{Gyr}$, $t = -1\,\mathrm{Gyr}$ and $t = 0\,\mathrm{Gyr}$ as labelled in brackets, in the dimensionless units of GalactICs, for the fiducial model. The disc and halo densities (top left), disc and halo velocity dispersions in the R, ϕ (offset by -0.5 dex to avoid overlap) and z (offset by -1 dex) directions (top right), disc surface density (bottom left), and disc rotational velocity (bottom right) are plotted.

disc will be effectively larger than the discs created in the fiducial model without hydrodynamics, during the interaction run. A stellar disc forms, that is stable and 7 kpc across at 2.5 Gyr. If we include SNe feedback, both the gaseous and stellar discs are much less stable.

3.2.3 Interaction Simulations

We adopt an SMC-centric non-inertial (but non-rotating) coordinate system for our interaction simulations, one in which the SMC disc lies on the x–y plane. The orbits of the LMC and MW and the SMC model from Section 3.2.1 are translated and rotated to this coordinate system, and the SMC model is evolved within this new coordinate system under the influence of the now "orbiting" MW and LMC. There are two degrees of freedom for the current inclination angle of the SMC, both

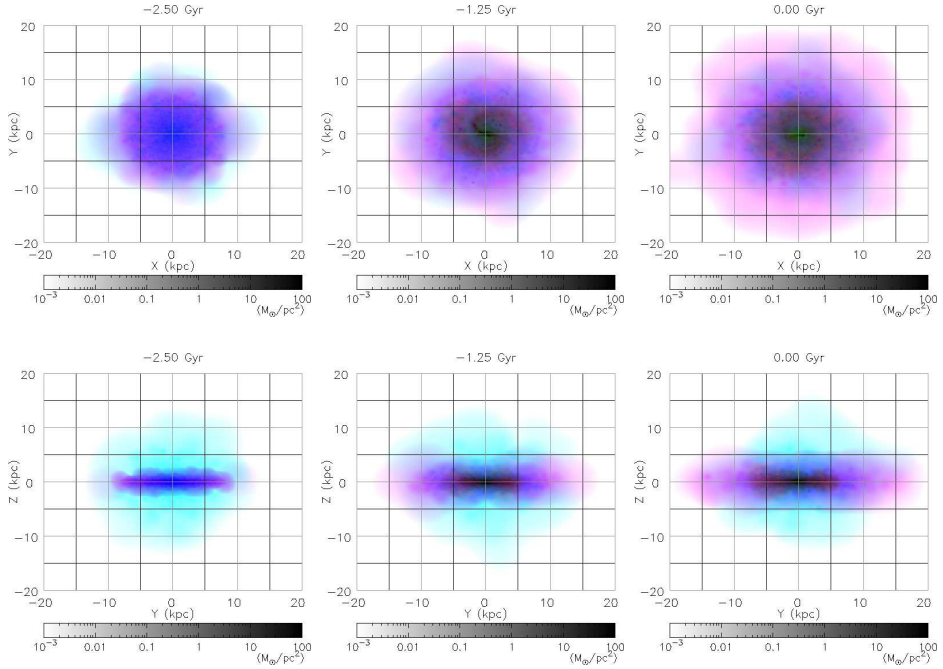

Figure 3.5: Face on (top) and edge on (bottom) views of the of the surface density of the SMC DM halo (cyan) and SMC gas disc (magenta; overlapping areas add to give blue), and SMC stellar disc (yellow; overlapping areas add to give green–black) at the start of the equilibrium run at $t = -2.5\,\mathrm{Gyr}$ (left), at $t = -1.25\,\mathrm{Gyr}$ (middle), and at $t = 0\,\mathrm{Gyr}$ (right), for the fiducial hydrodynamical model with no SNe feedback.

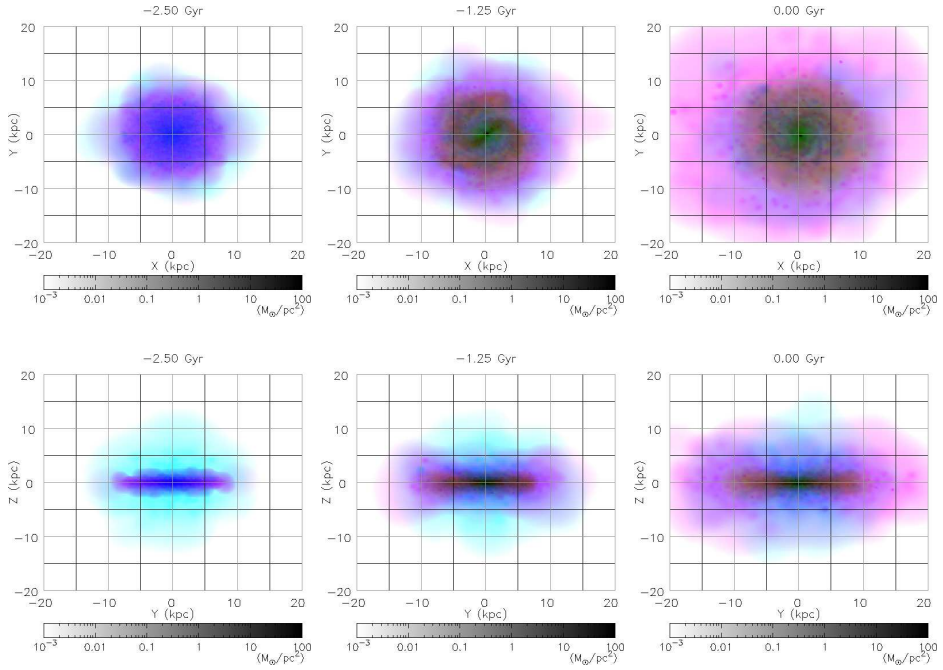

Figure 3.6: As in Figure 3.5, but with SNe feedback.

currently unknown. We define θ and ϕ following fig. 1 of GN96, survey the full range of both, and find that the final features of the simulated MS are sensitive to this angle. We adopt in the fiducial model an angle of $(\theta, \phi) = (45°, 210°)$, as discussed in Section 3.4. This choice leads to a trailing tidal stream with an orientation consistent with the observed MS, and a leading arm with shape qualitatively similar to the observed LAF. This angle is mildly different from that adopted in GN96, $(\theta, \phi) = (45°, 230°)$, but we find that the new value leads to a better match to the HIPASS dataset (which was not available to GN96).

The particles in the SMC are assumed to be collisionless and their dynamical evolution calculated with GCD+. The acceleration applied to the i-th particle is described (GN96) by

$$\begin{aligned} \ddot{\mathbf{r}}_i &= -G \sum_{j \neq i}^{n} \frac{m_j (\mathbf{r}_i - \mathbf{r}_j)}{\left(|\mathbf{r}_i - \mathbf{r}_j|^2 + \epsilon^2\right)^{3/2}} \\ &\quad + \mathbf{F}_{\rm MW}\left(\mathbf{r}_i - \mathbf{r}_{\rm MW}\right) + \mathbf{F}_{\rm LMC}\left(\mathbf{r}_i - \mathbf{r}_{\rm LMC}\right) \\ &\quad - \mathbf{F}_{\rm MW}\left(-\mathbf{r}_{\rm MW}\right) - \mathbf{F}_{\rm LMC}\left(-\mathbf{r}_{\rm LMC}\right), \end{aligned} \tag{3.10}$$

where ϵ is the softening length (see Section 2.2.1) and m_j is the mass of the j-th particle. The position of $\mathbf{r}$ is measured in the SMC-centric coordinate frame. The first term is the self-gravity of the SMC particles; the second and third terms are the forces on the particle resulting from the Galaxy and LMC, and can be derived from the respective potentials in Equations (3.1) and (3.3):

$$\mathbf{F}_{\rm MW}(\mathbf{r}) = -\frac{V_{\rm c}^2}{|\mathbf{r}|^2}\mathbf{r}, \tag{3.11}$$

$$\mathbf{F}_{\rm LMC}(\mathbf{r}) = -\frac{G M_{\rm L} \mathbf{r}}{\left(\mathbf{r}^2 + K_{\rm L}^2\right)^{3/2}}. \tag{3.12}$$

The final two terms arise from needing to correct for the integration of the equations of motion in a non-inertial reference frame centred on the SMC. All but the first term of Equation (3.10) are set to zero during the equilibrium run tests by the virtue of $M_{\rm LMC} = 0$ and $V_{\rm c} = 0$.

3.3 Fiducial Model

In this section, we demonstrate our fiducial model, the basic parameters for which are listed in Table 3.4 and below. Since we are primarily interested in the formation

of the MS and LAF, which we assume are both stripped H I gas components from the SMC disc, our analysis focuses on the particles which were initially within the original SMC disc. In what follows, our simulation products are compared closely with the empirical HIPASS dataset.

3.3.1 Initial Conditions for the Fiducial Model

The disc possesses an exponential profile with scale radius $R_{\rm d} = 3.5\,{\rm kpc}$, smoothly truncated beyond $R_{\rm t} = 7\,{\rm kpc}$ (with 95 per cent of both the disc and halo masses being within $r_{\rm d,95} \sim r_{\rm h,95} \sim 7\,{\rm kpc}$), to give a disc with total radial extent (where the face-on surface density of the disc reaches $1\,{\rm M}_\odot\,{\rm pc}^{-2}$) of 7.5 kpc (compared to the halo with radial extent of $\sim 14\,{\rm kpc}$). The rotation curve peaks at $\sim 2\,{\rm kpc}$ with a velocity of $\sim 45\,{\rm km\,s}^{-1}$, and turns over to become approximately constant, giving a total SMC mass of $3 \times 10^9\,{\rm M}_\odot$, with the disc mass being $1.5 \times 10^9\,{\rm M}_\odot$. The central velocity dispersion of the disc was chosen to be near the current H I velocity dispersion of the observed SMC (Figures 3.12 and 3.13), and the DM halo velocity dispersion of $26\,{\rm km\,s}^{-1}$ is similar to the value of $\sim 25\,{\rm km\,s}^{-1}$ obtained from observations of the stellar halo carbon stars and planetary nebulae (Dopita et al., 1985; Hardy et al., 1989; Hatzidimitriou et al., 1997). The Toomre Q-parameter at the disc half-mass radius is $Q = 1.08$.

Our fiducial SMC model assumes a somewhat larger scale length and total extent for the SMC disc of 3.5 kpc and 7 kpc respectively, when compared with earlier studies (GSF94; GN96; YN03). We should stress that one cannot simply take as initial conditions, the observed parameters of the SMC at the *present day*, since the SMC has obviously been significantly disturbed by interactions with the MW and LMC; we instead use initial parameters consistent with other relatively isolated dwarf disc galaxies (and integrate forward to ensure the final characteristics is consistent with that observed today). Dwarfs with H I mass $1.3 - 2.0 \times 10^9\,{\rm M}_\odot$ (comparable to the original SMC) have H I disc scale lengths ranging from 1.6 to 4.4 kpc, and smaller optical (i.e., stellar) scale lengths of 0.9 to 2.7 kpc (Swaters et al., 2002). These same galaxies have H I discs whose face-on corrected H I density drops to $1\,{\rm M}_\odot\,{\rm pc}^{-2}$ at a radius between 10 to 12 kpc. It is assumed in our models that the disc is comprised of both gas and star particles. Here, we mainly focus on N-body simulations, however in a hydrodynamical simulation, the smaller optical disc scale length is naturally reproduced by implementing the Schmidt law of star formation (Sec-

tion 2.2.4). Star formation is quenched in regions where the gas density falls below a density threshold $\rho_{\rm crit}$. A column density threshold for the SMC has been found to be $2.5 \times 10^{21}\,{\rm cm}^{-2}$ (Kennicutt et al., 1995), equivalent to a surface density threshold of $18.0\,{\rm M}_\odot\,{\rm pc}^{-2}$ and within a factor of a few of undisturbed systems (YN03). It thus seems reasonable that with our extended SMC model, the surface density would be even smaller than past models, and thus our stellar disc will be reduced in size.

The reasons for the larger truncation radius compared to previous work are twofold. First, we suggest the tidal radius of the SMC disc is larger than the 5 kpc proposed by GN96. Several Gyrs ago, the MW was likely to have been slightly less massive (secular halo growth), the SMC slightly more massive (less tidal disruption), and the perigalactic distance of the SMC was larger. In the estimated orbit of the SMC, at a lookback time of 2.5 Gyr (Figure 3.2), the perigalactic distance $r_{\rm p}$ was 60 kpc, and the apogalactic distance $r_{\rm a}$ was 120 kpc. However, the MW mass enclosed within the larger SMC orbit has then increased. The tidal radius of the SMC is (Faber & Lin, 1983)

$$r_{\rm t} = r_{\rm p} \left[\frac{M_{\rm S}}{(3+e) M_{\rm G}(r_{\rm p})} \right]^{1/3}, \tag{3.13}$$

where the eccentricity $e = (1 - r_{\rm p}^2/r_{\rm a}^2)^{0.5}$, and thus $r_{\rm t} = 6.3\,{\rm kpc}$ when $r_{\rm p} = 60\,{\rm kpc}$. We also suggest that it is not unreasonable that the disc was initially somewhat larger than the tidal radius when the SMC started to experience tidal stripping.

We use 200,000 disc and 200,000 halo particles to describe the SMC in the fiducial model. This corresponds to a resolution $\sim$ 30 times greater than that employed by GN96, G99 and YN03. Such high-resolution allows us to examine features of the MS, LAF, and SMC in a manner not previously possible, since smaller fractional differences in particle density become statistically significant. We adopt approximately equal masses for the disc and halo particles of $7.4 \times 10^3\,{\rm M}_\odot$ and $7.6 \times 10^3\,{\rm M}_\odot$, and softening lengths $\epsilon_d \sim \epsilon_h \sim 65\,{\rm pc}$, respectively. The high mass resolution requires a short timestep interval of $\sim 25,000$ years.

3.3.2 Evolution

In Figure 3.7, we present a series of snapshots in the Galactocentric coordinate system, with the orbit of the MCs overlayed. Consistent with earlier models (e.g. GN96; YN03), when the SMC experienced a close encounter with the MW and

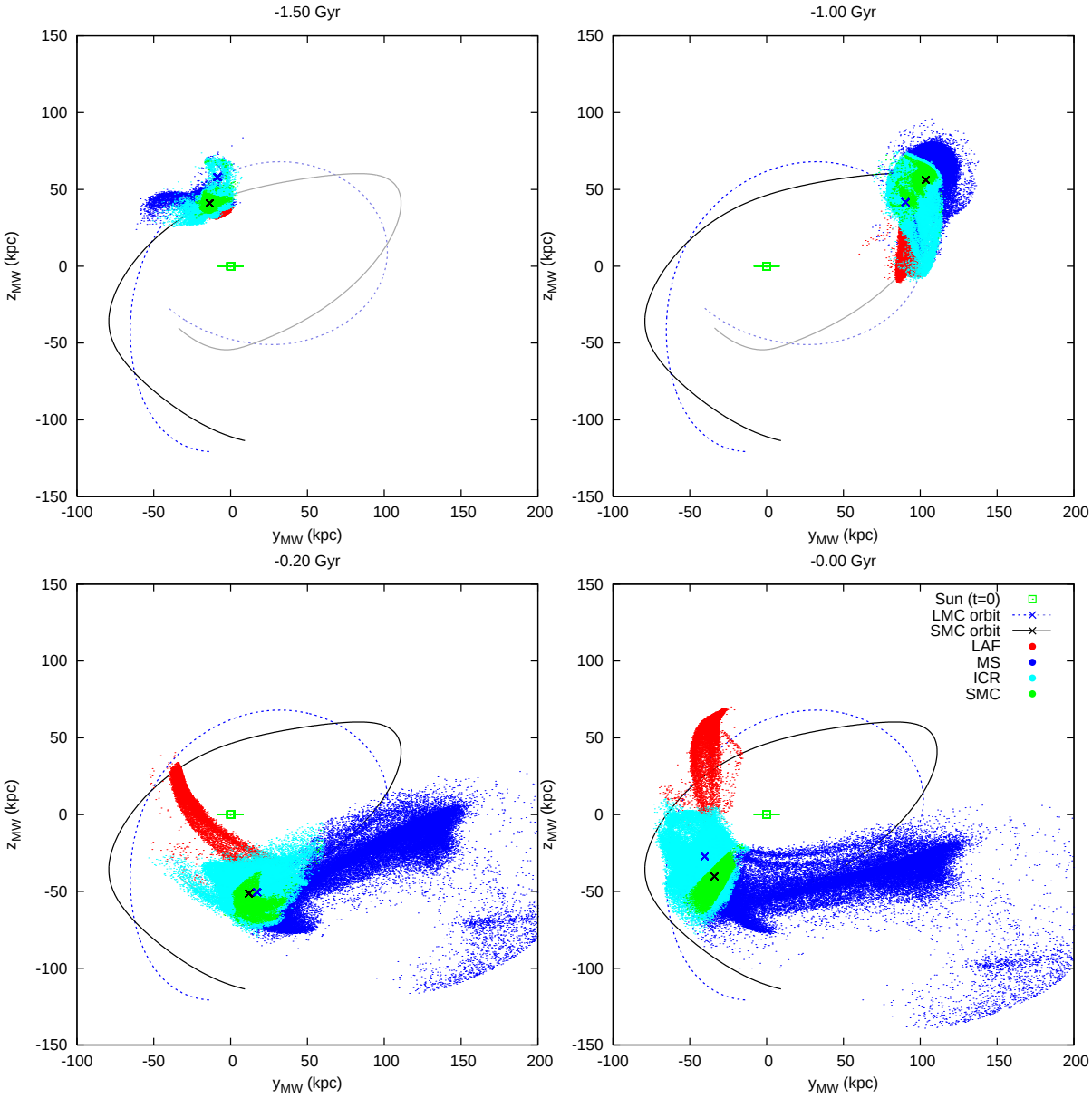

Figure 3.7: The configuration of the "gas" disc particles of the fiducial N-body simulation in the Galactocentric coordinate system at different timesteps. Different colour dots represent the particles which end up in different components at $T = 0$ as shown in the bottom-right plot. See the text and Figure 3.8 for the adopted spatial regions used to delineate the MS, LAF, ICR, and SMC in this final timestep.

the LMC about 1.5 Gyr ago, the edge of the disc of the SMC began to be drawn out, which formed the tidal features that later became the LAF and MS. By $T = -1.0$ Gyr, at the subsequent apo-Galacticon, the LAF becomes more prominent, whilst the MS was still under development. By $T = -0.3$ Gyr, much of the initially stripped material in the leading tidal arm had been pulled back into the ICR, and the material still in the LAF was brought within 3 kpc of the solar circle. By this time, the MS and LAF morphology resemble that seen today. The next encounter with the MW and LMC at $T = -0.2$ Gyr caused little obvious consequence to either the MS or LAF. It did, however, cause the dispersion of much of the material that had been within the SMC. Much of this material either ended up in the ICR (although most of the ICR material was already in an ICR structure before this event), or contributed to the large spread in radial extent of the SMC. At the current time, the ICR extends radially from ~ 30 to ~ 80 kpc, and the SMC from ~ 45 to ~ 60 kpc.

We also ran the simulation "forward" in time to $T = +0.25$ Gyr and found that the ICR undergoes mass loss with material being dragged out into two tidal tails, separated radially and kinematically from the main MS and LAF features. This is consistent with what is expected by Brüns et al. (2005). By $T = +0.25$ Gyr, the material in the ICR has been dragged 55 kpc towards the MS in the plane of the sky, giving an angular separation of 35° between the SMC and tip of the ICR.

3.3.3 H I Column Density Distribution

In this section, we compare the present-day H I column density distribution between the empirical HIPASS dataset and our simulation results. We combine the carefully flagged data cube of P98 with other HIPASS (Barnes et al., 2001) cubes surrounding the LAF, with appropriate velocity cuts to exclude Galactic H I emission particularly as the LAF crosses the disc. Figure 3.8 displays the H I column density map on a Zenith Equal Area (ZEA) projection. Here, we define by eye, the regions corresponding to the MS, LAF, ICR, and SMC as shown in the bottom panel of Figure 3.8. We converted the observed 21cm flux to H I column density, after Barnes et al. (2001), assuming optically thin H I emission (an assumption that is expected to break down partially in the higher column density regions of the SMC and ICR). To construct H I column density maps from the simulation results, we assume that the disc particles in the SMC are purely gaseous, and the H I mass fraction is 0.76 (see Section 2.3.4). The column densities within the SMC and ICR

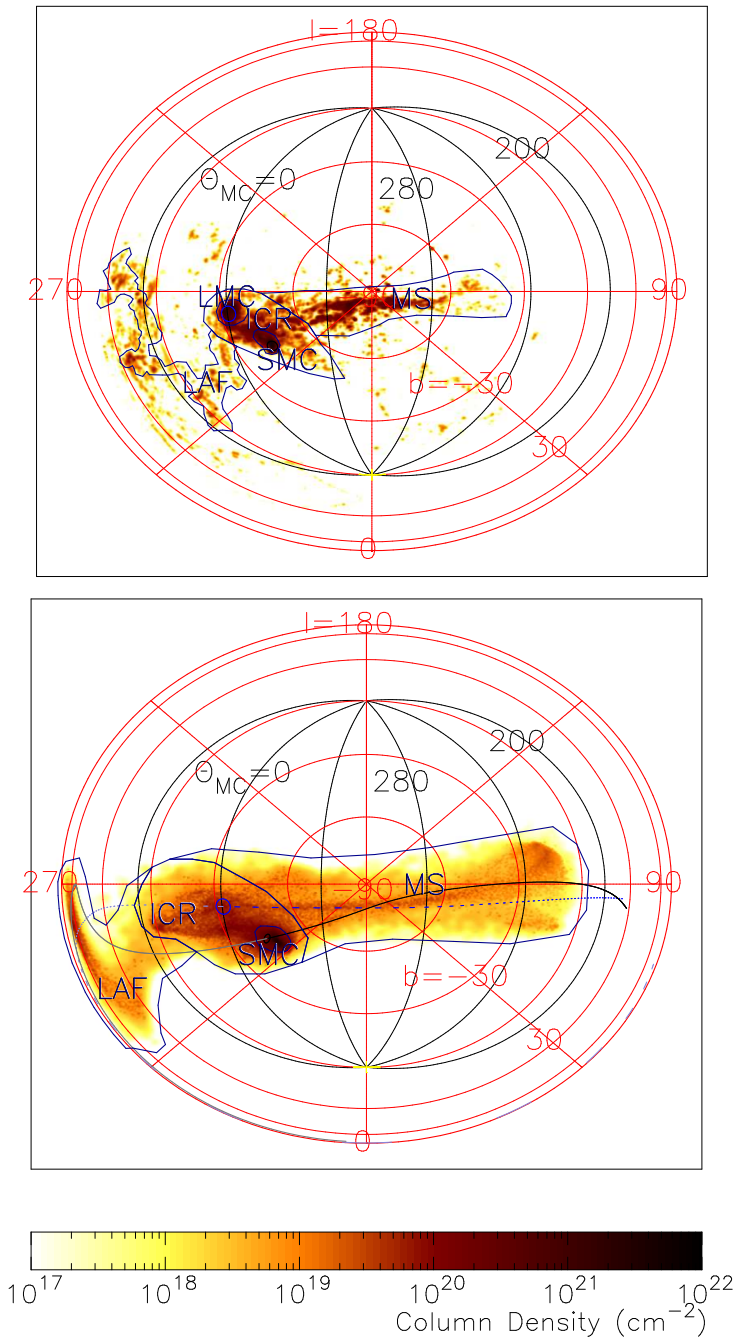

Figure 3.8: H I column density map (i.e., zeroth moment map) of the empirical data (top) and our fiducial model (bottom). A full sky Zenith Equal Area projection centred on the South Galactic Pole is applied, to preserve flux. We define by eye, the regions delineated by blue lines which are used to quantify the masses in Section 3.3.3. In the bottom panel, the enclosed regions with labels of MS, LAF, ICR, and SMC are also used to tag particles in Figure 3.7. The current positions of the SMC and LMC are represented by black and blue ellipses, and in the bottom panel, the past and future 1 Gyr histories of the SMC and LMC orbit are denoted by black solid and blue dashed lines, respectively (the future 1 Gyr is shaded in a lighter colour). Lines of constant Magellanic Longitude are drawn in black, with the LMC lying on the $\theta_{\rm MC} = 0°$ meridian.

region will be somewhat overestimated, as we neglect currently any associated stellar and ionised components of the disc. On the one hand, Figure 3.9 demonstrates that most particles in the MS and the LAF at $T = 0$ originate in the outer edge of the initial SMC disc, where there was likely a lack of stars due to the surface density dropping below a threshold, $\rho_{\rm crit}$, required for star formation (Section 3.3.1). Similarly, stars are not expected to form *in-situ* in the MS or LAF because of the low surface density, and to date, searches for a putative stellar component to the MS have proven unsuccessful (e.g. Philip, 1976b,a; Recillas-Cruz, 1982; Brueck & Hawkins, 1983). On the other hand, Lehner et al. (2008) show that the ICR is quite ionised, with only $\sim 20\%$ of the gas being H I. The H I fraction of 0.76 thus remains an upper limit, and our predictions should be considered as upper limits. For these reasons the comparisons between the simulation and the HIPASS data focus mainly upon the properties of the MS and LAF.

Figure 3.8 shows that our fiducial model reproduces the gross features of the observed MS, and the LAF appears as a consequence of tidal interactions. This supports previous studies, such as GN96 and YN03, which suggested that the MS and LAF features originate from gas stripped from the SMC disc by the tidal interaction with the LMC and MW.

The full extent of the LAF above the Galactic Plane remains a matter of ongoing research (e.g. Wakker, 2001; Brüns et al., 2005). The top panel of Figure 3.10, which is a new representation of the HIPASS dataset that was not available to P98, demonstrates that the LAF certainly extends above the Galactic plane to latitude $b \sim 30^\circ$. The metallicity of gas in this region (Lu et al., 1998; Gibson et al., 2000) and the association with nearby High Velocity Clouds (HVCs) at the required distance (Ben Bekhti et al., 2006) lend evidence to its SMC origin, supporting the tidal disruption scenario for the MS (and LAF). Furthermore, the observed H I cloud distribution seems to show a "kink" near $(l, b) = (310^\circ, 0^\circ)$, where two further components of the LAF are seen north of the Galactic plane (labelled LA II and III in Brüns et al., 2005). Although the exact position of the kink is inconsistent with the empirical data, our simulation does naturally predict its existence.

Figure 3.11 shows a "moment map" (see Equations 2.54 and 2.69) of the heliocentric distance of the simulated MS and LAF against the Magellanic longitude, $\theta_{\rm MC}$ (as defined in Wakker, 2001; lines of constant $\theta_{\rm MC}$ are shown in Figure 3.8, and the Magellanic coordinate system is the basis of Figure 3.10). The Galactocentric distance to the LAF is $20 - 80$ kpc, not inconsistent with the deduced Galactocentric

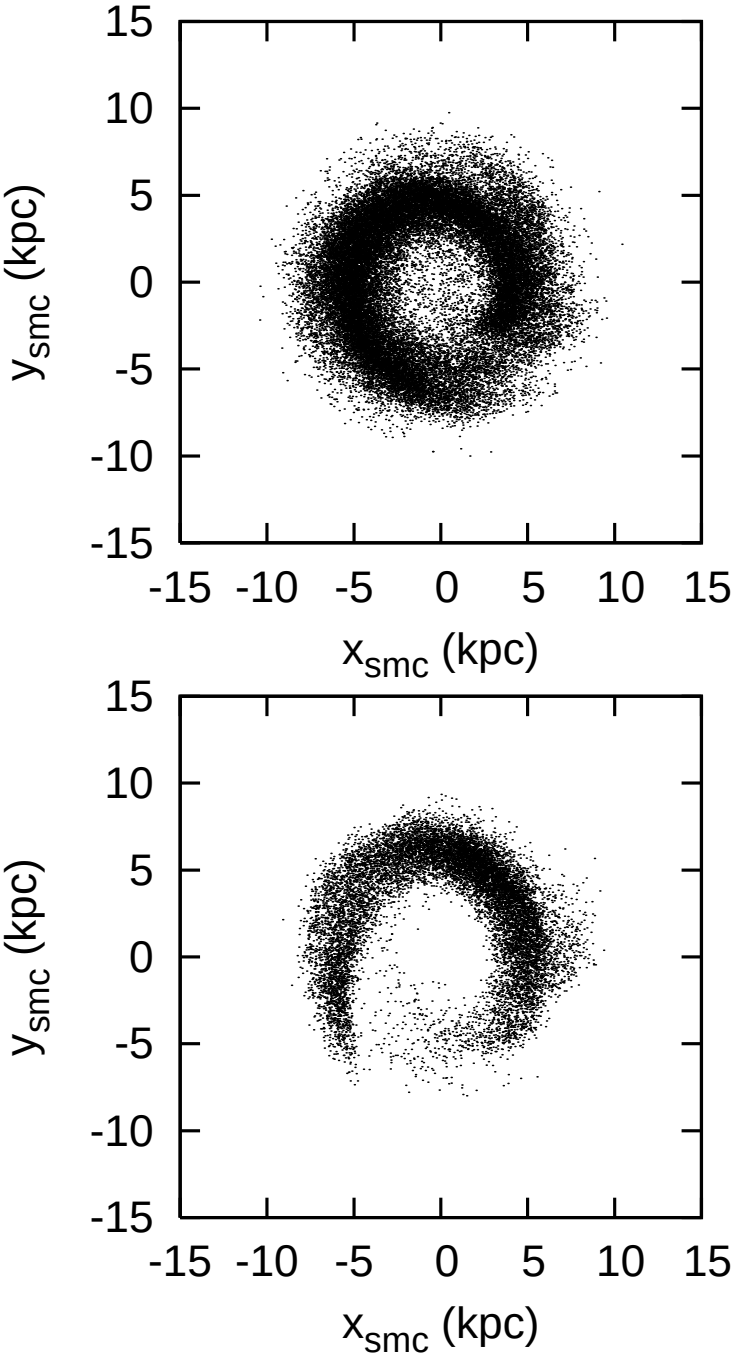

Figure 3.9: The initial distribution of the "gas" disc particles of the fiducial N-body simulation which end up in the MS (top) and LAF (bottom) at $T = 0$ in the face-on view of the initial ($T = -2.5\,\mathrm{Gyr}$) SMC disc. For the criteria used to define the MS and LAF particles, see Figure 3.8.

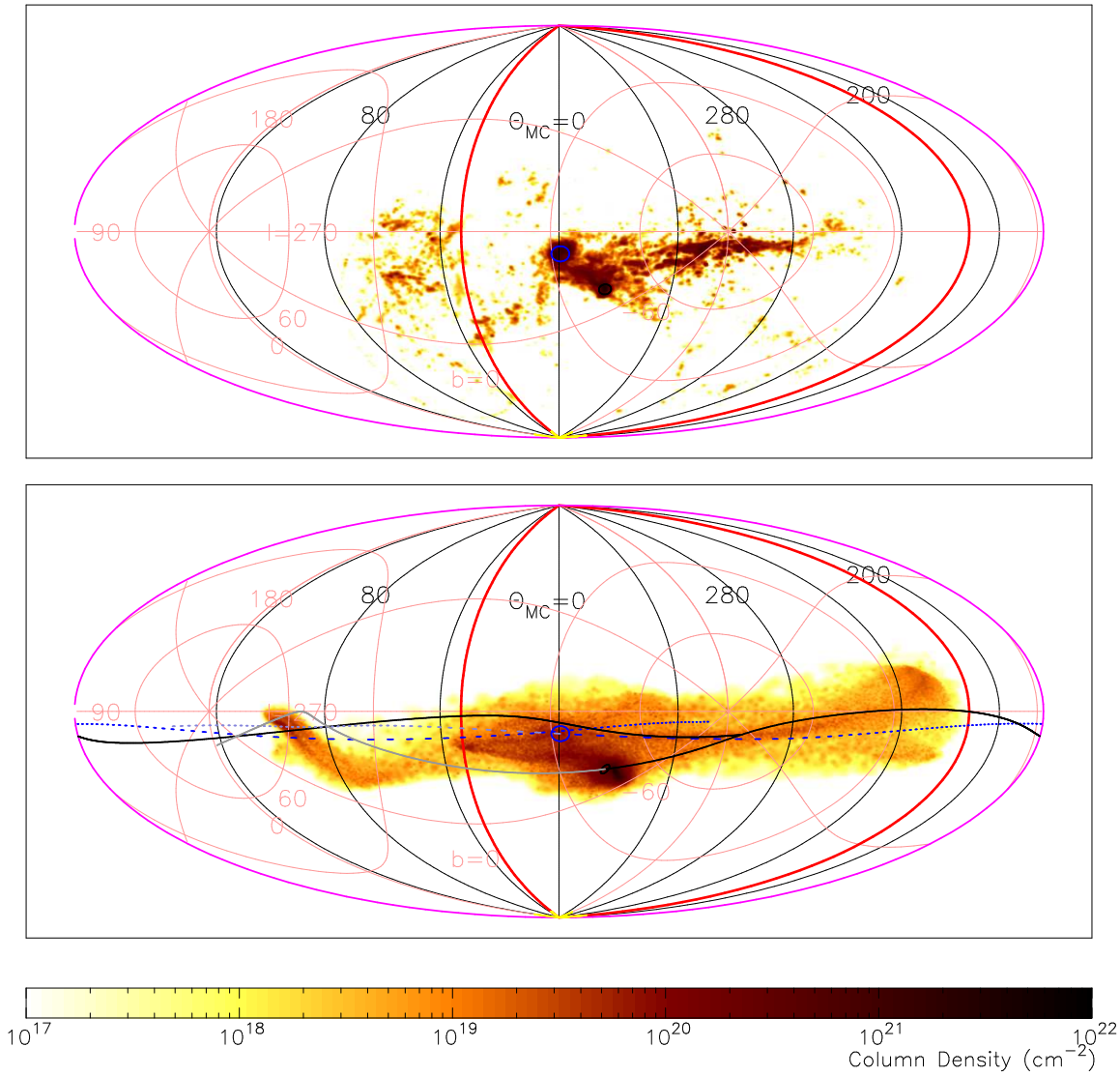

Figure 3.10: H I column density map of the HIPASS dataset (top) and fiducial model (bottom) with a full sky equal area Hammer-Aitoff (AIT) projection centred on the LMC. The coordinate system used here is that of the Magellanic coordinate system, where the MS lies close to the equator (see also Wakker, 2001). This gives a relatively undistorted view of the LAF. The future orbits of the MCs are denoted by a lighter shading, demonstrating the similarity between the orbit of both MCs and the orbit of the LAF. The underlying Galactic coordinates are also displayed in a lighter shading, with the thick red line denoting the Galactic equator.

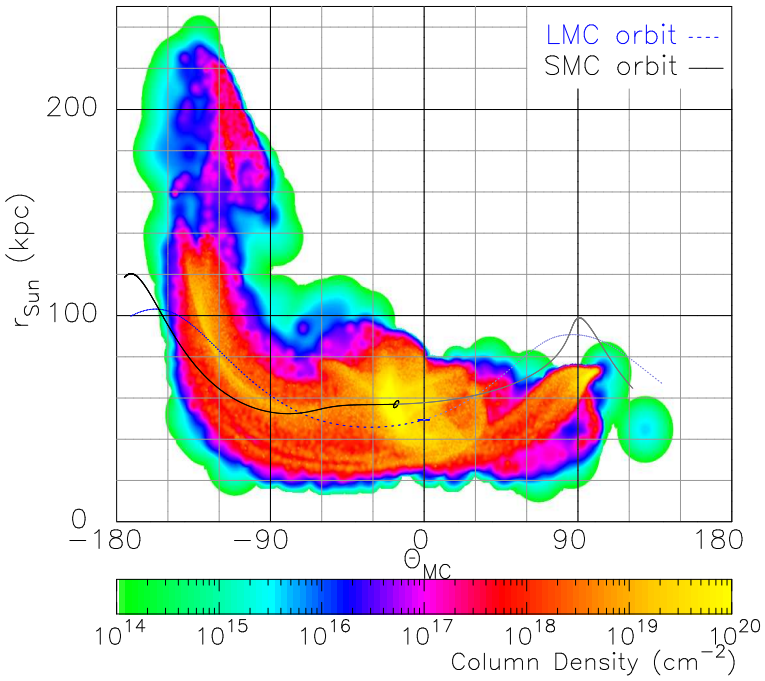

Figure 3.11: The heliocentric distance, as a function of the Magellanic longitude, derived from our fiducial model. The black solid and blue dashed lines show the past and future 1 Gyr histories (the future 1 Gyr is shaded a lighter colour) of distance and Magellanic longitude for the SMC and LMC, respectively.

distance to one LAF HVC of ~ 17 kpc (McClure-Griffiths et al., 2008).

The tail of the observed MS shows spatial bifurcation near $(l, b) = (300°, -70°)$ and $(l, b) = (80°, -55°)$ in Figure 3.8, with the two components forming an apparent twisting double helix-like structure (Putman et al., 2003b). This bifurcation is not apparent in previous studies such as GN96 and YN03; higher resolution simulations enable us to study such subtle features. Since this might be further evidence of the tidal interaction between the LMC and SMC, we return to this issue later.

An advantage of the present work is that the H I data available to constrain the models are significantly improved beyond that of GN96 or YN03. As in those previous studies, while the gross features of the observed MS and LAF are reproduced by our fiducial model, there remain subtle discrepancies between simulations and data. The simulated MS is both broader and more extended than that accounted for in the past (and hence the mean column density is somewhat lower than that encountered in the HIPASS dataset). However Braun & Thilker (2004) shows that the MS may extend as far north as $b = -20°$, and Lockman (2003) notes that HVC Complex H

is of similar internal structure to the MS. The position and kinematics of Complex H ($-15^\circ < b < 15^\circ$, $110^\circ < l < 155^\circ$, and $-220\,\mathrm{km\,s^{-1}} < v_{\mathrm{LSR}} < -80\,\mathrm{km\,s^{-1}}$; Wakker & van Woerden, 1991; Wakker et al., 2003), and that of HVC Complex G ($-20^\circ < b < 0^\circ$, $75^\circ < l < 120^\circ$, and $-200\,\mathrm{km\,s^{-1}} < v_{\mathrm{LSR}} < -80\,\mathrm{km\,s^{-1}}$), are not too dissimilar to the tip of the modelled stream, and if they are indeed related to the MS, then this presents the possibility that the modelling of the stream's extent is correct, despite previous evidence. Gibson et al. (2000) also note that MS appears to be responsible for absorption lines seen against background quasars Mrk 335 and Mrk 1501, more than 20° away from the MS, demonstrating that the MS may be a lot wider than previously thought. With the uncertainty in extent of the MS, the derived H I gas mass (assuming a heliocentric distance of 57 kpc) from HIPASS is still within 50 per cent of that of our simulated fiducial model ($3.5 \times 10^8\,\mathrm{M_\odot}$ and $2.4 \times 10^8\,\mathrm{M_\odot}$, respectively). Figure 3.11 demonstrates that the distance to the simulated MS is not constant, instead increasing across its length. Hence negating the distance ambiguity by obtaining a total flux gives us a fairer comparison than a total mass. Doing so results in an observed MS total H I flux of $4.8 \times 10^5\,\mathrm{Jy\ km\,s^{-1}}$, while the fiducial simulated MS has a total H I flux of $2.3 \times 10^5\,\mathrm{Jy\ km\,s^{-1}}$, still within a factor of ~ 2 of the HIPASS data.

Conversely, the simulated LAF has a predicted H I mass and associated flux ($7.3 \times 10^7\,\mathrm{M_\odot}$ and $7.9 \times 10^4\,\mathrm{Jy\ km\,s^{-1}}$, respectively) both factors of ~ 2 greater than that inferred from the HIPASS dataset ($3.5 \times 10^7\,\mathrm{M_\odot}$ and $4.6 \times 10^4\,\mathrm{Jy\ km\,s^{-1}}$, respectively)[2]. One clear difference between observation and simulation is that of the geometry of the LAF, in particular that of the projected deflection angle between the LAF and a Great Circle aligned with the MS proper (Figure 3.10). In addition, the simulated LAF extends above the Galactic Plane beyond that unambiguously observed. However, note that the more extended "EP" populations of HVCs of Wakker & van Woerden (1991), and other scattered clouds are contiguous in (l, b, v_{LSR}) space with the LAF, and may extend the LAF as far as 60° above the plane (Wakker, 2001), consistent with the tip of the modelled LAF. We will discuss possible solutions to these apparent problems in Section 3.6.

[2]We have defined the LAF and MS regions differently between the empirical and simulated datasets in Figure 3.8, to account for the geometrical differences, such as angle, width, and length, between the two.

3.3.4 H I Kinematics

Figures 3.12 and 3.13 shows the first and second moment maps for both our fiducial simulation and that derived from the HIPASS dataset. In order to remove the large velocity gradient along the MS (which acts to obscure fine kinematical details within the maps, and the differences between the observations and simulations), the first moment map is shown as the distribution of the velocity of $v_{\rm GSR} - v_{\rm MS,avg}$, where $v_{\rm MS,avg}$ is the mean trend of velocity across the observed MS and LAF that is subtracted from both observed and simulated maps equally, and is defined in terms of the first two harmonics, $v_{\rm MS,avg} = 86\sin(\theta_{\rm MC} + 2.5^\circ) - 92\sin(2(\theta_{\rm MC} - 26.3^\circ))$ in the GSR. The second moment map is the distribution of the velocity dispersion of H I gas.

In the first moment map, the observed velocity trend along our simulated MS is shown to be globally consistent with that of the empirical data. Figure 3.14 displays a "moment map" of $v_{\rm LSR}$ against the Magellanic longitude, $\theta_{\rm MC}$ (see Equations 2.54 and 2.67), and demonstrates perhaps more clearly that the mean velocity of the simulated MS is consistent with that observed. In contrast, the line-of-sight velocity of the simulated LAF is significantly larger than that observed, although it does follow the general trend of decreasing velocity at $\theta_{\rm MC} \gtrsim 0$.

The second moment maps seen in Figure 3.13 indicate that the velocity dispersion of the simulated LAF is roughly consistent with that observed, however the velocity dispersion of the simulated MS is somewhat greater than that inferred from the HIPASS dataset. This might be due to the neglect of gas dissipation via radiative cooling in the current suite of simulations.

We end by drawing attention to the evidence of a bifurcation in $v_{\rm LSR}$ (Figure 3.14) within the MS and LAF. The next section discusses this bifurcation in more detail.

3.3.5 Spatial and Velocity Bifurcation

Our fiducial model shows a bifurcation in the MS, as seen in the ZEA spatial distribution of the H I column density of Figure 3.8. Within the simulation, this bifurcation occurs both radially and tangentially. Figure 3.8 displays the tangential bifurcation, and shows that there are two stream components that appear to follow a twisting topology governed by the orbits of the MCs—both the orbits and the bifurcation seem to cross at $(l, b) \sim (45^\circ, -80^\circ)$. Radially, the head of the Stream, just behind the MCs, has two components (Figures 3.7 and 3.11). Also apparent in Figures 3.11

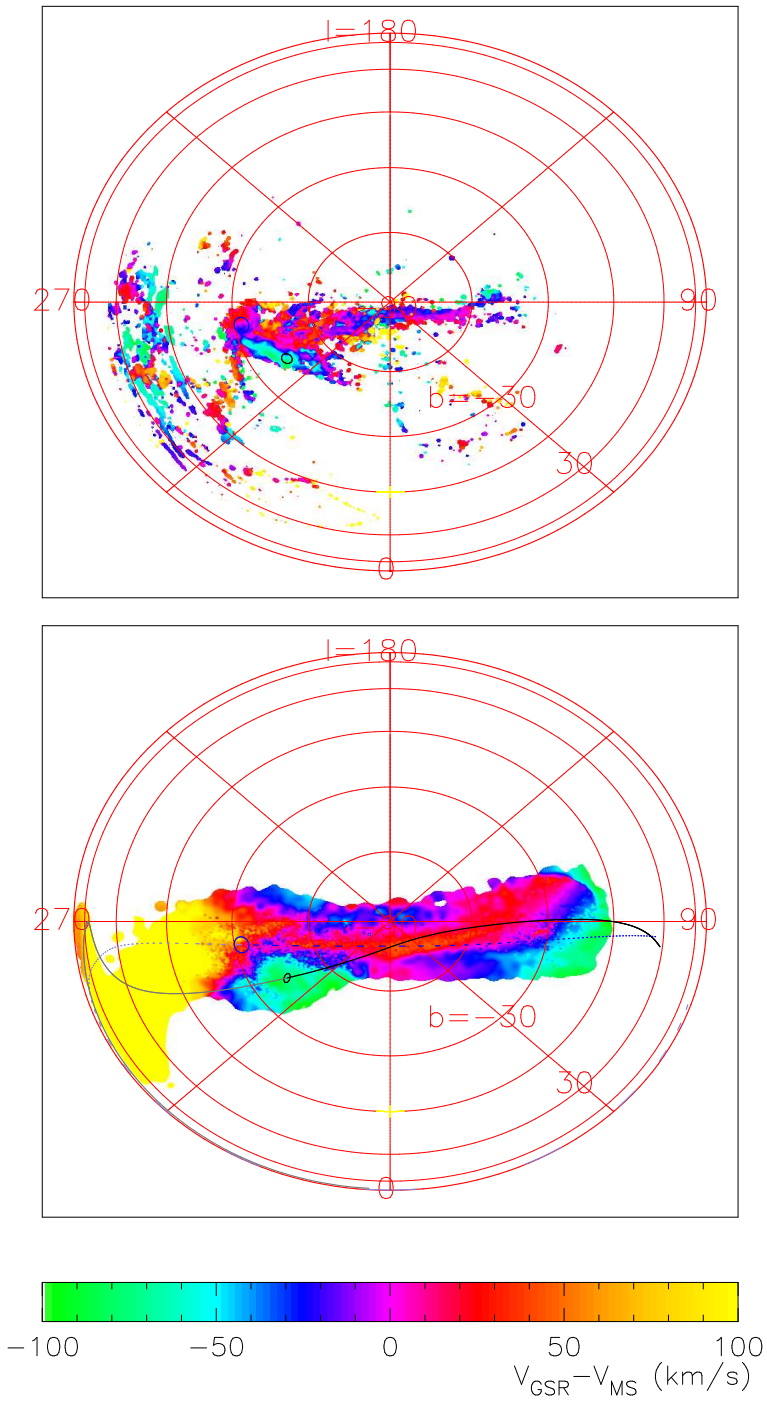

Figure 3.12: First moment maps, showing $v_{\rm GSR}$ with the MS velocity trend derived from the HIPASS dataset subtracted. This shows the observational HIPASS data (top) and that of our fiducial model (bottom). The current positions of the SMC and LMC are represented by black and blue ellipses, and in the bottom panel, the past and future 1 Gyr histories of the SMC and LMC orbit are denoted by black solid and blue dashed lines, respectively (the future 1 Gyr is shaded in a lighter colour).

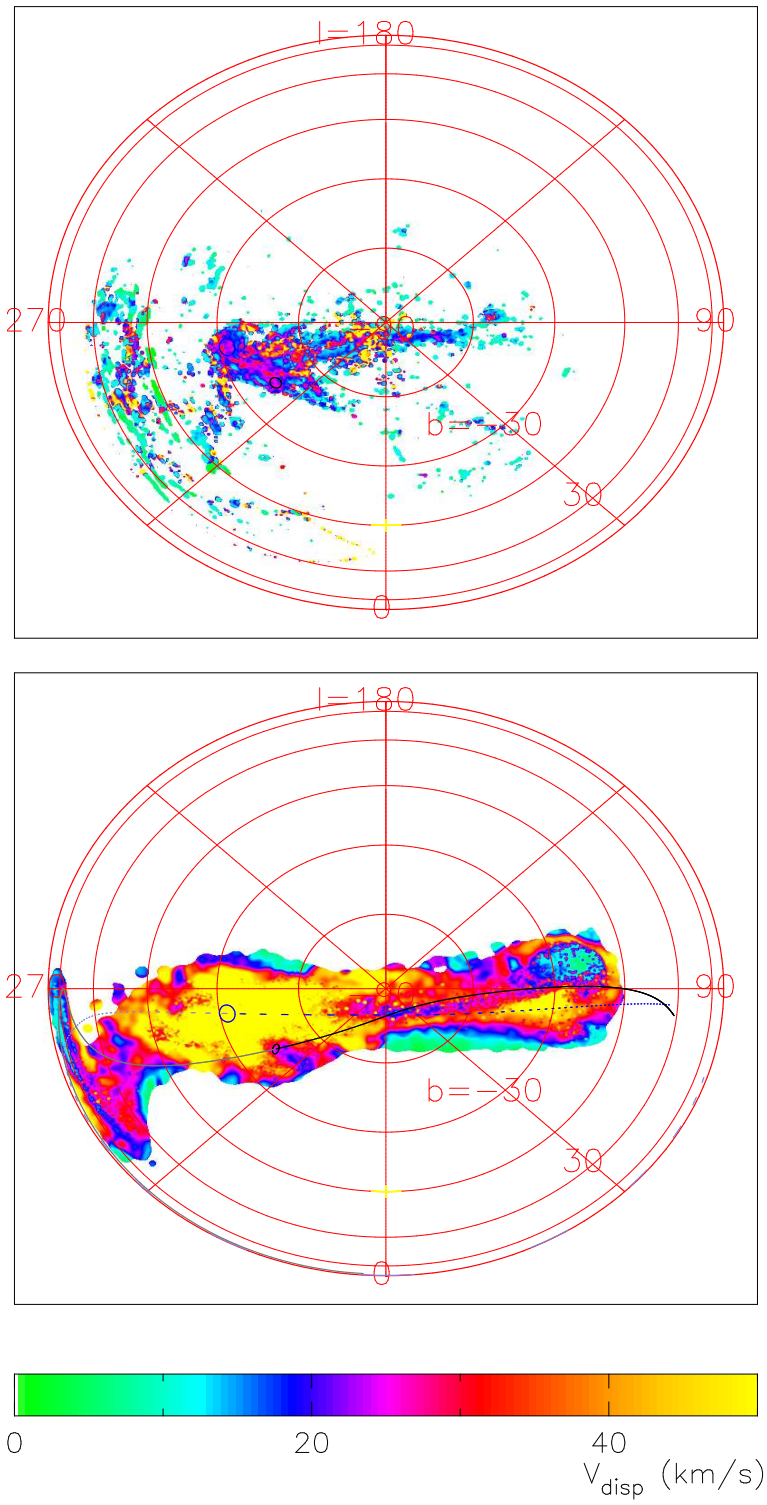

Figure 3.13: As in Figure 3.12, for the second moment maps, showing the velocity dispersion.

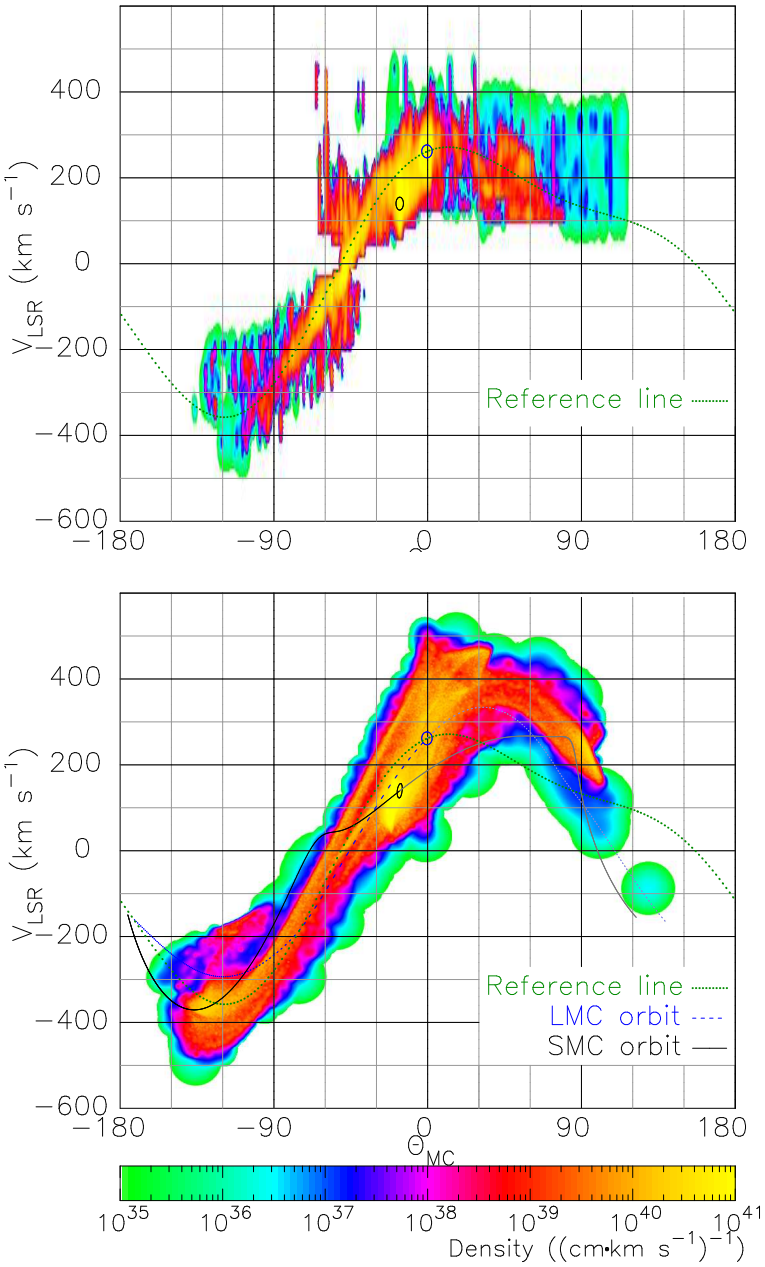

Figure 3.14: The line-of-sight velocity with respect to the Local Standard of Rest $v_{\rm LSR}$, as a function of the Magellanic longitude $\theta_{\rm MC}$, derived from the observed HIPASS dataset (top) and that of our fiducial model (bottom). The current positions of the SMC and LMC are represented by black and blue ellipses, and in the bottom panel, the past and future 1 Gyr histories of $v_{\rm LSR}$ and $\theta_{\rm MC}$ (where the longitude is defined with respect to the current position of the LMC) of the SMC and LMC orbit are denoted by black solid and blue dashed lines, respectively (the future 1 Gyr is shaded in a lighter colour). A reference line (dotted green) is drawn to show the velocity subtracted equally from both plots to yield Figure 3.12—see text for details.

and 3.10, are the radial and tangential bifurcations of the LAF, respectively.

At the tail of the MS, there is a third component, well separated spatially from the other two streams—extending from 170 to 220 kpc. It is visible through its differing heliocentric distance (Figure 3.11) and its lower negative velocity (Figure 3.14), relative to the rest of the MS. Its position of $(l, b) \sim (90°, -30°)$ coincides with the tip of the main MS components. Wakker & van Woerden (1991) suggest that the EN complex of HVCs at $(l, b) \sim (120°, -30°)$ are contiguous in $(l, b, v_{\rm LSR})$ space with the MS, hinting at a common origin, with the caveat that models must explain the abrupt disruption of the tail of the MS at $(l, b) = (90°, -40°)$. We may be tempted to equate this third component in the models with the EN complex, however the third component contributes a total H I flux of 1100 Jy km s^{-1}, a factor of 20 lower than the total flux of the EN complex (Wakker & van Woerden, 1991).

The bottom panel of Figure 3.14 demonstrates that the bifurcation of the main portion of the MS appears also in $v_{\rm LSR}$. Plotted are lines showing the history (and future) of the MCs' $v_{\rm LSR}$. Only one of the bifurcated components follows the orbit of the MCs (primarily the LMC), while the other possesses a higher velocity. Interestingly, there is a second velocity component at the position of the SMC (as well as at the head of the MS and the LAF). Mathewson & Ford (1984) observed two velocity components within the SMC itself, with a separation of $\sim 50\,{\rm km\,s^{-1}}$. While the separation of our two velocity components is much larger ($\sim 150\,{\rm km\,s^{-1}}$), it might indicate that the presence of two observed velocity components is because of a similar process.

Snapshots of the simulation, similar to those seen in Figure 3.7, hint at the origin of these bifurcations. Prior to the first major peri-Galacticon at $T = -1.5\,{\rm Gyr}$, an encounter with the LMC at $T = -2.2\,{\rm Gyr}$ drew the particles from the tip of the SMC disc closest to the LMC (and furthest from the MW), which resulted in the particles that eventually came to reside in the most distant MS component, at a Galactocentric distance of 170 to 220 kpc. The MS particles did not become "distinct" from the SMC proper until $T = -1.5\,{\rm Gyr}$; at $T = -1.05\,{\rm Gyr}$, the MS then received an impulse from an LMC encounter, which caused the spatial bifurcation of the MS. The MS was given a "kick" by the LMC at the subsequent apo-Galacticon at $T = -0.55\,{\rm Gyr}$. This encounter at $T = -0.55\,{\rm Gyr}$ resulted in the MS being broken into two kinematic components, causing the apparent velocity bifurcation.

On the other hand, a portion of the LAF comes from the particles on the same side of the disc, but closer to the SMC centre at the $T = -2.2\,{\rm Gyr}$ encounter. The

opposite side of the edge of the disc mostly consisted of particles that end up at the current time in the ICR. At $T = -0.9\,\mathrm{Gyr}$, the LMC passed through the LAF, splitting it into two bifurcated radial components.

Our models seem to create naturally both the spatial and velocity bifurcations via tidal interaction between the LMC and SMC. If this is the case, any observed bifurcation features would be strong evidence supporting the tidal formation scenario for the MS. Observationally, the top panel of Figure 3.8 shows that there is spatial bifurcation in the observed H I distribution. However, from this data alone, it is difficult to ascertain from the v_{LSR} distribution of Figure 3.14 whether there is an observed velocity bifurcation. Nevertheless, Figure 3.14 of this work, and Brüns et al. (2005) and Stanimirovic et al. (2008) with data of higher velocity resolution, show evidence for a bifurcation in v_{LSR} along the MS. The two components observed in this work are separated by approximately $100\,\mathrm{km\,s^{-1}}$ at $\theta_{\mathrm{MC}} \sim 100°$, and the two components are visible in fig. 3 of Brüns et al. (2005) between the Interface Region and Galactic Plane. There is also a hint of bifurcation (with separation of $\sim 100\,\mathrm{km\,s^{-1}}$) in the LAF at $\theta_{\mathrm{MC}} \sim 45°$.

3.4 Parameter Dependences

As discussed in Section 3.2, our simulations involve several parameters which are not well-constrained by current observations. In this section, we briefly demonstrate how the final configurations of the MS and LAF are sensitive to these free parameters. We varied parameters over a wide range of parameter space in our survey, to obtain our fiducial model (labelled "fiducial" in Tables 3.3 and 3.4). The parameter survey was performed at a lower resolution (25,000 disc and 25,000 halo particles) than the final fiducial model. We have confirmed that in the fiducial model the results of the lower-resolution simulation are consistent with the higher-resolution simulation, although, as presented above, the choice of a higher resolution enables us to discuss more detailed features. For example, in Figure 3.15, we show the H I column density map for the lower-resolution model with identical parameters as our fiducial model. The distribution of the H I column density is roughly consistent with that shown in Figure 3.8, although the higher-resolution models affords an improved examination of the finer-scale structures intrinsic to the simulated streams. The bifurcation alluded to in the previous section is an example of such a feature, and is perhaps best appreciated through an inspection of Figures 3.16 and 3.17, where the flux

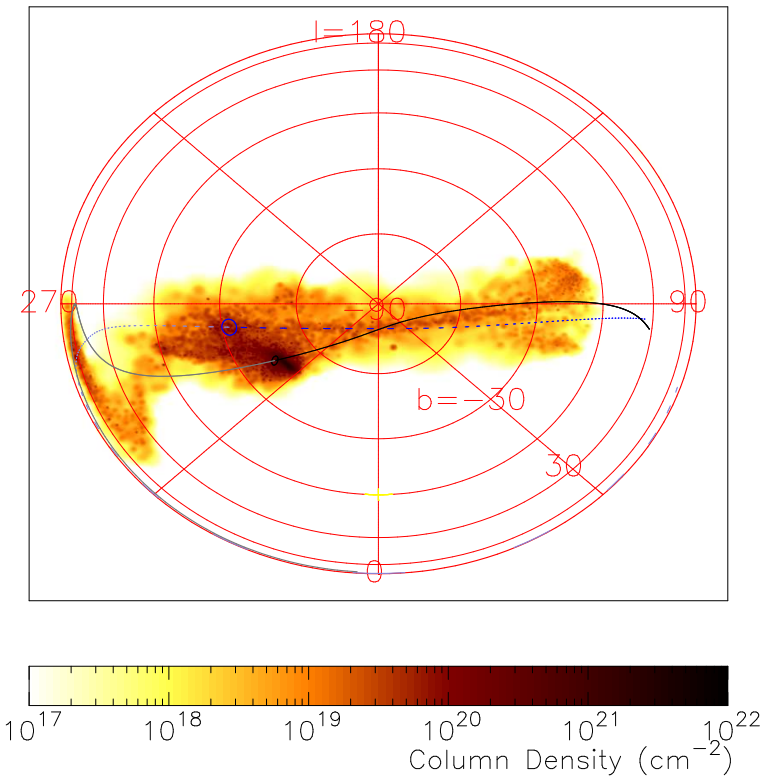

Figure 3.15: H I column density map for the lower-resolution simulation with the same parameter set as the fiducial model. Compare this with the bottom panel of Figure 3.8. The current positions of the SMC and LMC are represented by black and blue ellipses, and the past and future 1 Gyr histories of the SMC and LMC orbit are denoted by black solid and blue dashed lines, respectively (the future 1 Gyr is shaded in a lighter colour).

"excess" of the high-resolution model with respect to the lower-resolution model is presented in both the sky plane and in the $v_{\rm LSR}$ versus $\theta_{\rm MC}$ plane, and the bifurcation becomes readily apparent.

Most of the parameter space surveyed is summarised in Tables 3.3 and 3.4 (with the additional parameters of the mass of the LMC and the strength of the dynamical frictional also being tested). Such parameters were varied through the ranges allowed by the observations in Table 3.2. The scale height of the SMC disc (tested by the model labelled "thin" in Table 3.3), the ratio of SMC disc mass to SMC halo (DM) mass (tested by the models labelled "halo" and "disc"), the extent of the halo (labelled "extended"), the velocity dispersion of the SMC disc (labelled "hot"), and the final total mass of the SMC (varying the mass of the SMC for the purposes of the orbit calculation) were found to be not important to the evolution of the system. Both the velocity dispersion of the disc and the ratio of H I disc and DM mass of

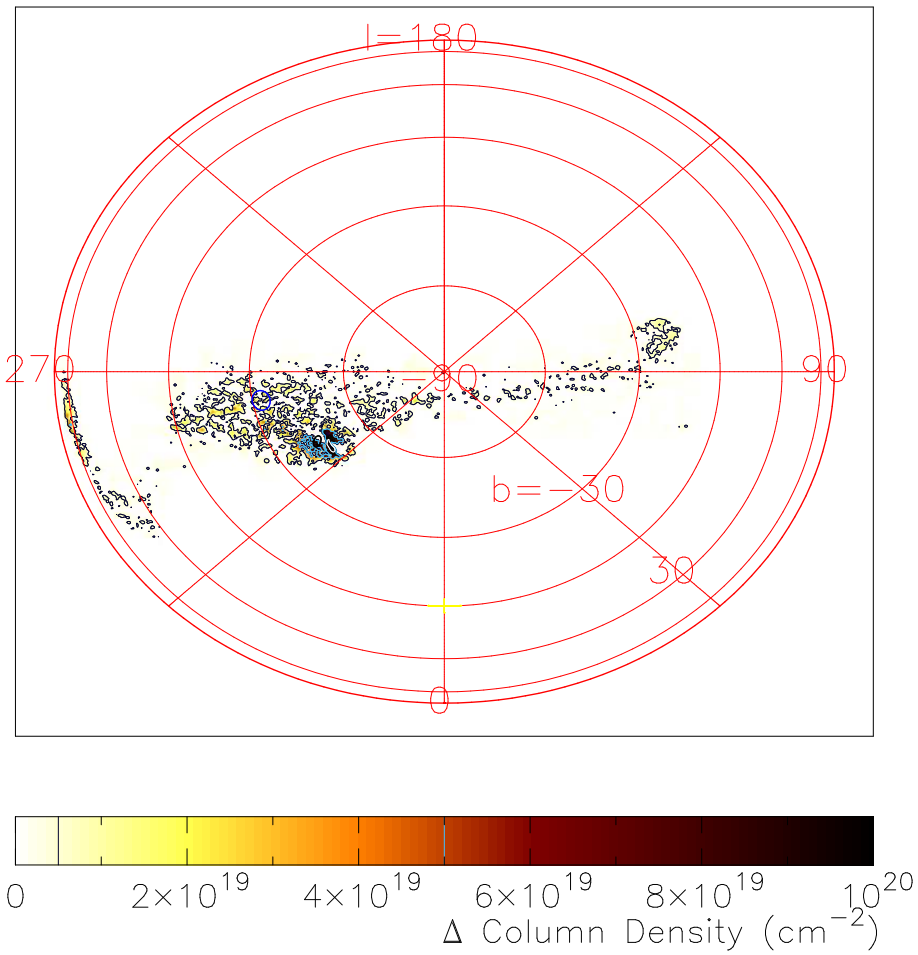

Figure 3.16: H I column density excess, for the high-resolution model over the low-resolution model, demonstrating the finer features visible particularly in the bifurcation of the stream. Black, blue and white contours are overlayed at 5×10^{18}, 5×10^{19} and $5 \times 10^{20}\,\mathrm{cm}^{-2}$, respectively. The current positions of the SMC and LMC are represented by black and blue ellipses.

the halo simply scale the velocity dispersion and quantity of H I found in the final LAF, MS and MCs in a linear fashion. The extent of the DM halo has an effect on the stripped DM, but such changes are unobservable by the nature of DM, and it had no effect on the gas stream. Increasing the initial SMC mass to the maximum allowed value of $3.6 \times 10^9\,\mathrm{M}_\odot$ (labelled "heavy" and "v. heavy"), was found to lead to slightly less mass being stripped into the streams, since the SMC particles became further bound.

In the parameter survey, the orbits of the MW, LMC and SMC were derived assuming the mass of the SMC is constant. However, we find that the SMC bound mass decreases from 3×10^9 to $1.5 \times 10^9\,\mathrm{M}_\odot$ approximately linearly with time between

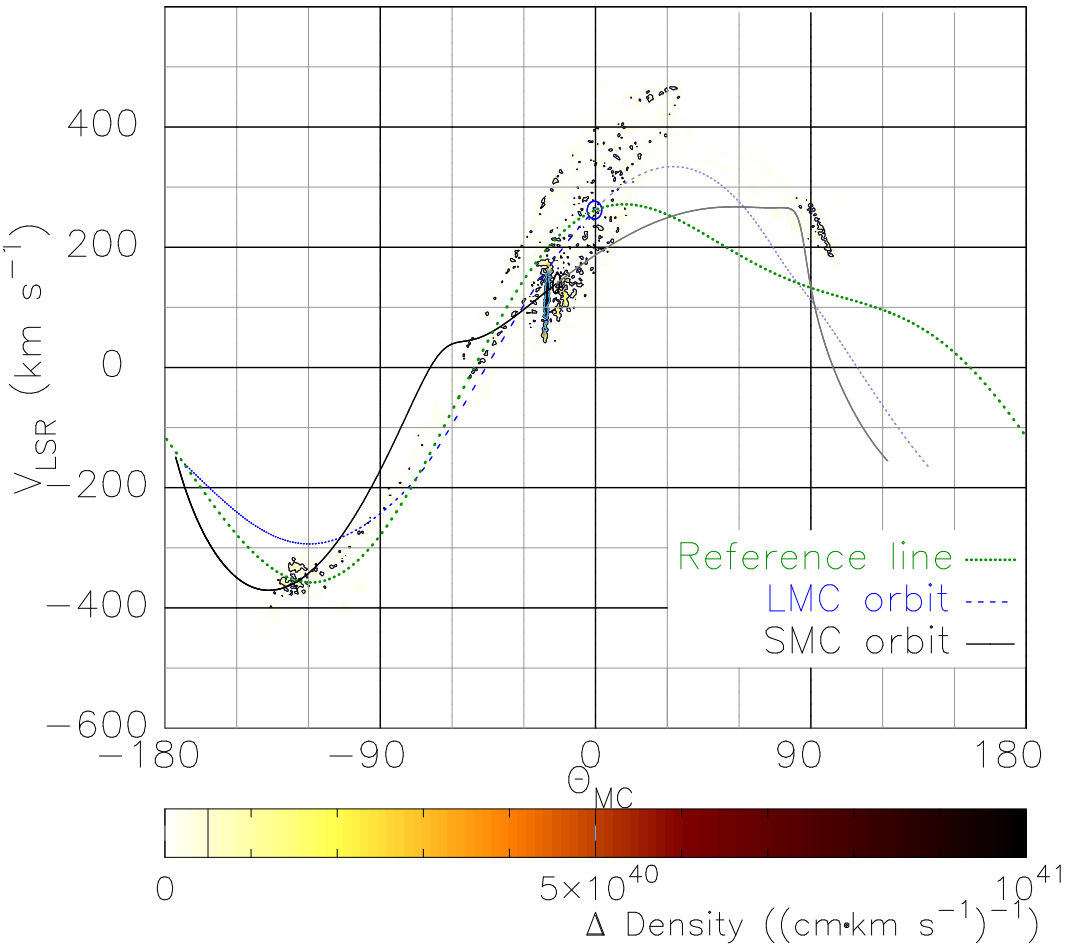

Figure 3.17: H I flux excess in the $v_{\rm LSR}$ versus $\theta_{\rm MC}$ plane, for the high-resolution model over the low-resolution model, demonstrating the finer features visible. Black and blue contours are plotted at 5×10^{39} and $5 \times 10^{40} (\mathrm{cm\,km\,s^{-1}})^{-1}$, respectively. The current positions of the SMC and LMC are represented by black and blue ellipses.

$T = -2.25\,\mathrm{Gyr}$ (near the first interaction between the LMC and SMC), and $T = 0$. Such mass-loss may affect the orbit and the final features of the MS and LAF (e.g. Zhao, 2004; Knebe et al., 2005). Thus, we explore the effects of decreasing the mass of the SMC linearly with time from 3.0×10^9 to $1.5 \times 10^9\,\mathrm{M}_\odot$, with initial conditions matching the fiducial model. We find that there is little change to the orbits, since the LMC, rather than the less massive SMC, primarily determines the orbit of both bodies in Equations (3.4) and (3.5). As a result, we confirmed by running simulations that the final features of the MS and the LAF are also not influenced heavily by the time evolution of the SMC mass. Thus, in all other simulations in the parameter survey, we use the orbits predicted with no evolution of the SMC mass. We now highlight the influence of the most important input parameters.

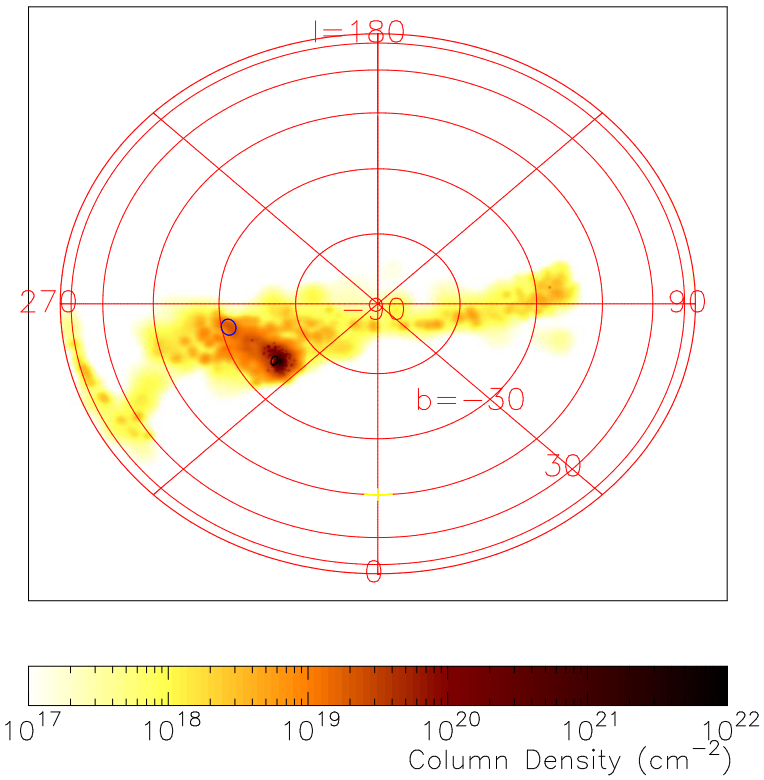

Figure 3.18: H I column density map for models with a smaller scale length (1.4 kpc) for the initial SMC disc. The current positions of the SMC and LMC are represented by black and blue ellipses

3.4.1 The Initial Scale Length of the SMC Disc

We find that the final H I distributions are sensitive to the scale length of the initial SMC disc. Figure 3.18 shows the column density map of a model with a smaller scale length (1.4 kpc) for the initial SMC disc. This reduced scale length results in a lower total H I flux for the MS, as the initially more concentrated SMC mass distribution results in less material being stripped from the disc. Since the fiducial model does not have a total H I flux high enough to match perfectly the observations (Section 3.3.3), we conclude that reducing the SMC scale length is not appropriate. It is also worth noting that the smaller scale length model leads to a less significant bifurcation in the simulated MS.

To quantify the difference between the models labelled "very conc." (scale length $R_{\rm d} = 1.4$ kpc) in Table 3.4 and the fiducial model, we have measured the H I masses and total fluxes within the regions delineated as the MS in Figure 3.8. As a result, the low-resolution simulation of the fiducial model has an H I mass in the MS of

$2.4 \times 10^8\,\mathrm{M}_\odot$ and total H I flux of 2.5×10^5 Jy km s^{-1}. The low-resolution simulation has a very similar mass to that of the high-resolution case (see Section 3.3.3). On the other hand, the small scale length model leads to a MS H I mass and total flux of $1.8 \times 10^8\,\mathrm{M}_\odot$ and 1.9×10^5 Jy km s^{-1} respectively, which is significantly smaller than that of the fiducial model. Since the fiducial model has a mass which is somewhat lower than that inferred from the HIPASS dataset, we again conclude that the models derived with the reduced initial scale length for the SMC perform worse than the fiducial model.

The H I survey of late-type dwarf galaxies by Swaters et al. (2002) suggested that the range of scale lengths of the gas disc for galaxies which have a similar H I mass to that of the SMC is 1.5 – 4.5 kpc. The scale length of our fiducial model (3.5 kpc) appears reasonable, and thus the progenitor of the SMC is considered to have had a large H I disc before the SMC fell towards the MW.

We note that choosing a smaller scale radius is similar to setting a small truncation radius, in that the SMC material is concentrated more strongly towards the centre of the SMC, where it is more difficult to tidally strip. We obtain similar results to the above when we choose smaller SMC truncation radii, such that the stream is substantially retarded when the truncation radius is reduced from 7 kpc to 3 kpc (labelled "3kpc", "5kpc", "6kpc", "6.5kpc" after their respective disc diameters in Table 3.4). In this situation, the MS H I mass and total flux are reduced to $7.2 \times 10^7\,\mathrm{M}_\odot$ and 7.0×10^4 Jy km s^{-1}. The LAF mass is scaled in a similar manner in both cases.

3.4.2 The Inclination Angle of the SMC

As mentioned in Section 3.2.3, the current inclination angle of the SMC is unknown, and the initial disc angle θ and ϕ are free parameters in our simulations. Figure 3.19 shows the H I column density distribution for models with $(\theta, \phi) = (30°, 210°)$ and $(45°, 230°)$ (but otherwise identical to the fiducial model), to demonstrate how these angles affect the final distribution of the MS and LAF. We remind the reader that we use $(\theta, \phi) = (45°, 210°)$ in the fiducial model, and therefore small differences of only 20° in the initial inclination angle have quite a marked effect on the details of the final distribution. If accurate observations of the current inclination angle of the SMC were to be made, it would provide a strong constraint on any putative model of the formation of the MS.

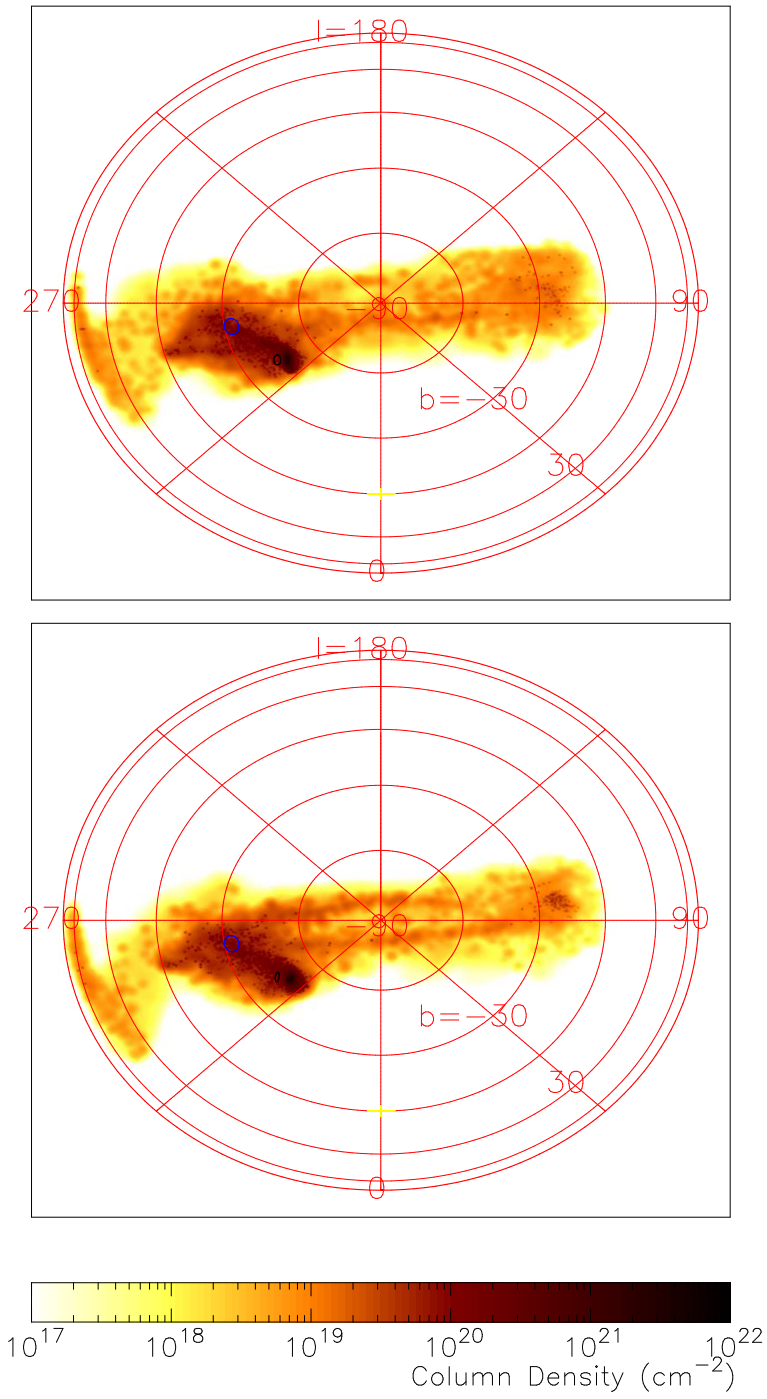

Figure 3.19: H I column density map for the model $(\theta, \phi) = (30°, 210°)$ (top) and $(45°, 230°)$ (bottom). The current positions of the SMC and LMC are represented by a black ellipse (the ellipse is the projection of the SMC disc at the given angle) and blue circle respectively.

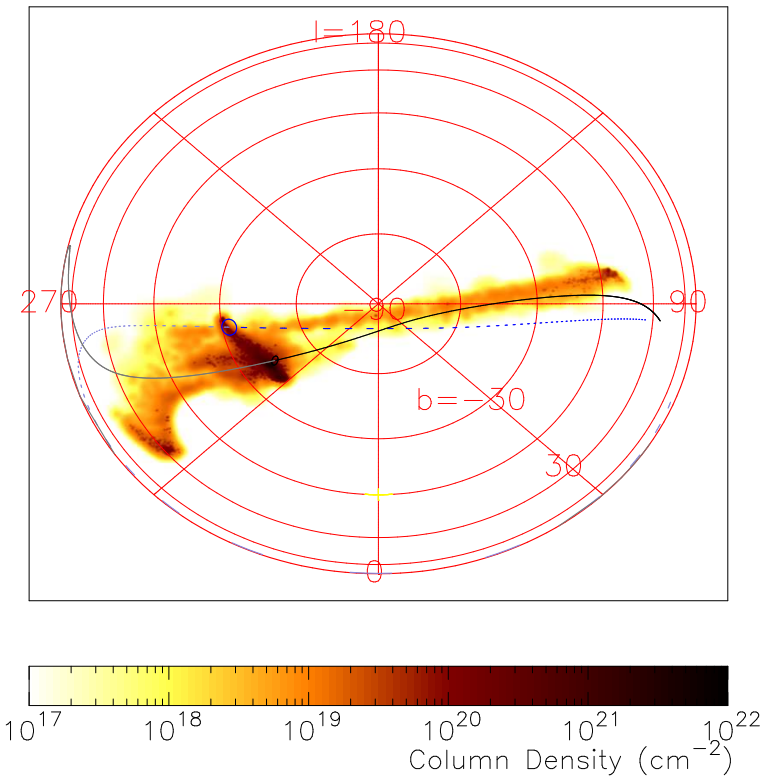

Figure 3.20: H I column density map for the model with an lower LMC mass of $1.5 \times 10^{10}\,M_\odot$. The current positions of the SMC and LMC are represented by black and blue ellipses. The changed past and future 1 Gyr histories of the orbit resulting from this differing LMC mass are presented by black solid and blue dashed lines for the SMC and LMC respectively.

3.4.3 The Mass of the LMC

Another unknown parameter is that of the mass of the LMC itself. At the time of the GN96 study, the mass of the LMC was believed to be $\sim 2 \times 10^{10}\,M_\odot$ (e.g. Schommer et al., 1992). However, recently some authors claim a lower mass for the LMC (e.g. van der Marel et al., 2002, who suggested that the mass of the LMC within $R < 8.9\,\mathrm{kpc}$ is about $9 \times 10^9\,M_\odot$). Motivated by such claims, we also ran models with varying orbital parameters, and in particular, a lower LMC mass. Figure 3.20 shows the result of a model with an LMC mass of $1.5 \times 10^{10}\,M_\odot$ (but otherwise identical to the fiducial model). Even such small differences in the LMC mass cause a large change in the orbits of the LMC and SMC. Since the MS follows the past orbit of the MCs, the angle of the MS is radically different between the model with small LMC mass, and both the fiducial model and the observed MS. This result suggests that such a low mass LMC is unlikely, *if* the MS is the result of

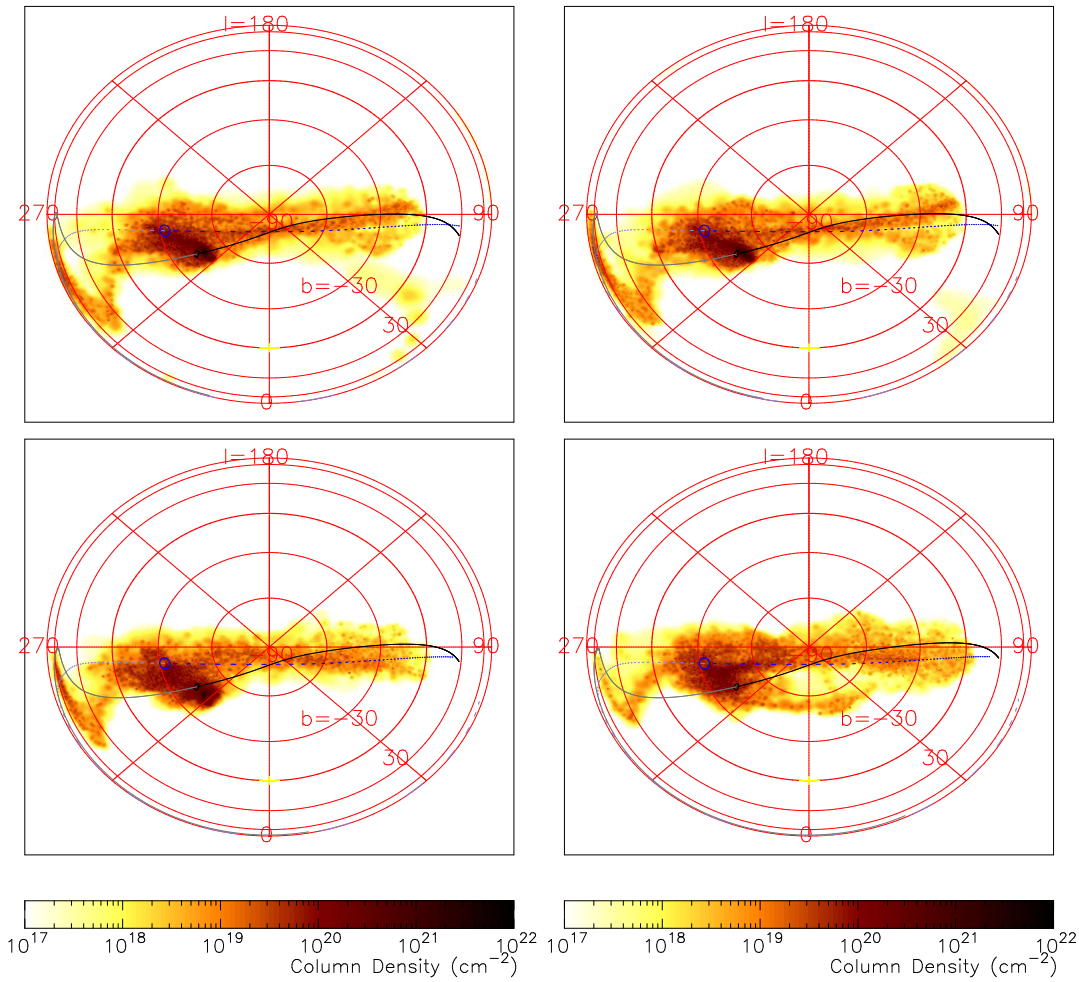

Figure 3.21: H I column density map for model with strength of the dynamical friction $\ln(\Lambda) = 1.5$ (top left), $\ln(\Lambda) = 2$ (top right), $\ln(\Lambda) = 4.5$ (bottom left) and $\ln(\Lambda) = 6$ (bottom right). The current positions of the SMC and LMC are represented by black and blue ellipses. The past and future 1 Gyr histories of the orbit resulting from these varying strengths of dynamical friction are presented by black solid and blue dashed lines for the SMC and LMC respectively.

tidal interactions. Weinberg (2000), after finding the tidal radius of the LMC, come to a similar conclusion.

3.4.4 Dynamical Friction

The strength of the dynamical friction term in Equation (3.6) is parameterised by $\ln(\Lambda)$, which we vary from 1.5 to 6, with $\ln(\Lambda) = 3$ in the fiducial model. Figure 3.21 shows the H I column density distributions for our models to demonstrate how the dynamical friction subtly affects the orbits with large consequences to the

modelled MS and LAF. Hashimoto et al. (2003) suggest that $\ln(\Lambda) = 3$ is too high for the LMC, causing the system to evolve too fast. However, we find that weaker dynamical friction results in a separate component of the MS forming, and the LAF becomes more extended. Stronger dynamical friction results in a distorted MS and less extended LAF. The observational data does not discriminate strongly between the models with $2 \leq \ln(\Lambda) \leq 4.5$.

3.5 Toward a More Self-Consistent Model: Gas Dynamics and Star Formation

To demonstrate how gas physics, star formation, and SNe feedback affect the predictions from our pure N-body simulations, we need to model the MS taking into account such physics self-consistently. This section, as a pioneering work, shows our first attempts. Admittedly as discussed below, these models are too simple. Nevertheless, they are useful to obtain a rough idea of the effects of these physics, and are a valuable insight into how to construct more self-consistent models in a future study.

We demonstrate two hydrodynamical models, one with SNe feedback, and one without. From Equation (2.30), we set the dimensionless star formation efficiency to $c_* = 0.5$. For the model with feedback, the magnitude and effect of SNe in Equation (2.37) is parameterised by $\epsilon_{\rm SN} = 0.1$ and $f_v = 0$, following Kawata & Gibson (2003a,b). This sets the initial energy of a SN to be 10^{50} erg and the kinetic feedback $E_{\rm kin} = 0$, implying all of the available energy of a SNe increases the thermal energy of the gas, and none is used to perturb the gas velocity field (Kawata & Gibson, 2003a).

The initial conditions used were that of the output of GalactICs, not evolved in a prior equilibrium run. There are no stars in the initial conditions, and so they can not be in equilibrium (Section 3.2.2). There will thus be a burst of star formation at the onset of the simulation. Figure 3.22 shows the star formation history (SFH) of the model without any SNe feedback, mass loss from stars nor metal enrichment, during both the equilibrium run and the simulation run. There is a second burst of star formation ~ 0.75 Gyr into the equilibrium run, as a result of the formation of the stellar spiral arms. The SFH of the simulation run mirrors the SFH of the equilibrium run, indicating that much of the star formation is artificially the result

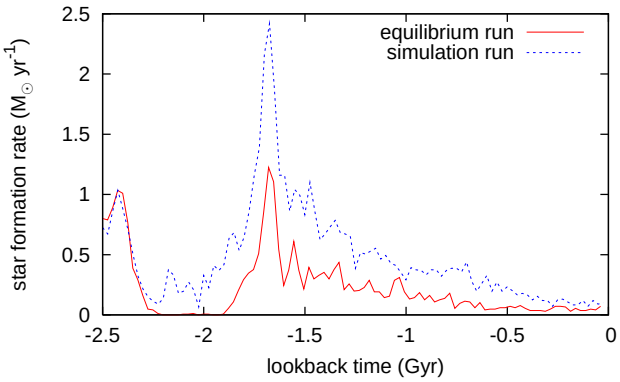

Figure 3.22: Star formation history of the hydrodynamical version of our fiducial model, without SNe feedback.

of the initial conditions not being in equilibrium.

Despite the simplicity of the initial conditions, Figure 3.23 shows that the shape of the gas streams are relatively unchanged from the pure N-body fiducial model. Figure 3.24 shows the column density maps of H I and H II obtained from the simulation as described in Section 2.2.7. Despite the extra heating of the disc, the MS is less extended than the pure N-body case. Less gas has been ejected into the stream, because of the excessive star formation partially exhausting the supply of gas. Despite the excessive star formation, the stellar content of the MS is minimal. The total H I flux contributed by the modelled MS and LAF are 1.0×10^5 Jy km s^{-1} and 1.2×10^4 Jy km s^{-1}, respectively. The modelled LAF contains a high fraction of ionised hydrogen, such that if it was not ionised at all, the total H I flux contributed by the LAF would be 2.0×10^4 Jy km s^{-1}. These are reduced somewhat compared to the fluxes from the pure N-body fiducial case obtained in Section 3.3.3, where we find 2.3×10^5 Jy km s^{-1} and 7.9×10^4 Jy km s^{-1} for the MS and LAF, respectively.

Figure 3.25 shows the SFH during both the equilibrium run and the simulation run, including SNe feedback and metal enrichment. There is no second burst of star formation, and instead the star formation is continual and excessive. The SFH of the simulation run again mirrors the SFH of the equilibrium run. We show in Figure 3.26 and Figure 3.27 that the extra heating resulting from the initial conditions produces a more extended MS and LAF. In the observed MS, the density of the stream is found to decrease over the length of the stream. Tidal models have been criticised in the past because they have not been able to reproduce this decrease (Moore & Davis, 1994; Mastropietro et al., 2005). If not an artifact of the imperfect initial

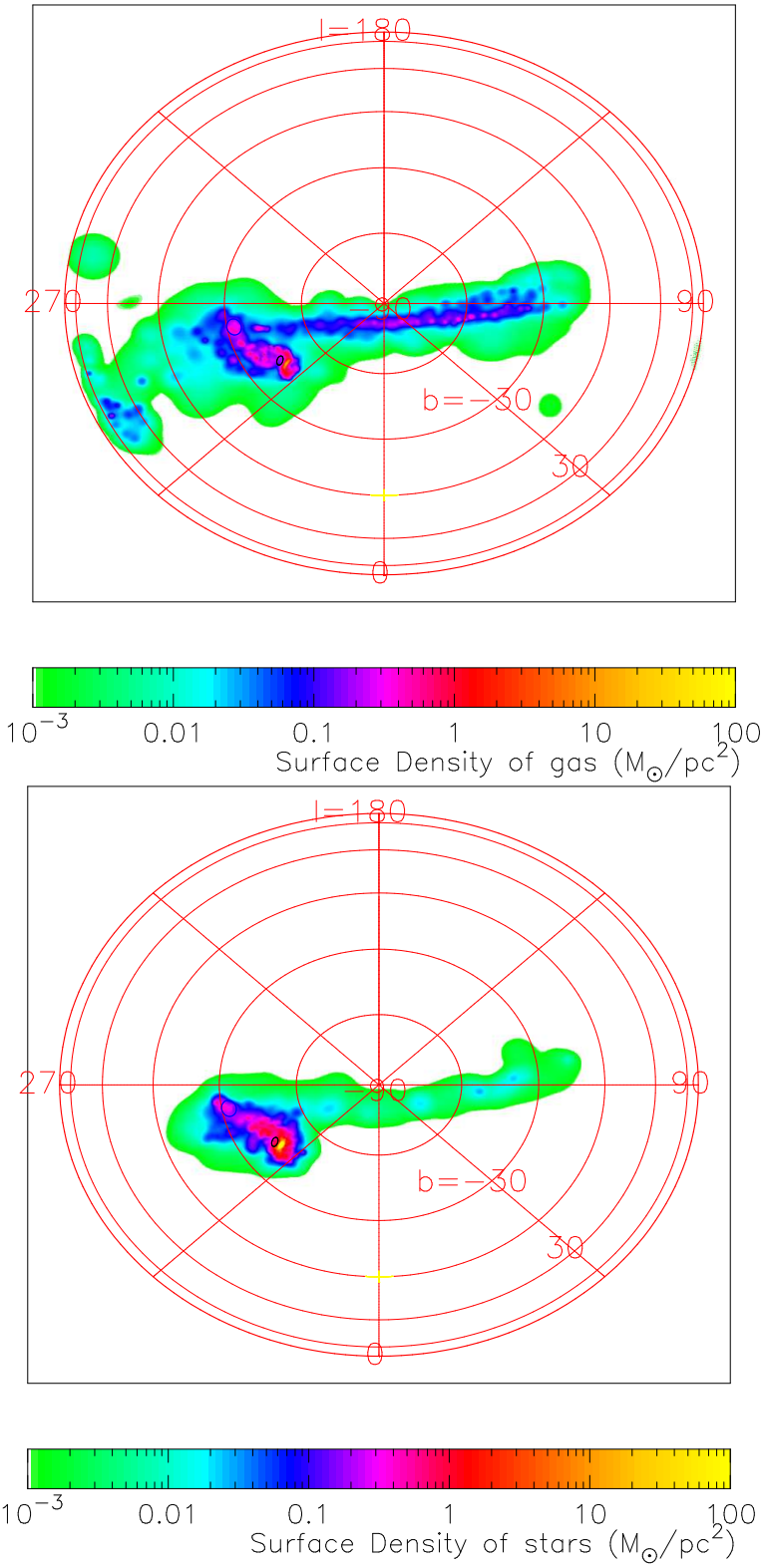

Figure 3.23: Surface density of all gas (top) and stellar (bottom) material in a hydrodynamical version of our fiducial model, without SNe feedback. Current positions of the SMC and LMC are represented by black and blue ellipses, respectively. The density scaling is identical in both maps.

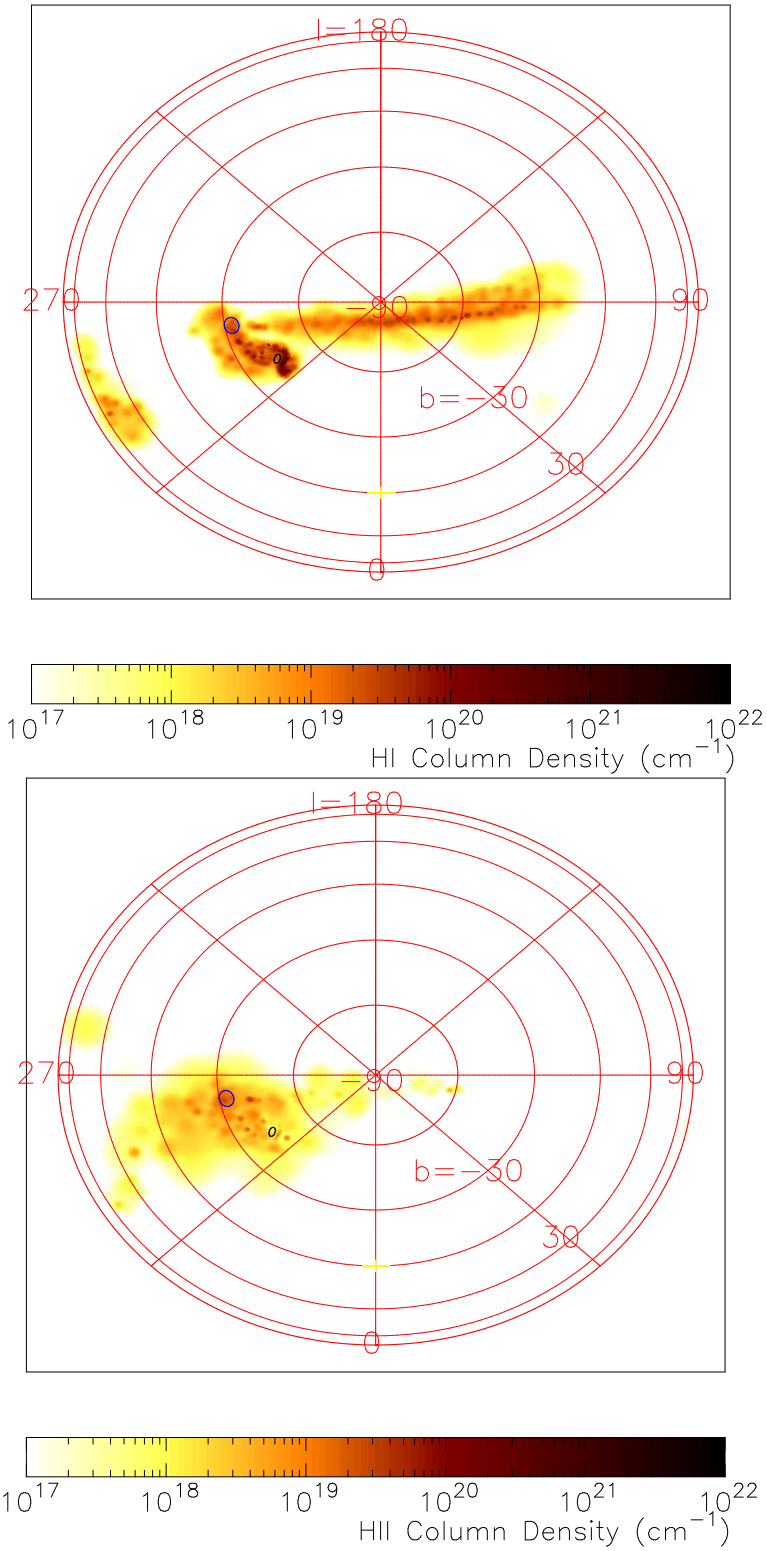

Figure 3.24: Column density of H I (top) and H II (bottom) in a hydrodynamical version of our fiducial model, without SNe feedback. The current positions of the SMC and LMC are represented by black and blue ellipses, respectively. The colourmap scaling is identical in both maps.

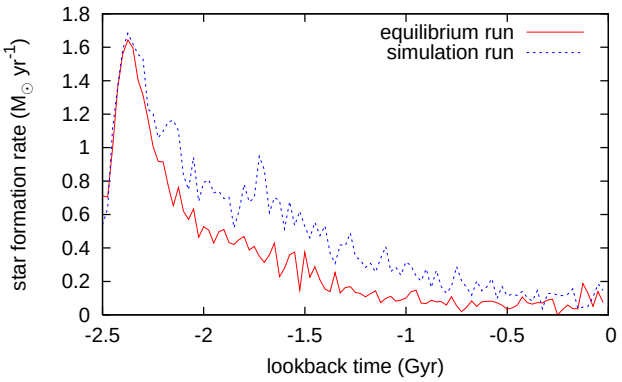

Figure 3.25: Star formation history of the hydrodynamical version of our fiducial model, with SNe feedback.

conditions, then the simulation with SNe feedback shows that the ejected gas falls off in density towards the tail of the MS as observations require. The tip of the MS is also quite extended, similar to the tentative results obtained from the observations of Westmeier & Koribalski (2008). However, adding feedback results in a larger stellar disc in the equilibrium run, and thus a larger stellar content in the MS in the simulation run. The increased star formation relative to the simulation without SNe feedback, decreases the mass of our MS and LAF, and also acts to increase the stellar content of the MS. The total H I flux contributed by the modelled MS and LAF are 5.4×10^4 Jy km s^{-1} and 9.2×10^3 Jy km s^{-1}. Again, from Figure 3.27, we find the H II fraction is high, and the total H I flux if it was not ionised would be 1.7×10^4 Jy km s^{-1}.

Although our hydrodynamical models are promising, a more sophisticated treatment of the hydrodynamics and star formation is called for. A fuller treatment would require the initial conditions in the simulation run to be the result of a prior equilibrium run, with suitable metallicity gradients and temperatures assigned to the stars and gas. Because of the heating of the disc during the initial burst of star formation in the equilibrium run, the initial conditions should be modified to start with a smaller disc. The observed stellar and gas masses of the disc (Table 3.2), set additional constraints that the initial conditions would need to be verified against.

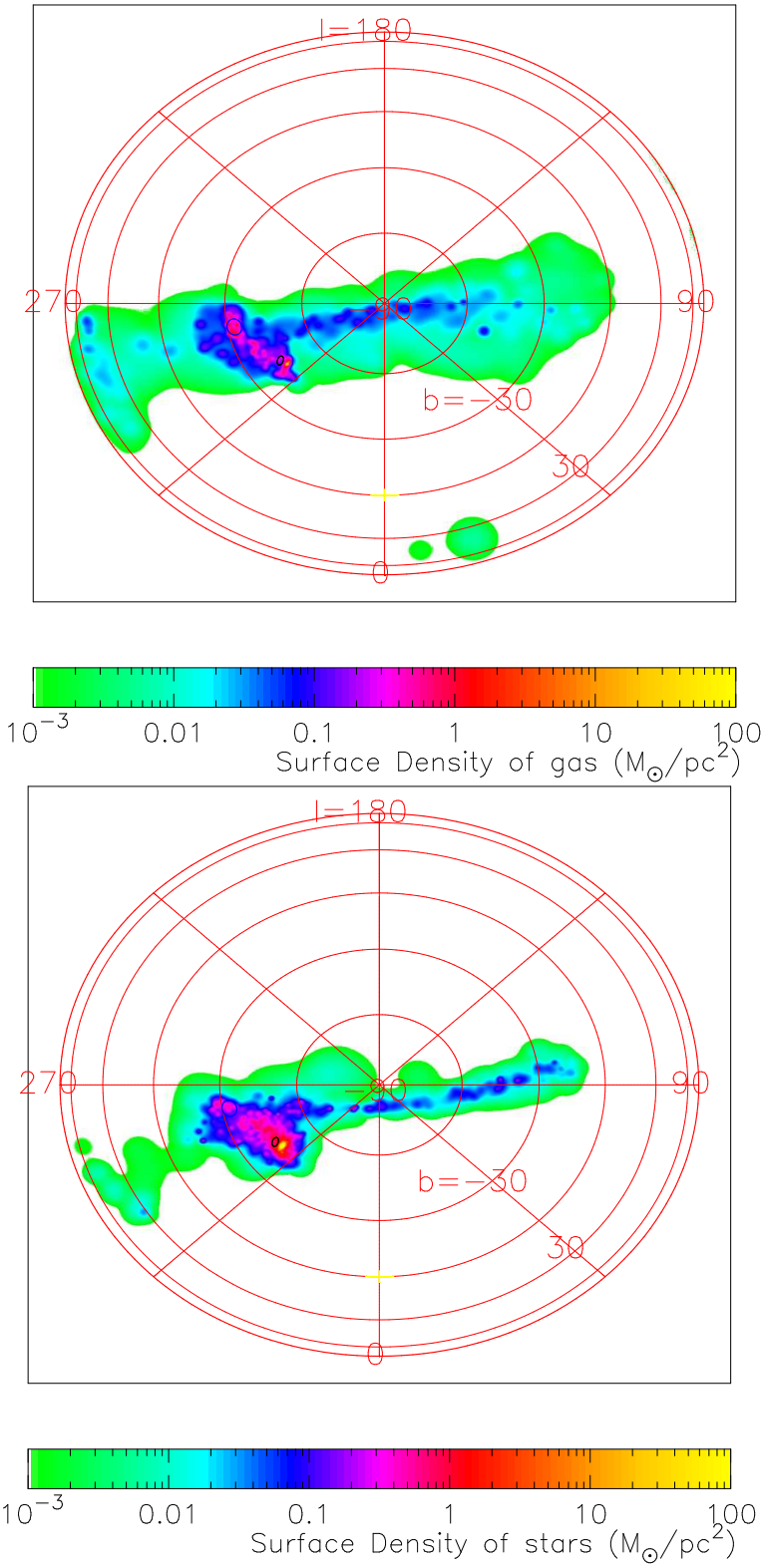

Figure 3.26: Surface density of all gas (top) and stellar (bottom) material in a hydrodynamical version of our fiducial model, with SNe feedback. The current positions of the SMC and LMC are represented by black and blue ellipses, respectively. The density scaling is identical in both maps.

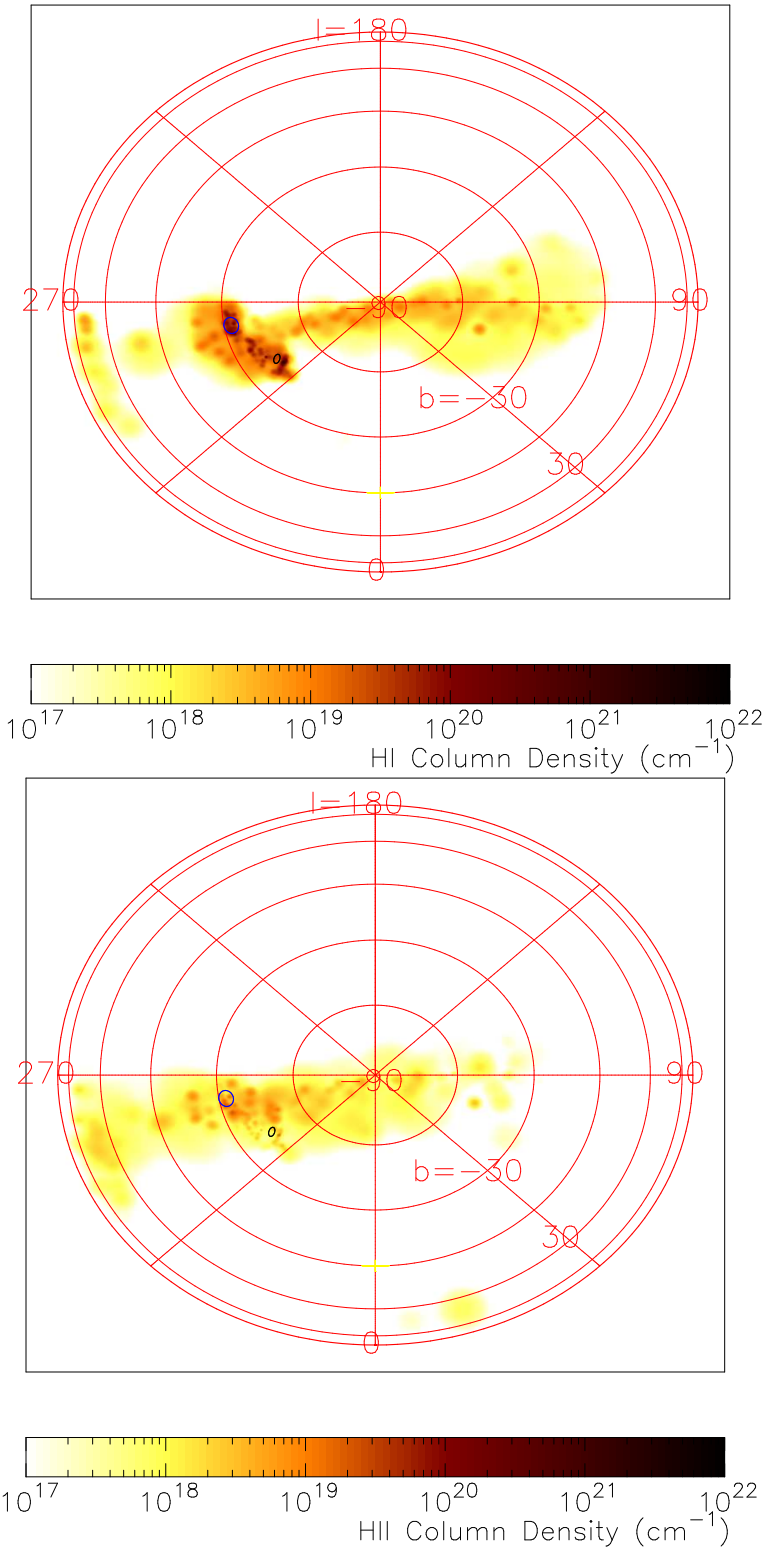

Figure 3.27: Column density of H I (top) and H II (bottom) in a hydrodynamical version of our fiducial model, with SNe feedback. The current positions of the SMC and LMC are represented by black and blue ellipses, respectively. The colourmap scaling is identical in both maps.

3.6 Summary and Discussions

We have carried out high-resolution, N-body simulations of the history of the SMC disturbed by tidal interactions with the MW and LMC. We have surveyed most of the possible parameter space for the SMC orbit and the properties of the initial SMC disc, and found the best model. The increased numerical resolution of $\sim 7\,\mathrm{Jy\ km\,s^{-1}}$ per particle for the H I flux, ~ 30 times higher than the previous studies (GN96; G99; YN03), made it possible for us to examine the detailed features of both leading and trailing tidal streams. Taking advantage of this higher resolution, we for the first time made a direct and quantitative comparison of the simulation results with newly available high quality observational data from HIPASS (Barnes et al., 2001). We convolved the HIPASS dataset with the identical software tools used to analyse the simulated datasets, and compared the results in identical manners. Such comparisons confirm the conclusions of previous studies—that the existence of the LAF and MS can be well explained by the leading and trailing streams of the SMC created by tidal interactions with the MW and LMC.

We found a fiducial model in which the SMC disc was initially less centrally concentrated (with a scale radius of 3.5 kpc) and more extended (with a diameter $> 7\,\mathrm{kpc}$) than prior studies such as GN96 and YN03 indicated. Smaller discs were found to be too tidally bound and the resulting streams were too weak. The initial SMC disc was oriented with $(\theta, \phi) = (45^\circ, 210^\circ)$, and small differences of 20° were enough to disrupt the shape of the streams. Contrary to some recent studies (e.g. van der Marel et al., 2002) which indicated a reduced LMC mass of $\sim 1\times10^{10}\,\mathrm{M_\odot}$, we found that even a $1.5\times10^{10}\,\mathrm{M_\odot}$ LMC mass leads to an unacceptable deviation in the modelled MS position from that observed. We thus support the findings of Weinberg (2000) who found an LMC mass of $2 \times 10^{10}\,\mathrm{M_\odot}$. We found the observational data does not strongly differentiate between models with dynamical friction strengths $2 \leq \ln(\Lambda) \leq 4.5$, the lower values of which are consistent with Binney & Tremaine (1987) and Hashimoto et al. (2003). Varying the dynamical friction between the larger range of $1.5 \leq \ln(\Lambda) \leq 6$ does not have a large effect on the projected orbits of the MCs, however it does have profound effects on the shape of the stream.

Some parameters of the models do not affect properties of the stream that are able to be observed. Such unconstrained parameters include the scale height of the SMC disc, the extent of the DM halo, and the final total mass of the SMC (adopting the same initial mass of the SMC as the fiducial model, but calculating

the orbit based on the monotonically decreasing mass of the SMC as it is stripped). Increasing the initial SMC mass the maximum allowed by observations, $3.6\times10^9\,\mathrm{M}_\odot$, was counter-intuitively found to lead to slightly less mass being stripped into the streams, since the SMC particles became more tightly bound. The extent of the DM halo effects the stripped DM, but such changes are unobservable at the current time, and it had no effect on the gas stream. Both the velocity dispersion of the SMC disc and the ratio of H I disc and DM mass of the SMC halo simply scale the velocity dispersion and quantity of H I found in the final LAF, MS and MCs in a linear fashion.

Another benefit of the higher-resolution simulations performed here is the identification of the bifurcation of the MS and LAF both spatially (radially and tangentially) and kinematically. The tangential bifurcation formed at $T = -1.05\,\mathrm{Gyr}$ when an impulse was imparted by the LMC onto the MS during an encounter, and the radial bifurcation formed at $T = -0.9\,\mathrm{Gyr}$ when the LMC passed through the LAF. The kinematical bifurcation formed at $T = -0.55\,\mathrm{Gyr}$ when the MS was given a "kick" by the LMC at apo-Galacticon. Our simulations predict that if the MS is created by a tidal interaction with the LMC, the bifurcation would appear both in the H I column density map and the line-of-sight velocity versus Magellanic longitude plane. Current observations are consistent with the existence of a spatial bifurcation in the H I column density map (top panel of Figure 3.8). In the velocity versus Magellanic longitude plane, it is difficult to make a firm conclusion from the current HIPASS data, although it is interesting that the SMC itself is found to consist of at least two velocity components (Mathewson & Ford, 1984), perhaps caused by the same tidal disruption processes that form the bifurcation in our models. With high velocity and spatial resolution observations, Stanimirovic et al. (2008) have made a tentative confirmation of the existence of a kinematic bifurcation in the MS tip, and Brüns et al. (2005) have also tentatively confirmed a velocity bifurcation in the LAF. If confirmed, it would provide strong evidence that the MS and LAF were created by tidal interactions.

With the addition of hydrodynamics and star formation to the fiducial model, we found the shape of the MS was largely unchanged, although the details of the stream were poorly matched because of the simplicity of the initial conditions. A more sophisticated treatment of the gas and star formation would require the disc gas and stars to be modelled in equilibrium prior to the initiation of the simulation, such that the SMC gas and stellar discs were already at the required size and masses.

Our hydrodynamical simulation with SNe feedback shows the H I density decreasing down the length of the MS, as observations require, but which has not typically been seen in tidal models of the MS. The tip of the MS is found to be more extended than the pure N-body case, and it appears similar to the tentative results obtained from the observations of Westmeier & Koribalski (2008).

Despite our success in modelling the MS and LAF, our quantitative comparison have revealed extant problems with the models (some minor; some more significant). We found that even in our best model (1) the shape of the MS is too extended in width and maybe in length (Section 3.3.3); (2) the total H I flux of the MS is too low, and thus the mass of the MS is too low (Section 3.3.3); (3) the angle the LAF emanates from the MCs is not entirely consistent with observations (Section 3.3.3); (4) and nor is its total H I flux consistent with observations (Section 3.3.3); (5) the velocity dispersion of the MS is too high (Section 3.3.4); and (6) the line of sight velocity of the LAF is too high (Section 3.3.4).

These problems suggest that additional physics may be required to explain the observed properties of the MS and LAF, quantitatively. We largely neglect the study of gas physics, such as hydrodynamics and dissipation by radiative cooling. Simulations in Maddison et al. (2002) indicate that dissipation causes the MS to become narrower, as we also see in Section 3.5, which might lead to a reduced velocity dispersion. Ram pressure (Moore & Davis, 1994; Mastropietro et al., 2005) is another physical process which our numerical model does not currently take into account. Although we show it does not the main shaper of the MS and LAF, ram pressure (or drag—see G99) is expected to shorten the leading arm and increase the gas density in the MS, which should help to solve the deficiencies of the model at recreating the LAF and MS with their correct shapes and densities (alternatively, observations that unambiguously linked the "EN" and "EP" populations of HVCs of Wakker & van Woerden (1991) to the MS and LAF, would support our model). If ram pressure were to also bring the MS significantly closer than the 57 kpc fixed for the observational data within this work, then the mass of the observed stream and total flux of the modelled stream would be increased, bringing them back into agreement. However, drag might lead to more problems for the length of the MS. Another possibly important mechanism is SNe feedback which might aid in ejecting gas from the SMC and/or LMC, and help to increase the gas density in the MS and LAF (Nidever et al., 2008). Finally, we note that the LAF passed very close to the centre of the MW 0.2 Gyr ago, and since we modelled the MW potential as spherically

symmetric with a constant rotational velocity of $220\,\mathrm{km\,s^{-1}}$, any deviations from this (such as the unknown contribution from the MW disc; e.g. Fich & Tremaine, 1991) would affect our modelled LAF in particular. If such effects on the LAF were to compress it or reduce its velocity, then agreement with the observations may be improved.

Chapter 4

Origin of HVCs in the Milky Way

Summary

We show that neutral hydrogen (H I) gas clouds, resembling High Velocity Clouds (HVCs) observed in the Milky Way (MW), appear in MW-sized disc galaxies formed in high-resolution Λ–dominated Cold Dark Matter (ΛCDM) cosmological simulations which include gas-dynamics, radiative cooling, star formation, supernovae (SNe) feedback, and metal enrichment. Two such disc galaxies are analysed, and H I column density and velocity distributions in all-sky Hammer-Aitoff (AIT) projections are constructed. The simulations demonstrate that ΛCDM is able to create galaxies with sufficient numbers of anomalous velocity gas clouds consistent with the HVCs observed within the MW, and that they are found within a galactocentric radius of 150 kpc. We also find that one of the galaxies has a polar gas ring, with radius 30 kpc, which appears as a large structure of HVCs in the AIT projection. Such large structures may share an origin similar to extended HVCs observed in the MW, such as Complex C.

4.1 Introduction

High Velocity Clouds (HVCs) are neutral hydrogen (H I) gas clouds with velocities inconsistent with galactic rotation[1] (Wakker & van Woerden, 1997). From our vantage point within the Galaxy, they appear to cover a large portion of the sky relatively isotropically. HVCs do not appear to possess a stellar component (e.g. Simon & Blitz, 2002; Siegel et al., 2005) and their individual distances (and masses) are generally unknown. Direct distance constraints have only been made for a select

[1]HVCs are typically defined as having $|v_{\rm LSR}| > 100\,{\rm km\,s^{-1}}$, a definition we adopt in this thesis.

number of HVCs, by looking for the absorption of intervening H I in the spectra of stars coincident with HVCs (Danly et al., 1993; van Woerden et al., 1999; Wakker, 2001; Thom et al., 2006; Wakker et al., 2007; Thom et al., 2007; Wakker et al., 2008). There are still open questions as to whether HVCs are local to the Milky Way (MW) or distributed throughout the Local Group (LG); whether they are peculiar to the MW or are common in disc galaxies; whether they are gravitationally bound or pressure confined; whether they contain Dark Matter (DM); and their degree of metal-enrichment. Additionally, only recently have observations been made for the presence of ionised metals in HVCs (e.g. Sembach et al., 2003; Collins et al., 2005; Fang et al., 2006). These observations rely on seeing lines in absorption, and there are few large scale surveys of the entire sky with enough pointings to be able to map the location of these ionised clouds, and it is not known whether the various ionisation species trace each other.

Despite uncertainty in the distances to HVCs, there are a small but growing number of HVCs that have one or more direct constraints on their possible locations, as concerted efforts are made to find stars with distance constraints themselves, that bracket HVCs. The presence or absence of appropriate absorption lines in these stars spectra indicate whether they are behind or in front of the HVC in question. Most clouds to date with direct distant constraints are unsurprisingly close, at least 2 kpc away, but within 15 kpc of the MW (Wakker, 2001; Thom et al., 2006; Wakker et al., 2007, 2008), because of the necessity of having stars beyond a HVC to set its distance upper limits. Most HVC complexes without constraints must still be within 40 kpc, since a large fraction of them have been observed with H α emission caused by the radiation leaking from the Galactic disc (Putman et al., 2003a). The most studied HVC complex to date is that of Complex C, which is ~ 10 kpc distant, has a H I and total mass of $\sim 5 \times 10^6\,\mathrm{M}_\odot$ and $\sim 8 \times 10^6\,\mathrm{M}_\odot$ respectively, and subtends $\sim 17^\circ \times 85^\circ$, implying the dimensions of 3×15 kpc (Thom et al., 2007). The metallicity of Complex C is $\log(\mathrm{Z/Z}_\odot) \sim -1$ (e.g. Gibson et al., 2001; Richter et al., 2001), and it may be accreting at the rate of $0.1\,\mathrm{M}_\odot\mathrm{yr}^{-1}$ (Thom et al., 2007).

Systematic H I surveys have routinely been carried out over the last few decades (e.g. Dieter, 1965; van Kuilenburg, 1972; Mathewson & Ford, 1984; Hulsbosch & Wakker, 1988; Barnes et al., 2001; Lockman et al., 2002; Braun & Thilker, 2004; Kalberla et al., 2005; Brüns et al., 2005; McClure-Griffiths et al., 2006) that map the location, density and velocity of H I emission, resulting from the spontaneous spin flip transition of atomic hydrogen. We can now study elements other than hydrogen.

Oxygen is the most abundant metal and O VI lines have large oscillator strengths, but it must be observed in absorption against background sources. Sembach et al. (2003), using Far Ultraviolet Spectroscopic Explorer (FUSE), find that O VI absorption lines are ubiquitous; they are seen in 60 – 85% of the ~ 100 observed quasar sightlines to the detection limit of $\sim 10^{13} - 10^{14}\,\mathrm{cm}^{-2}$ (compared to 37% of the sky being covered in H I down to $8 \times 10^{17}\,\mathrm{cm}^{-2}$; Lockman et al., 2002). These individual observations enable the construction of crude, low resolution maps of column density and velocity of the O VI. The observations show that O VI covers much of the sky, much like high velocity H I, but the maps aren't detailed enough yet to show just how clumpy the O VI clouds are.

Since O VI probes temperatures significantly higher ($\sim 2 - 4 \times 10^5\,\mathrm{K}$) than those that H I is sensitive to ($\lesssim 2 \times 10^4\,\mathrm{K}$), it potentially traces different structures. Although some of the O VI detections correlate with known H I HVCs with column densities $N(\mathrm{HI}) \geq 10^{18.5}\,\mathrm{cm}^{-2}$, the survey catalogues a new class of "highly ionised" HVCs with H I column densities below the detection threshold of single-dish radio telescopes. Collins et al. (2005) showed that since the O VI and O VII gas covers the sky, this gas must reside in the Galactic halo, as otherwise the implied mass would be too large. Fang et al. (2006) verifies that the covering factor of O VII is indeed large, with a 90% confidence that at least 63% of the sky is covered in such gas, and furthermore, find a lack of absorption corresponding to non local O VII in the LG.

Many theories have been proposed to explain HVCs, mostly based on those of Oort (1966). Blitz et al. (1999) proposed that HVCs are large "mini-halos" distributed through the filaments on Mpc-scales, travelling towards the LG. However, despite extensive searching (Thilker et al., 2004; Pisano et al., 2004; Westmeier et al., 2005a), similar clouds are not seen around other galaxies such as M31. A supernovae (SNe) driven cyclic Galactic fountain, reaching as high as 10 kpc above the disc (de Avillez, 2000), may be responsible for some solar metallicity HVCs (Bregman, 1980; Houck & Bregman, 1990; Gibson et al., 2001; Oosterloo et al., 2007). HVCs may also be the result of cooling instabilities in Cold Dark Matter (CDM) halos leading to clouds condensing out of a hot MW halo, up to 150 kpc away (Maller & Bullock, 2004). In this situation, the condensing clouds may themselves be growing through accretion as they approach the disc (Peek et al., 2008), and so the largest HVC complexes would be close, with $d \lesssim 15\,\mathrm{kpc}$. Such HVCs would be low metallicity, $\mathrm{Z} \sim 0.01$ – $0.2\,\mathrm{Z}_\odot$. Kravtsov et al. (2002) use constrained cosmological simulations of the Local Supercluster (where the initial conditions are dictated to result in a

system appearing like the Local Supercluster) to show that gas and DM are still raining down on the Galactic halo. The O VI seen in HVCs may be the result of bow shocks produced from these clumps as they travel through the dense Galactic halo, in which case they are within 50 kpc (Collins et al., 2004). HVCs have been associated with the tidal accretion of H I rich dwarf galaxies. The Magellanic Stream (MS) clearly results from the tidal disruption of the Magellanic Clouds (MCs) (Putman et al., 1998). There are also tenuous connections between HVCs and the Sagittarius Stream (Putman et al., 2004). Such clouds would appear as long streams and be at the distances of these accreting bodies, with $30\,\mathrm{kpc} \lesssim d \lesssim 50\,\mathrm{kpc}$. They would likely have intermediate metallicities.

Although most HVC complexes are likely reasonably close, there exists a differing population (Braun & Burton, 1999) of Compact High Velocity Clouds (CHVCs). Modelling the ram pressure interaction with the ambient Galactic medium, as well as the interfaces between the multiphased Cold Neutral Medium and Warm Neutral Medium cores of the CHVCs, Burton et al. (2001), de Heij et al. (2002), Sternberg et al. (2002) and Westmeier et al. (2005b) have shown that CHVCs are likely to be a different circumgalactic population $\sim 100\,\mathrm{kpc}$ from the MW (but up to 850 kpc). However, some doubt still exists, as Tufte et al. (2002) claim that the strength of the H α emissions even from CHVCs, show that they are excited by the photons escaping the Galactic disc and must be within the halo, closer than 100 kpc. Putman et al. (2003a) go so far as to say that H α measurements indicate the distances to many CHVCs are $\sim 40\,\mathrm{kpc}$.

If CHVCs are long lived and gravitationally bound, then their velocity dispersions of $\sim 14\,\mathrm{km\,s^{-1}}$ imply significant DM content with dynamical masses of $\sim 5 \times 10^8\,\mathrm{M_\odot}$, distances of $\sim 750\,\mathrm{kpc}$, and H I masses of $\sim 1 \times 10^7\,\mathrm{M_\odot}$ (Blitz et al., 1999; Sternberg et al., 2002). If circumgalactic, the CHVCs more likely to be pressure confined, and have H I masses of $\sim 3 \times 10^5\,\mathrm{M_\odot}$ each (Sternberg et al., 2002). Peek et al. (2008), using TreeSPH simulations, suggest that local HVCs are actually larger than the more distant HVCs if they are condensing out of the hot halo, and that the largest HVCs are within 30 kpc. This would suggest that CHVCs are closer than estimates which assume either a constant HVC size, or increasing DM content and sizes for HVCs further from the Galaxy.

Outside our own Galaxy, Pisano et al. (2004) report that there are no HVC-like objects with H I mass in excess of $4 \times 10^5\,\mathrm{M_\odot}$ in three LG-analogues. They suggest that if HVCs are a generic feature, they must be clustered within 160 kpc of the host

galaxy, ruling out the original Blitz et al. (1999) model in which HVCs are gas clouds distributed in filaments on Mpc-scales. Thilker et al. (2004) and Westmeier et al. (2005a) find 16 HVCs around M31, with H I masses ranging from 10^4 to $6 \times 10^5\,M_\odot$. Most of the HVCs are at a projected distance < 15 kpc from the disc of M31. Some clouds appear to be gravitationally dominated by either DM or as yet undetected ionised gas. They also found two populations of clouds, with some of the HVCs appearing to be part of a tidal stream, and others appearing to be primordial DM dominated clouds, left over from the formation of the LG.

The various formation scenarios can be differentiated via the determination of distances and metallicities to the HVC populations. Knowing the metallicity and distances, we would be able to estimate the rate of accretion of low metallicity gas as Thom et al. (2007) have done for Complex C. We would know the rate of circulation of the Galactic fountain (Wakker et al., 2008), and we could calibrate the fraction of ionising photons escaping from the MW disc, since we see H α in many HVCs (Bland-Hawthorn & Maloney, 1999). In an attempt to answer the question of their origin, Putman & Moore (2002) performed a purely N-body simulation of a LG analogue and, assuming the gas distribution follows DM, found a population of HVCs which they compared to the MW. While they found some similarities between the simulation and the MW's HVC population, the observed HVCs are likely decoupled from the DM they were simulating, limiting the ability of the simulations to accurately predict properties of the HVCs.

In this Chapter, we present simulation results of two generic MW sized disc galaxies formed in Λ–dominated Cold Dark Matter (ΛCDM) cosmological hydrodynamical simulations. We show that H I clouds naturally result from these simulations and that the simulated galaxies show HVCs comparable in population to the observed ones. We also find that large HVCs resembling Complex C appear in simulated galaxies. Therefore, we conclude that HVCs appear to be a natural byproduct of galaxy formation in the ΛCDM Universe. Furthermore, we demonstrate that the models roughly reproduce the coverage of highly ionised HVCs with some reasonable assumptions. The next section describes our methodology, including a brief description of the simulations and how we "observe" the simulated disc galaxies. In Section 4.3, we present our results for both galaxies, looking at several ionisation species. We discuss our findings in Section 4.4.

4.2 Methodology

We analyse two disc galaxy models found in cosmological Smooth Particle Hydrodynamical (SPH) simulations. These simulations use a multi-mass technique, that self-consistently models the large-scale tidal field using low-resolution particles, but resimulates those particles that end up in the final galaxy at a higher resolution (Kawata et al., 2004). These simulations self-consistently include many of the important physical processes in galaxy formation, such as self-gravity, hydrodynamics, radiative cooling, star formation, SNe feedback, and metal enrichment. The disc galaxies we analyse correspond to "KGCD" and "AGCD" in Bailin et al. (2005), and we use these names hereafter. These are chosen on the basis of being disc-like $L_\star$ galaxies that are analogous to the MW. Both simulations are carried out with our galactic chemodynamics package GCD+ (Kawata & Gibson, 2003a).

The simulations are identical to those given in Bailin et al. (2005). The AGCD simulation uses the same initial conditions as the simulation of Abadi et al. (2003, kindly provided by Matthias Steinmetz), starting at redshift $z = 50$. The KGCD simulation is that of the "D1" simulation originally found in Kawata et al. (2004), simulated at higher resolution, starting at redshift $z = 43.5$. Essentially, initial conditions are created by small fluctuations being imposed on a CDM power spectrum using GRAFIC2 (Bertschinger, 2001). Table 4.1 summarises the simulation parameters and the properties of the resultant galaxies, including the galaxy name; their virial mass and radius ($M_{\rm vir}, r_{\rm vir}$); the radial extent of the gas disc ($r_{\rm disc}$, defined as the largest radius at which we find gas particles in the disc plane); the number of gas, DM and star particles within $r_{\rm vir}$ ($N_{\rm gas}, N_{\rm DM}, N_{\rm stars}$), the mass of each gas in the highest resolution region ($m_{\rm gas}$) and DM particle ($m_{\rm DM}$); the softening lengths of the gas in the highest resolution region ($\epsilon_{\rm gas}$) and DM ($\epsilon_{\rm DM}$), and the cosmological parameters (Ω_b, the baryon density fraction of the Universe; Ω_0, the matter density fraction of the Universe, and H_0, the Hubble constant). Note that the spatial resolution for the gas is determined by the smoothing length of the SPH scheme. The minimum smoothing length is set to be half of the softening length of the gas particles (Section 2.2.2). The smoothing length depends on the density, and the average smoothing length in the simulated HVCs we focus on here is $\sim 5\,$kpc.

Both galaxies were chosen to be resimulated at higher resolutions on the basis of them being similar in size and mass to the MW, and them having clear gas and stellar disc components (Bailin et al., 2005). Because of the cosmic variance

Table 4.1: The properties of the cosmological simulations.

Name	$M_{\rm vir}$	$r_{\rm vir}$	$r_{\rm disc}$	$N_{\rm gas}$	$N_{\rm DM}$	$N_{\rm stars}$	$m_{\rm gas}$	$m_{\rm DM}$	$\epsilon_{\rm gas}$	$\epsilon_{\rm DM}$	Ω_b	Ω_0	H_0
	($10^{12}\,{\rm M}_\odot$)	(kpc)					($10^6\,{\rm M}_\odot$)		(kpc)				${\rm km\,s^{-1}\,Mpc^{-1}}$
	(1)	(2)	(3)	(4)	(5)	(6)	(7)	(8)	(9)	(10)	(11)	(12)	(13)
KGCD	0.88	240	10	40188	158498	107349	0.92	6.2	0.57	1.1	0.039	0.3	70
AGCD	0.93	270	21	8600	52523	34774	3.3	19	0.87	1.5	0.045	0.3	65

Parameters: [1] final virial mass, [2] final virial radius, [3] final radial extent of the gas disc, [4] final number of gas particles, [5] final number of DM particles, [6] final number of star particles, [7] mass of each gas disc (highest-resolution) particle, [8] mass of each DM particle, [9] softening length of each gas disc (highest-resolution) particle, [10] softening length of each DM particle, [11] baryon density fraction of the Universe, [12] matter density fraction of the Universe, and [13] Hubble constant.

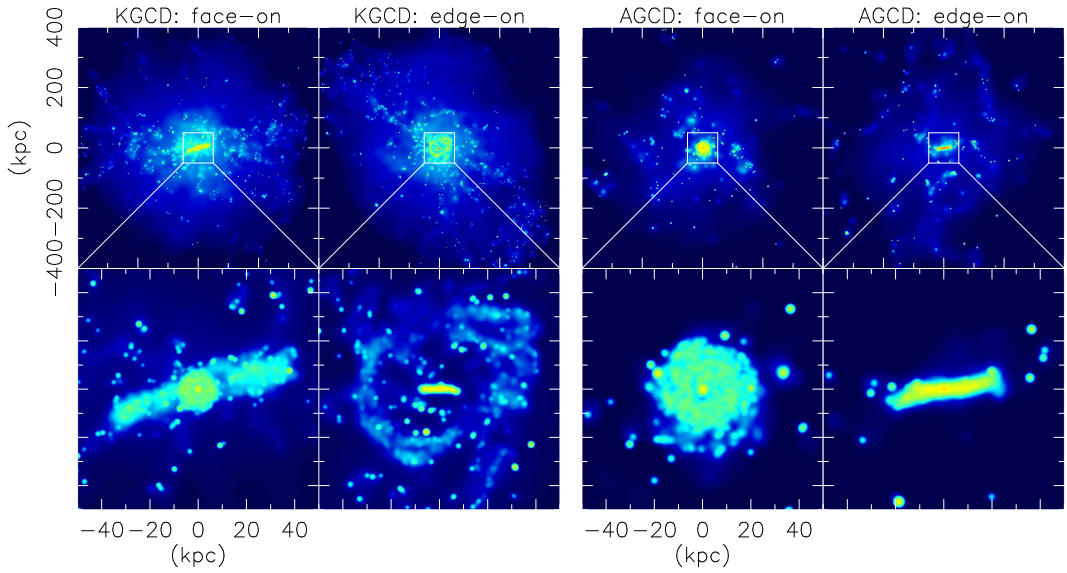

Figure 4.1: H I gas column density maps of KGCD (left set of 4 panels) and AGCD (right set) simulations.

principle, we expect predictions from any set of models to show some variance to the MW. Unlike Kravtsov et al. (2002), we do not constrain the initial conditions to generate an exact match to the Local Supercluster, instead opting to compare against more generic $L_\star$ galaxies to see whether HVCs are a universal phenomenon. Figure 4.1 shows edge-on and face-on views of the projected gas density of each galaxy at the final timestep. We use the simulation output at $z = 0.1$ for KGCD (with a lookback time of 1.2 Gyr), as contamination from low-resolution particles in the simulated galaxy start to become significant after this redshift. This does not affect our conclusions, as the features we observe are found in all timesteps at late times. We use the output at $z = 0$ for AGCD.

In order to compare the simulations with the HVC observations in the MW, we project the simulation (removing the Hubble-flow and orienting the disc so it rotates with the same sense as the MW) from the vantage point of a "virtual observer" to an arbitrary position on the disc plane of the simulated galaxies, with galactocentric distance of 8.5 kpc, and "observe" the H I column density and velocity of the gas particles from that position. We confirm that both simulated galaxies have gas discs rotating at $\sim 220\,\mathrm{km\,s^{-1}}$, and hence set the rotation velocity of the Local Standard of Rest (LSR) to $220\,\mathrm{km\,s^{-1}}$, similar to that of the MW (Lockman et al., 2002). We define HVCs as consisting of gas particles with absolute lines-of-sight velocities, v_{LSR}, deviating from the LSR by more than $100\,\mathrm{km\,s^{-1}}$. Herein, the results are based only

on those particles within 4.5 virial radii ($r_{\rm vir}$; see Table 4.1). We have confirmed that the results are not sensitive to the cutoff radius chosen for column densities $N(\mathrm{HI}) \gtrsim 10^{17}\,\mathrm{cm}^{-2}$. We only display results for one chosen observer, however we demonstrate the generality of these results, with the sky coverage fraction typically changing by no more than 20% for a given column density, as we change the observer's position. A similar outcome is observed as we analyse other outputs of the simulations near the final redshift.

Our chemodynamical simulation follows the hydrogen and other elemental abundances for each gas particle, but does not calculate the ionisation fraction of each species. Instead, the H I mass for each gas particle is calculated assuming a simple collisional ionisation equilibrium (CIE) model. The CIE neutral hydrogen fraction is estimated using Cloudy94 (Ferland et al., 1998; see also Section 2.2.7). We neglect shock heating, heat conduction, and the photoionisation effects resulting from UV radiation leaking from the Galactic disc (the latter effects should not affect the O VI predictions; Sembach et al., 2003). These assumptions enable us to simply obtain the ionisation fraction as a function of temperature, combined with the elemental ratios within each particle in the simulation, to obtain species mass fractions of each particle.

It might be expected that the clouds in the simulations may be destroyed by effects that our simulations are not able to reproduce accurately. The resolution and nature of the SPH simulations make it more difficult to resolve shocks between the HVCs and the MW halo compared to Eulerian codes (Agertz et al., 2007); however the HVCs in our simulations are mostly subsonic due to the low density of the halo, and thus there will not be strong shocking of the HVCs. Any slight heating that might occur is further expected to be offset by the cooling that would result from the ionised gas in the shock front. Indebetouw & Shull (2004), using more detailed simulations, argue that the Mach number of the HVCs are only $M_s \sim 1.2 - 1.5$, marginally sufficient to form shocks, and heating the leading $\sim 0.1\,\mathrm{pc}$ of the HVC. Quilis & Moore (2001) show that the lifetime of such HVCs in the presence of shocks is $\sim 1\,\mathrm{Gyr}$, long enough for our HVCs to survive. Maller & Bullock (2004) discuss various physical processes, including conduction, evaporation, ram-pressure drag, Jeans instabilities, and Kelvin–Helmholtz instabilities that limit the mass ranges of stable clouds. The most massive HVC apparent in our simulations is found to be $1.5 \times 10^8\,\mathrm{M}_\odot$, and the mass resolution and hence smallest resolvable HVC in our simulations are $\sim 10^6\,\mathrm{M}_\odot$; clouds of both extremes are clearly within the stable mass

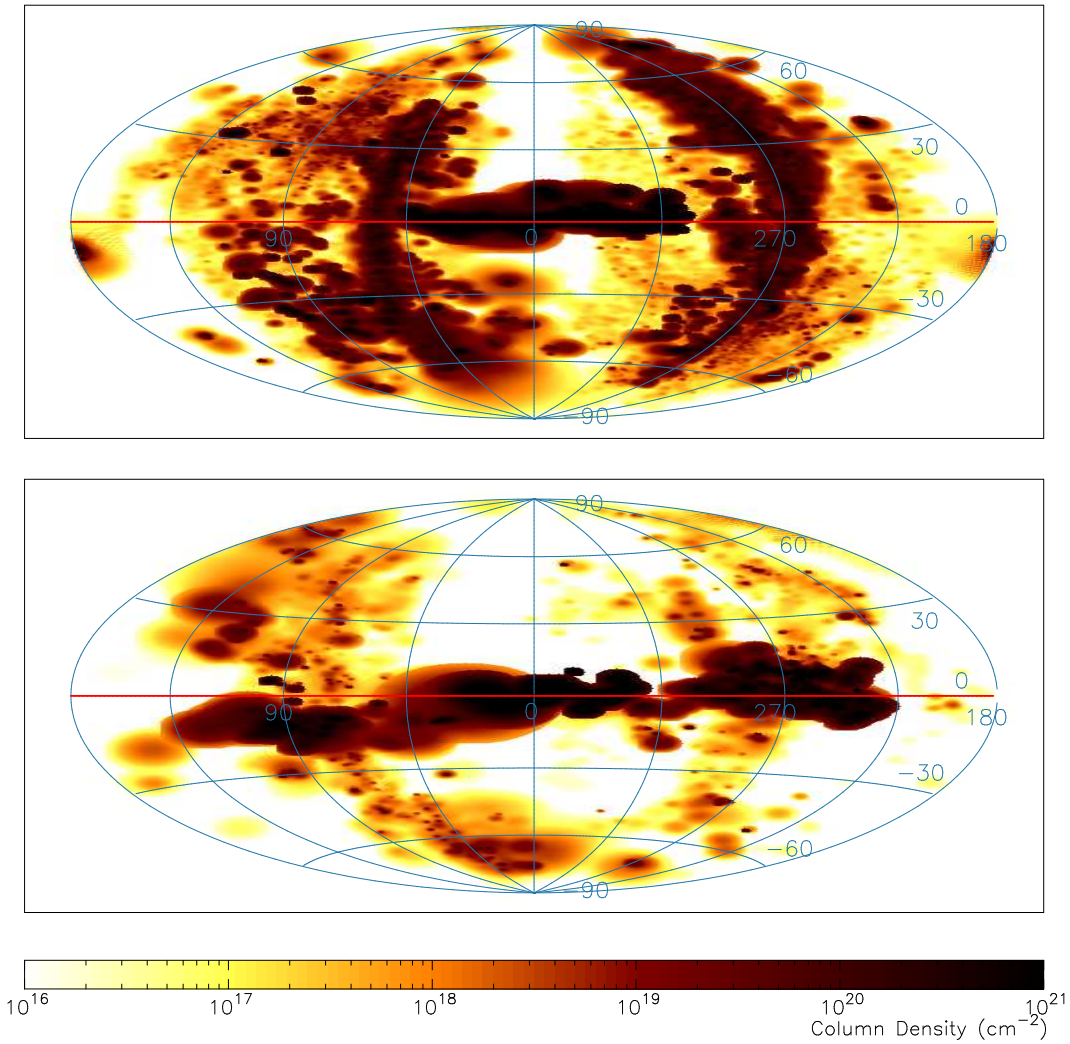

Figure 4.2: H I column density maps of KGCD (top) and AGCD (bottom) simulations, using an all-sky Hammer-Aitoff projection in galactic coordinates. Particles with $|v_{\rm LSR}| < 100\,{\rm km\,s^{-1}}$ are excluded. Compare these maps with fig. 2 in Wakker (1991).

ranges summarised in fig. 6 of Maller & Bullock (2004). Therefore, the simulated clouds are also expected to be stable.

4.3 Results

4.3.1 H I HVC Distributions

The all-sky figures in Figure 4.2 demonstrate that both galaxies have a significant number of HVCs with $|v_{\rm LSR}| > 100\,{\rm km\,s^{-1}}$, with column density distributions above $10^{18}\,{\rm cm^{-2}}$ comparable to those observed by Wakker (1991). The KGCD simulation

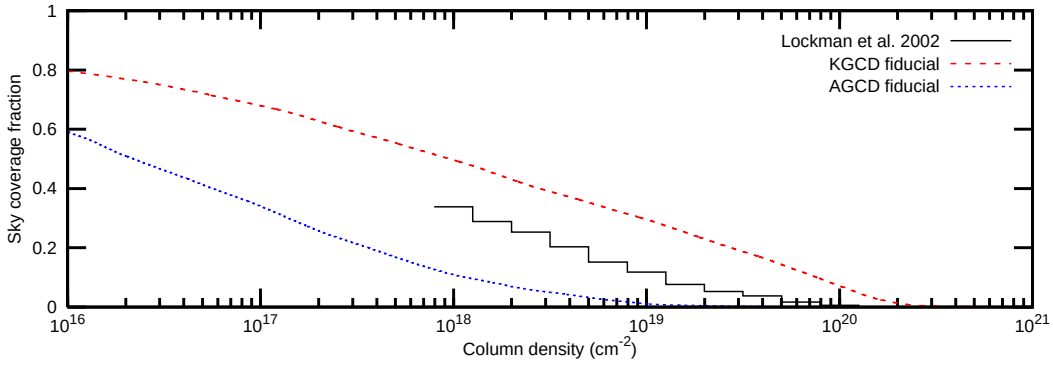

Figure 4.3: H I sky coverage fraction vs. limiting column density for the "fiducial" observer examined in the bulk of this chapter. The histogram denotes the sky coverage fraction from the Lockman et al. (2002) HVC survey (which excludes $|v_{\rm LSR}| \lesssim 100\,{\rm km\,s^{-1}}$, and $|b| \lesssim 20°$) to the 4σ completeness limit. From the point of view of the fiducial observer (at an arbitrary location on the disc, 8.5 kpc from the respective galactic centres), the sky coverage fraction obtained from the KGCD simulation is shown as a red dashed line, and the blue dotted line denotes the AGCD simulation.

displays several large linear HVCs at galactic longitudes $l \sim 60°$ and $l \sim 270°$. These components correspond to the outer ring structure seen at a galactocentric radius of $\sim 30\,{\rm kpc}$ in Figure 4.1. We name this structure the "polar gas ring", and discuss it later.

To compare the HVC population of our simulations with the MW HVCs quantitatively, Figure 4.3 shows the fraction of sky covered by HVCs as a function of limiting column density for both simulations and for the observations in Lockman et al. (2002). In this plot, we exclude the area with low galactic latitude $|b| < 20°$, to avoid contamination by the disc component (the sample of sightlines in Lockman et al., 2002 was limited in a similar fashion). As is obvious from Figure 4.2, KGCD has more extensive high column density HVCs than AGCD, and almost all of the sky is covered down to $10^{16}\,{\rm cm^{-2}}$. At a fixed column density, the sky coverage in the simulations bracket the observed sky coverage in the MW. To verify that differing observers within the galaxy discs see similar populations of HVCs, Figure 4.4 demonstrates that the sky coverage fraction typically changes between observers by no more than 20% for a given column density.

In the simulations, we are able to measure the distance of HVCs—data which are not yet generally available for the real MW HVCs. In Figure 4.5, we show a flux-weighted histogram of the galactocentric distances, r, of the high velocity gas particles with $|b| > 20°$. In both simulations, less than 1% of the H I flux visible in Figure 4.2 originates from HVCs with $r > 150\,{\rm kpc}$ (in AGCD, the bulk of this

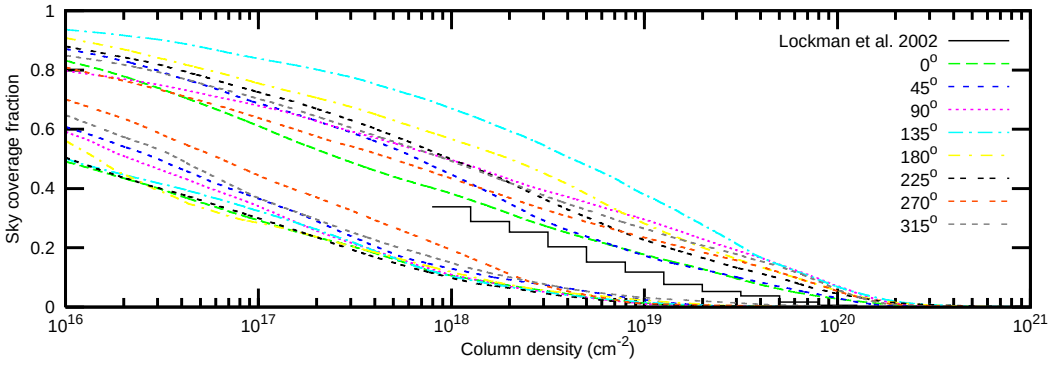

Figure 4.4: As in Figure 4.3, the H I sky coverage fraction vs. limiting column density, but for varying observers. The observer is chosen in increments of 45° around the disc plane, with all of them remaining 8.5 kpc from the galactic centre. The top set of lines corresponds to the KGCD simulation, and the bottom set to the AGCD simulation.

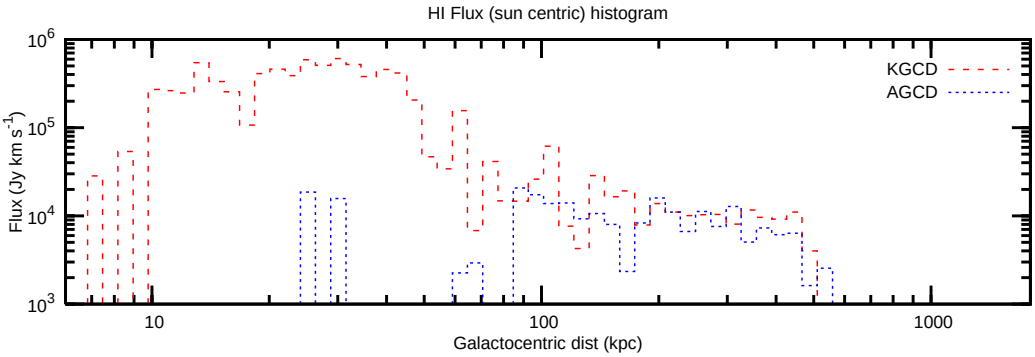

Figure 4.5: H I flux weighted histogram with logarithmically spaced bins in distance (de-emphasing fluxes from smaller galactocentric distances) of both AGCD and KGCD simulations, excluding $|v_{\rm LSR}| < 100\,{\rm km\,s^{-1}}$ and $|b| < 20°$.

emission comes from the disc, and excluding the disc between $-20° < b < 20°$ results in only half of the emission coming from distances closer than 150 kpc). For KGCD, this is consistent with the aforementioned limits established by Pisano et al. (2004). It is also clear that most of the non-disc emission in the KGCD simulation results from the polar gas ring, whose radius is ~ 30 kpc. The mass of this ring (including low velocity gas) is $3.6 \times 10^9\,{\rm M}_\odot$, of which $2.3 \times 10^9\,{\rm M}_\odot$ is H I. Although there is no prominent polar ring in AGCD, at larger distances, the flux distribution is found to follow that of the KGCD simulation.

Figure 4.2 demonstrates that the polar gas ring seen in KGCD forms a linear high velocity structure found in all quadrants of the sky. Large HVC components, such as Complex C and the MS, are well known in our MW, and several authors

(e.g. Mathewson et al., 1987; Haud, 1988) argue that the MW is surrounded by a polar gas ring. Neglecting the MS, which has likely originated from the infalling MCs (GN96; YN03; see also Chapter 3), the largest HVC structure is Complex C. We measure the H I mass of the HVC ring in one quadrant as $\sim 4 \times 10^8\,\mathrm{M}_\odot$. If we place Complex C at a distance of 10 kpc, its H I mass would be $\sim\ 5 \times 10^6\,\mathrm{M}_\odot$ (Thom et al., 2007). Nevertheless, this indicates that there is more than enough H I gas to create such large observed HVCs in the simulated galaxy. In KGCD, the polar gas ring is a relatively recently formed structure that begins forming at redshift $z \sim 0.2$ (i.e., 1 Gyr before the simulation is terminated at $z = 0.1$), and prior to this time, the associated gas particles are found flowing inward along filamentary structures. Thus, this simulated ring structure demonstrates that current ΛCDM numerical simulations can explain the existence of such large HVCs like Complex C as recently accreted gas which rotates in a near-polar orbit. On the other hand, AGCD does not show such a prominent large structure. This may indicate that such HVC structures are not common in all disc galaxies.

Note that we ignore any effects of background radiation on the gas. It is expected that such a field would decrease the population of HVCs with galactocentric distance less than 10 kpc or $N(\mathrm{HI}) \lesssim 10^{19}\,\mathrm{cm}^{-2}$ (Maloney, 1993; Bland-Hawthorn & Maloney, 1997, 1999). Thus, since the distances of the simulated HVCs are greater than 10 kpc, our estimated coverage fractions in Figure 4.3 should be interpreted as upper limits for $N(\mathrm{HI}) \lesssim 10^{19}\,\mathrm{cm}^{-2}$ and lower limits for $N(\mathrm{HI}) \gtrsim 10^{19}\,\mathrm{cm}^{-2}$, where the highest column density HVCs may not be fully resolved. With these caveats, KGCD appears to have a sufficient population of HVCs to explain the observed population of HVCs within the MW. The differences between KGCD, AGCD and the MW may demonstrate real differences in the populations of HVCs among disc galaxies.

We can compare the HVCs seen in the first moment maps of Figure 4.6 with fig. 16 of Wakker et al. (2003), and the distributions in Putman et al. (2002). Overall, the clouds between $l = 0°$ and 180° have a negative velocity, while the clouds between $l = 180°$ and 360° have a positive velocity. This is natural, since the LSR is moving towards $l = 90°$. In KGCD, we find that there is a relatively large HVC complex whose velocity is very high, $-450 \lesssim v_{\mathrm{LSR}} \lesssim -300\,\mathrm{km\,s}^{-1}$. These Very High Velocity Clouds (VHVCs) are located between $-45° \lesssim b \lesssim 15°$ and $60° \lesssim l \lesssim 120°$, in the top panel of Figure 4.6. The MW also has such VHVCs in the Anti-Centre complex (Hulsbosch, 1978; Hulsbosch & Wakker, 1988). The galactocentric distance to the VHVC in KGCD is $\sim 10-25$ kpc and we find that the cloud is a gas clump which has

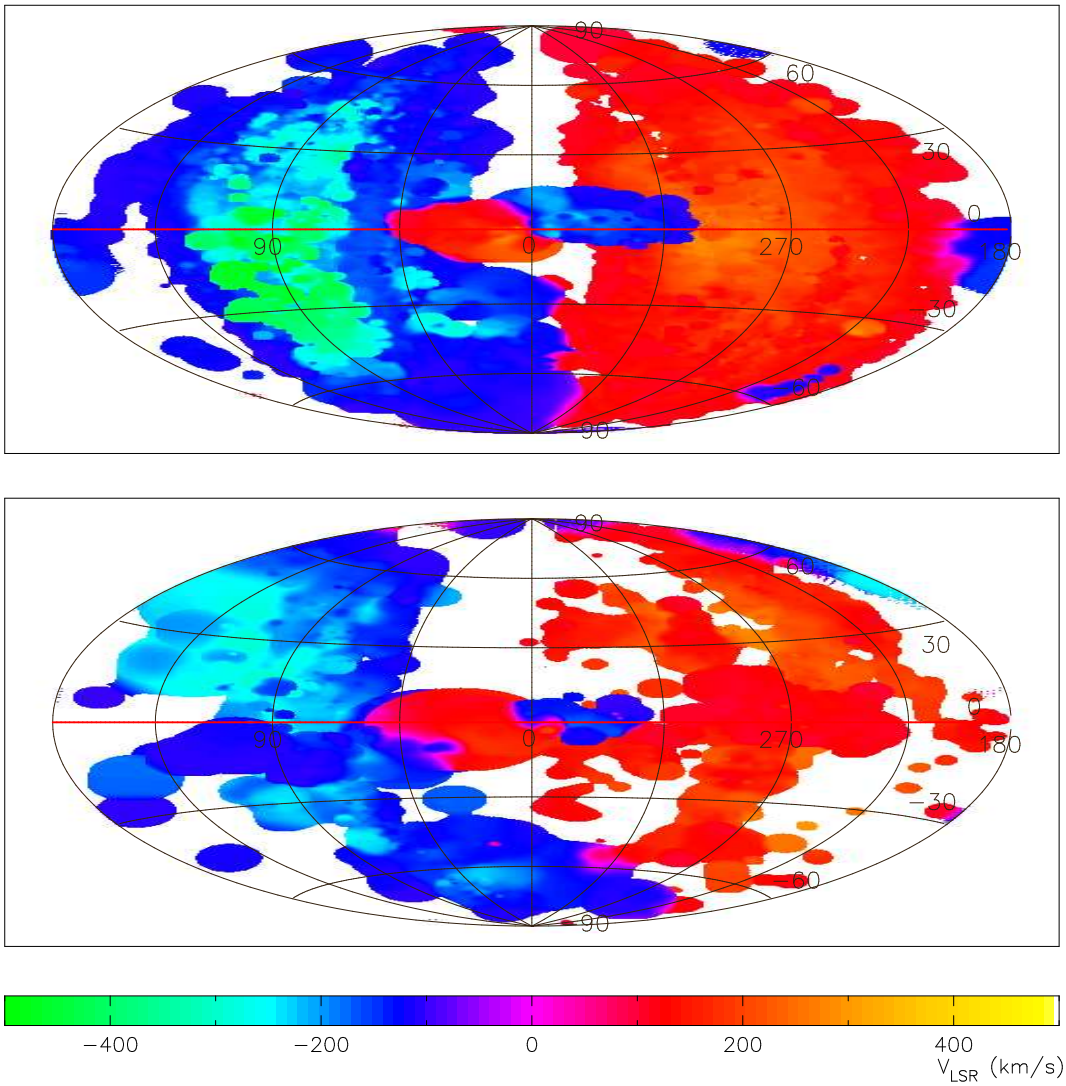

Figure 4.6: H I first moment map of KGCD (top) and AGCD (bottom) simulations. The first moment is that of the mean velocity in the LSR, $v_{\rm LSR}$, weighted by column density. Particles with $|v_{\rm LSR}| < 100\,{\rm km\,s^{-1}}$ are excluded. Compare these maps with fig. 16 in Wakker et al. (2003).

recently fallen into the galaxy. We convert the H I mass for each particle into a H I flux using $M_{\rm HI} = 0.235 D_{\rm kpc}^2 S_{\rm tot}$ (Wakker & van Woerden, 1991), where the H I mass $M_{\rm HI}$ is in $\rm M_\odot$, total H I flux in Jy km s^{-1} is $S_{\rm tot}$, and distance from observer to the particle in kpc is $D_{\rm kpc}$. We find the H I mass of the VHVC complex is $1.2 \times 10^8\,\rm M_\odot$, and the total H I flux (for the chosen observer) is 2.5×10^6 Jy km s^{-1}.

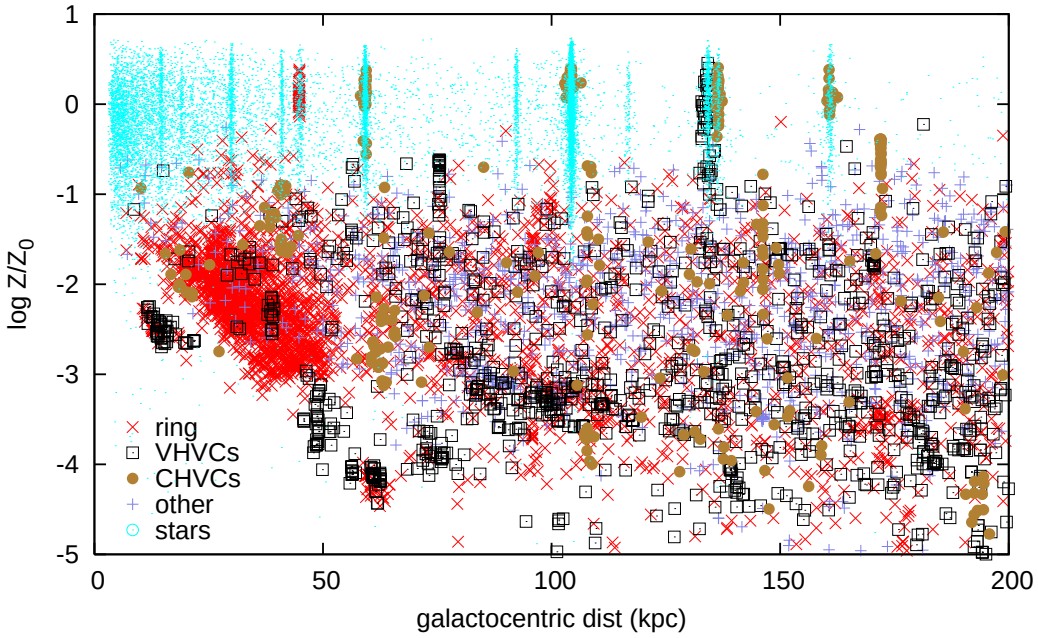

Figure 4.7: Metallicity ($\log \mathrm{Z/Z_\odot}$) of gas and stars with $|v_{\mathrm{LSR}}| > 100\,\mathrm{km\,s^{-1}}$ in the KGCD simulation. The gas has been tagged on whether it spatially appears to be in the polar gas ring, in compact high column density clumps, the significant VHVC complexes, or elsewhere. No kinematical or distance information has been used in this tagging.

4.3.2 Metal Distributions

We analyse the metallicity of the simulated HVCs. Since the abundance profiles of the AGCD and KGCD simulations are largely consistent with each other, we focus here on the KGCD simulation in greater detail. Looking at its H I distribution, the gas is tagged on whether it spatially appears to be in the polar gas ring, in compact high column density clumps, the significant VHVC complexes, or elsewhere. In order to mimic the limitations of the observations, distance information is not used in the tagging process, and as such, particles further out can be erroneously catalogued as ring particles. Figure 4.7 displays the metallicities of the star particles and particles in these various gas components in KGCD with $|v_{\mathrm{LSR}}| > 100\,\mathrm{km\,s^{-1}}$. For KGCD, we also produce a metallicity moment map in Figure 4.8 of all gas, including the disc. In KGCD we find that the prominent HVCs, such as the VHVC, have H I flux weighted metallicities of $-4 \lesssim \log(\mathrm{Z/Z_\odot}) \lesssim -2$ with a flux weighted mean of $\log(\mathrm{Z/Z_\odot}) \sim -2.4$. This is much lower than the metallicities of the observed HVCs in the MW, $-1 < \log(\mathrm{Z/Z_\odot}) < 0$ (Wakker, 2001). The polar gas ring seen in KGCD has a metallicity of $-3 \lesssim \log(\mathrm{Z/Z_\odot}) \lesssim 0.5$ with a mean of $\log(\mathrm{Z/Z_\odot}) \sim -1.7$,

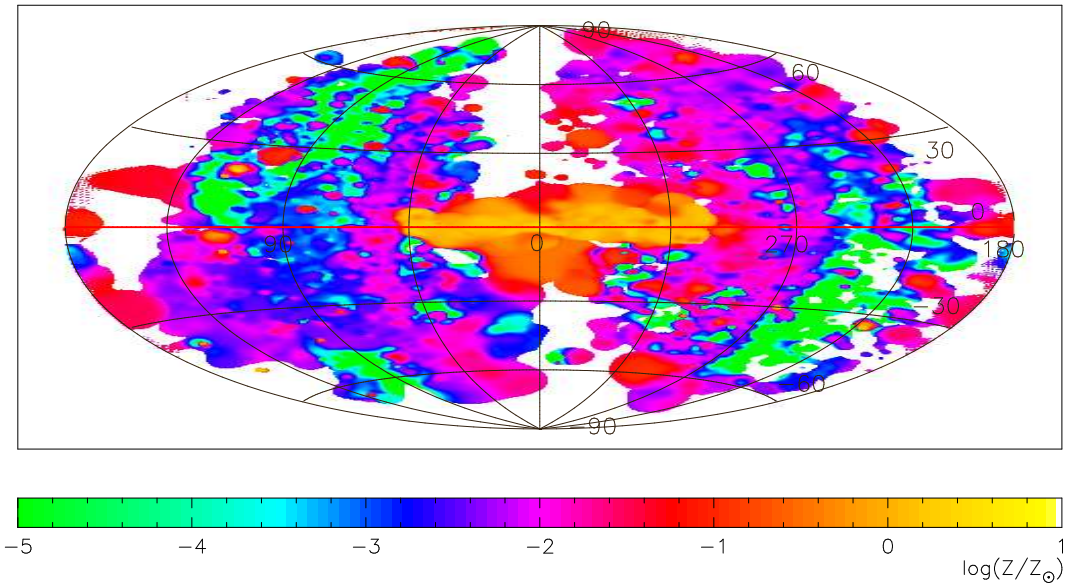

Figure 4.8: Moment map of mass weighted metallicity ($\log \mathrm{Z/Z_\odot}$) of gas with $|v_{\mathrm{LSR}}| > 100\,\mathrm{km\,s^{-1}}$ in the KGCD simulation.

which is lower than the observed metallicity of Complex C, $\log(\mathrm{Z/Z_\odot}) \sim -1$ (e.g. Gibson et al., 2001; Richter et al., 2001). Thus, our numerical simulations seem to underestimate the metallicity of the later infalling gas clouds. This is likely because we adopt a weak SNe feedback model in our simulations, with 10^{50} erg available per SN (Kawata & Gibson, 2003b; Kawata et al., 2004). If we were to use a model with strong feedback, more enriched gas would be blown out from the system at high redshifts, enriching the inter-galactic medium which then falls into galaxies at a later epoch. Despite not reproducing the absolute metallicities, our models are clearly able to discriminate between the different types of HVC structures by their chemical signatures, with newly infalling clouds such as the VHVCs being lower in metallicity. Thus we expect observations of the chemical makeup of the various HVCs will prove useful in the future.

4.3.3 O VI HVC Distributions

The simulated sky is found to be more uniformly covered in O VI than in H I, with O VI not forming large linear structures. In Figure 4.9, the zeroth (flux) and first (v_{LSR}) moment maps of O VI, excluding $|v_{\mathrm{LSR}}| < 100\,\mathrm{km\,s^{-1}}$, are displayed for the KGCD model. The O VI is similar, kinematically, to the H I in Figure 4.6. Sembach et al. (2003) and Wakker et al. (2003) contain the corresponding observations,

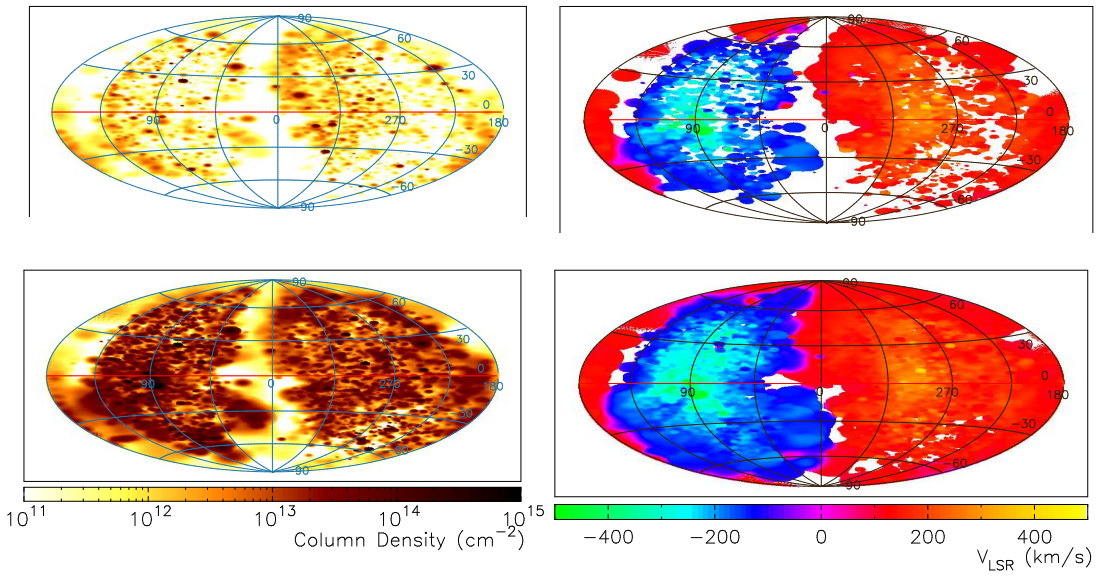

Figure 4.9: All-sky column density (left) and first moment ($v_{\rm LSR}$; right) maps of KGCD simulation in O VI. The top row shows the oxygen content unconstrained, and the bottom row shows the oxygen content for the assumption of a minimum oxygen abundance of [O/H] = −0.5. Particles with $|v_{\rm LSR}| < 100\,{\rm km\,s^{-1}}$ are excluded. Compare these maps with figs. 6 and 11 in Sembach et al. (2003).

which show similar kinematic behaviour, but only have sparse spatial coverage of data. From Figure 4.10, displaying the temperature of particles and hence their O VI ionisation fractions with galactocentric distance, and Figure 4.11 showing the distribution of distances to O VI flux, we find the particles rich in O VI are distributed throughout the hot halo from $\sim 100 - 500\,{\rm kpc}$.

The column density for a given sky coverage in KGCD and AGCD is two orders of magnitude below that observed. In Figure 4.12, the left most curves are the modelled sky coverage as a function of limiting column density for O VI. Sembach et al. (2003) show that 60 – 85% of the sky is covered down to $\sim 10^{13}\,{\rm cm^{-2}}$. We find however, that the mass weighted mean of oxygen abundance, [O/H] is ~ -1.75 for most of the gas responsible for the O VI emission (see also Figures 4.10 and 4.7). If we force the gas to adopt a minimum oxygen abundance of [O/H] = −0.5 (generating the bottom plots in the O VI maps in Figure 4.9 and right curves in the sky coverage fractions in Figure 4.12), similar to the oxygen abundance of HVCs in the MW (Collins et al., 2007), then we can increase the sky coverage fraction somewhat, but not enough to reproduce the observations. This may point to inadequacies of our SNe feedback model in generating heavier elements, as well as possible problems in adequately ionising these hot clouds because of the lack of UV background.

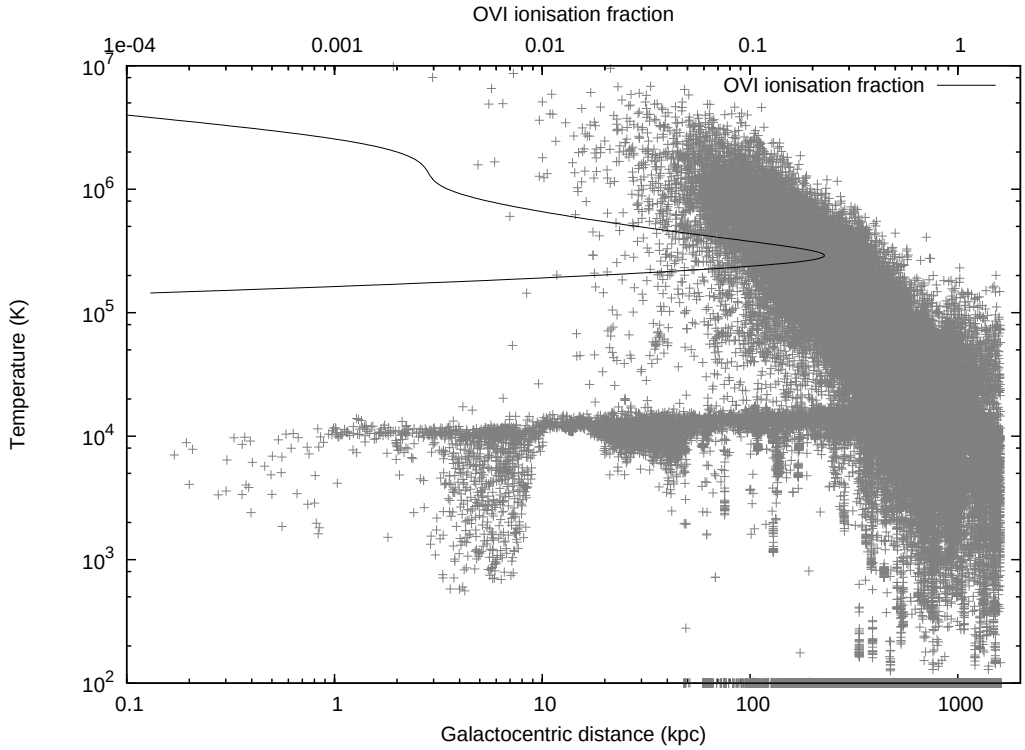

Figure 4.10: Temperature of all gas particles in the KGCD simulation, with O VI ionisation fraction superimposed, illustrating where gas abundant in O VI is likely to be found.

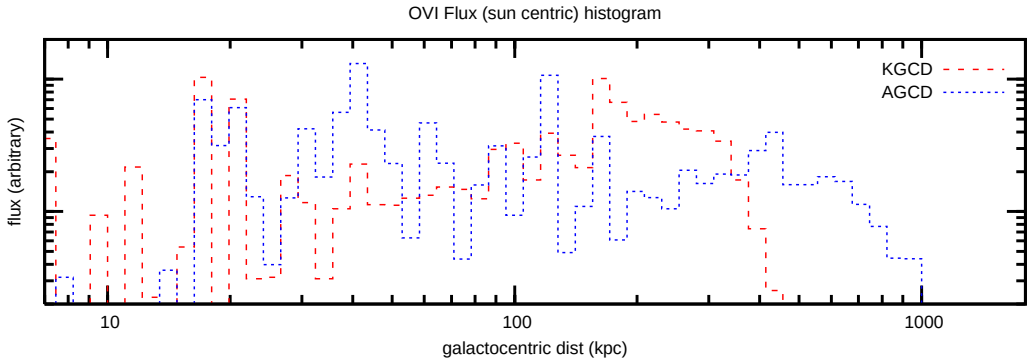

Figure 4.11: O VI flux weighted histogram with logarithmically spaced bins in distance (de-emphasing fluxes from smaller galactocentric distances) of both AGCD and KGCD simulations, excluding $|v_{\rm LSR}| < 100\,{\rm km\,s^{-1}}$ and $|b| < 20°$.

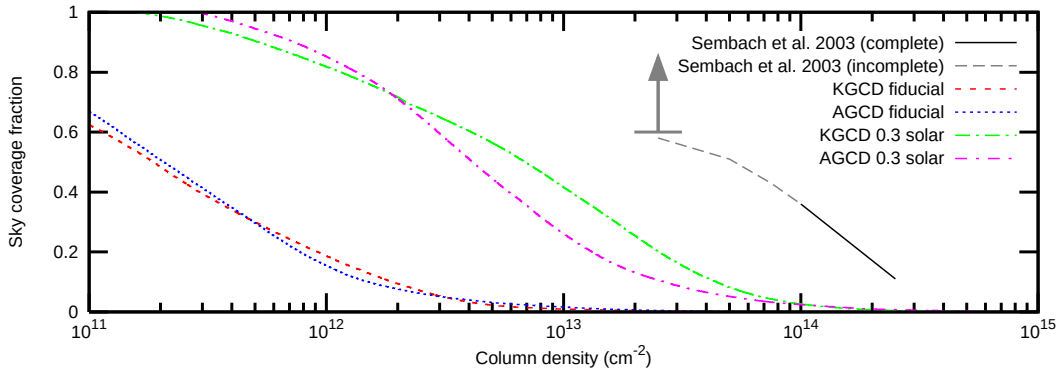

Figure 4.12: O VI sky coverage fraction vs. limiting column density. The solid black line denotes the sky coverage fraction obtained from the Sembach et al. (2003) survey (which excludes $|v_{\rm LSR}| \lesssim 100\,{\rm km\,s^{-1}}$, and $|b| \lesssim 20°$), and its dashed extension shows the lower limit obtained from the same survey for the lower quality data, along with its uncertainty. The sky coverage fraction (excluding $|b| < 20°$) of O VI with $|v_{\rm LSR}| > 100\,{\rm km\,s^{-1}}$, obtained from the KGCD simulation, is shown as a red dashed line, or assuming a minimum oxygen abundance of [O/H] = −0.5, a green dot dashed line. Blue dotted and magenta dot dashed lines similarly denote the AGCD simulations.

4.3.4 H II, C IV and O VII HVC Distributions

Observations of elemental species other than O VI are not yet complete enough to obtain sky coverage fractions, however Figure 4.13 shows the zeroth (flux) and first ($v_{\rm LSR}$) moment maps of H II, C IV and O VII for KGCD. From these, we obtain sky coverage fractions for H II in Figure 4.14, C IV in Figure 4.15 and O VII in Figure 4.16. Sembach et al. (2003) indirectly obtain an estimate of a 60% (but up to 85%) sky coverage fraction of H II at $1.15 \times 10^{18}\,{\rm cm^{-2}}$, assuming the hot high velocity gas has an oxygen abundance similar to the Magellanic Stream of [O/H] = −0.7. This agrees well with our predictions. However, our modelling of O VII suffers from the same poor sky coverage as our modelling of O VI. Boosting the oxygen abundance to a minimum of [O/H] = −0.5 has a similar effect as it did for O VI, of improving the reproduction of observations somewhat.

4.3.5 Stellar and Dark Matter Association

Figure 4.17 plots the surface density of the gas, stars and DM, and demonstrates that the majority of the simulated HVCs, including the polar gas ring and VHVCs in KGCD, do not have any obviously associated stellar or DM components, which is consistent with current observations (Simon & Blitz, 2002; Siegel et al., 2005). The VHVC at $l \sim 90°$, for example, can only be seen as a gas over-density and is not seen

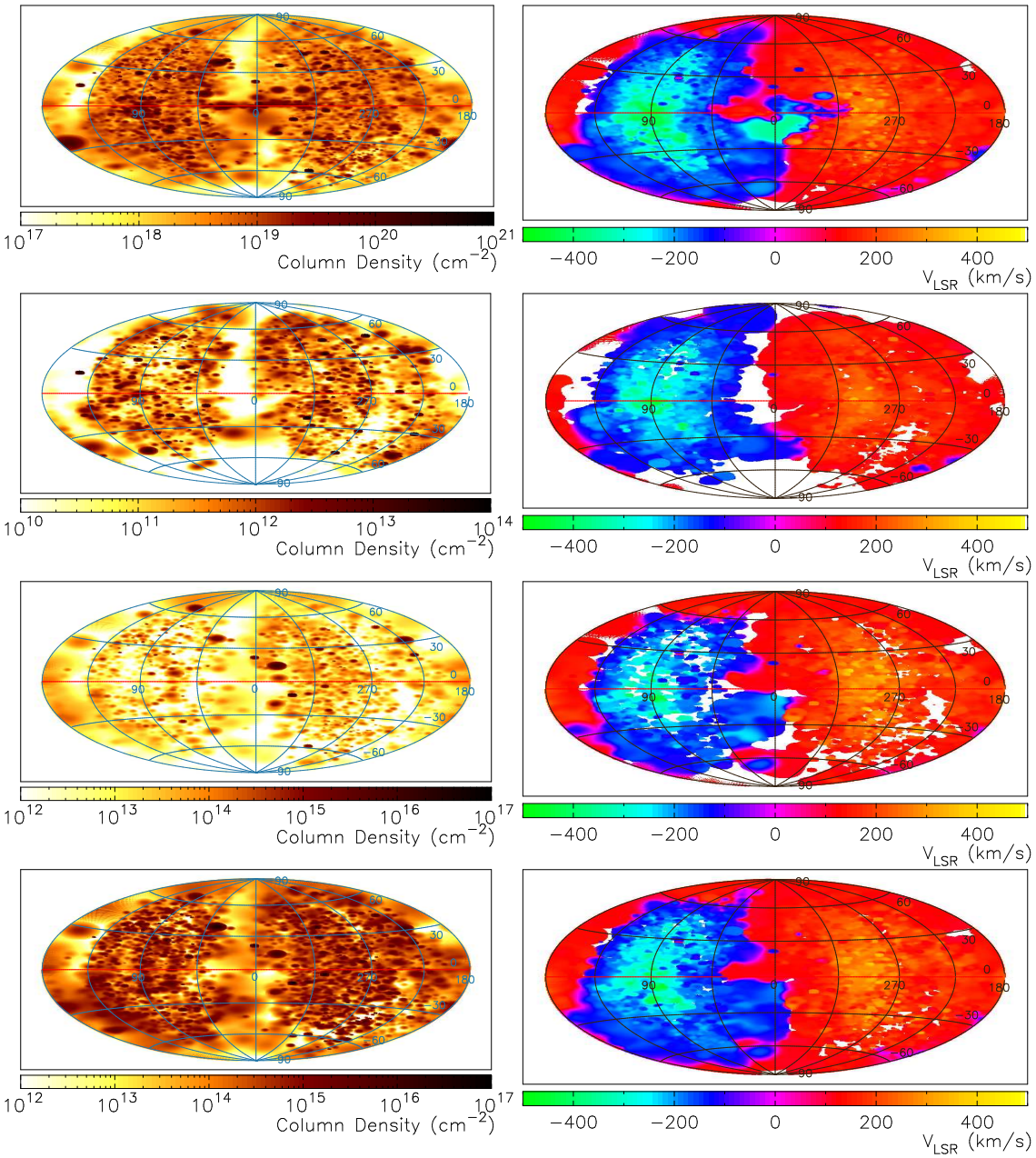

Figure 4.13: All-sky column density (left) and first moment (v_{LSR}; right) maps of KGCD simulation in H II (top row), C IV (second row) and O VII (third and fourth rows). The third row shows the oxygen content unconstrained, and the bottom row shows the oxygen content for the assumption of a minimum oxygen abundance of [O/H] $= -0.5$. Particles with $|v_{\mathrm{LSR}}| < 100\,\mathrm{km\,s^{-1}}$ are excluded.

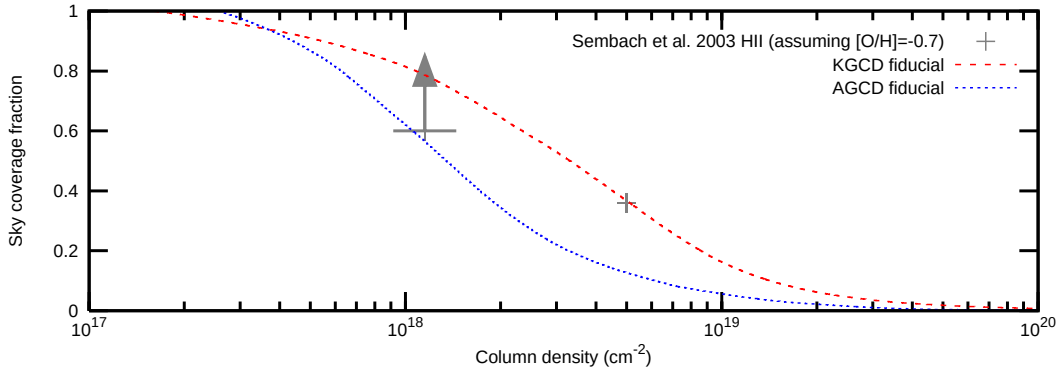

Figure 4.14: H II sky coverage fraction vs. limiting column density. The sky coverage fraction (excluding $|b| < 20°$) of H II with $|v_{\rm LSR}| > 100\,{\rm km\,s^{-1}}$, obtained from the KGCD simulation, is shown as a red dashed line. A blue dotted line denotes the AGCD simulations. Sembach et al. (2003) estimate that 60 – 85% of the sky is covered by H II down to $\sim 10^{18}\,{\rm cm^{-2}}$, if the hot high velocity gas has an oxygen abundance similar to the Magellanic Stream of [O/H] = −0.7.

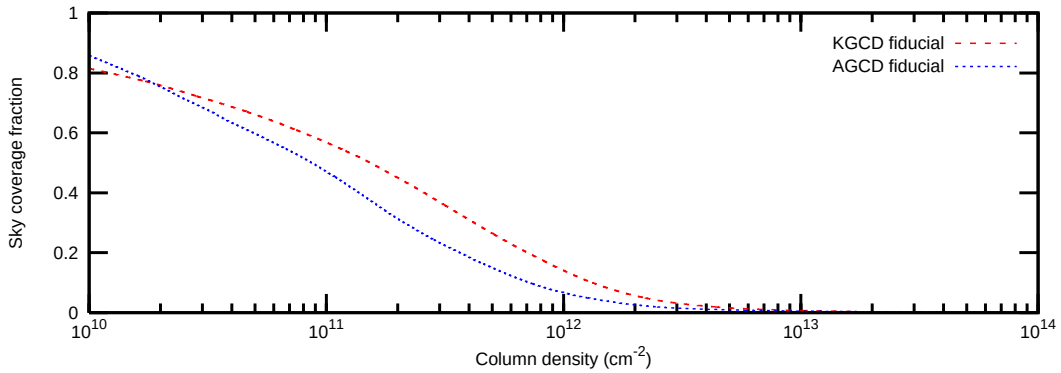

Figure 4.15: C IV sky coverage fraction vs. limiting column density. The sky coverage fraction (excluding $|b| < 20°$) of C IV with $|v_{\rm LSR}| > 100\,{\rm km\,s^{-1}}$, obtained from the KGCD simulation, is shown as a red dashed line. A blue dotted line denotes the AGCD simulations.

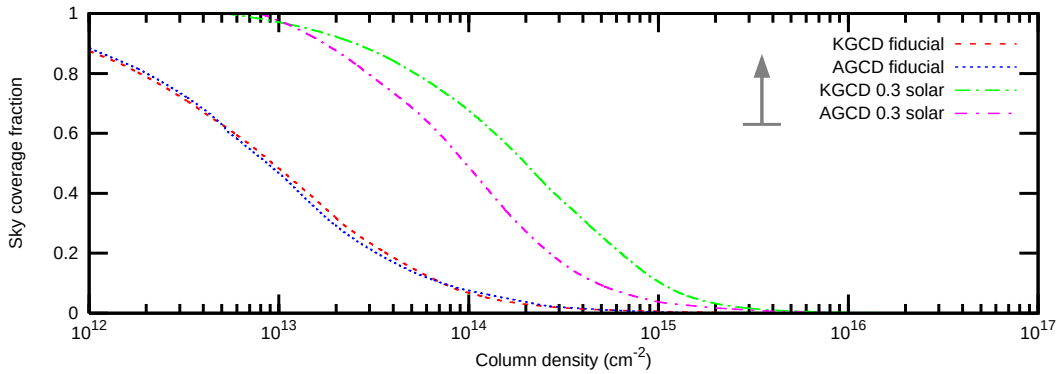

Figure 4.16: O VII sky coverage fraction vs. limiting column density. The sky coverage fraction (excluding $|b| < 20°$) of O VII with $|v_{\rm LSR}| > 100\,{\rm km\,s^{-1}}$, obtained from the KGCD simulation, is shown as a red dashed line, or assuming a minimum oxygen abundance of [O/H] = −0.5, a green dot dashed line. Blue dotted and magenta dot dashed lines similarly denote the AGCD simulations.

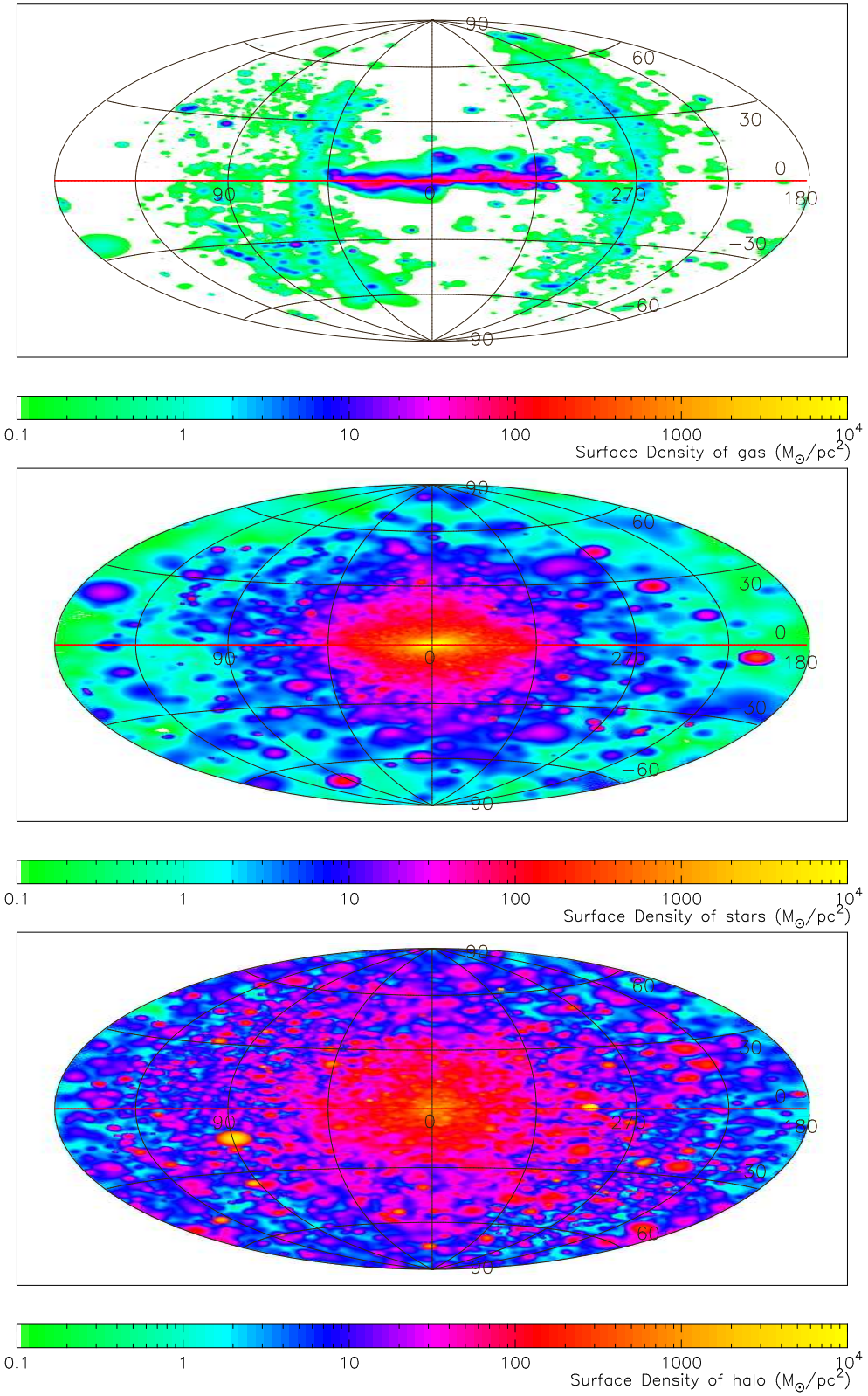

Figure 4.17: Density of all gas (top), stars (middle) and halo DM (bottom) material with $|v_{\rm LSR}| > 100\,{\rm km\,s^{-1}}$, in the KGCD simulation.

in the other components. However, we find from Figure 4.7 that a few (but not all) CHVCs further out are found to be associated with stellar components. It would be interesting to estimate the luminosity of these stellar systems, and if they are detectable within the current observational limits. Unfortunately, the resolution of the current simulations are too poor to estimate the luminosity, and it is also likely that our simulations produce too many stars due to our assumed minimal effect of SNe feedback.

4.4 Conclusion

We report that HVCs, decoupled from any stellar or DM counterpart, seem to be a natural occurrence in a ΛCDM Universe. We emphasise that the galaxies that result from our simulations were not created specifically to reproduce the MW exactly—they were selected for resimulation at higher resolution on the basis of being disc-like, $L_\star$ galaxies with luminosity and mass of the order of the MW's. We thus expect some variance from the MW simply through cosmic variance. However, via self-consistent cosmological simulations, we recover many of the properties of anomalous velocity features that are seen within the MW. At the termination of the simulations near the current time (redshift $z = 0.1$ and $z = 0$ in KGCD and AGCD respectively), we have two $L_\star$ galaxies with rotation curves and masses similar to the MW, with large-scale linear features in H I with anomalous velocities. Their H I column densities are within an order of magnitude of HVCs found in the MW by Lockman et al. (2002), and they have a similar velocity distribution to those catalogued by Putman et al. (2002). The resultant H I HVCs have locations that are consistent with observational limits currently known (Danly et al., 1993; van Woerden et al., 1999; Wakker, 2001; Pisano et al., 2004; Thilker et al., 2004; Westmeier et al., 2005a; Thom et al., 2006; Wakker et al., 2007; Thom et al., 2007; Wakker et al., 2008) for other galaxies. This gas is local to the simulated galaxies, with 99% and 50% of high velocity, non-disc H I flux originating from closer than 150 kpc in KGCD and AGCD respectively. Furthermore, from the vantage point of an artificial Sun, we find that the entire sky is covered in H I down to the arbitrary fluxes that the simulation can probe. The sky coverage fraction, as a function of limiting column density, is found to follow similar trends as the HVCs within our own Galaxy, up to the limit that can be probed by observations. The simulations reproduce the different populations of HVCs, with

large complexes like Complex C, that could be explained as a portion of a ring rotating in a near polar orbit, VHVCs, and CHVCs.

We have also shown that anomalous velocity O VI clouds share similar properties to those observed with the new observational data from FUSE (Sembach et al., 2003). We find there exists ionised anomalous velocity clouds that constitute a hot halo extended from ~ 100 kpc to ~ 500 kpc. O VI clouds are found to be distributed isotropically with 70% and 50% of the flux originating from further than 100 kpc in KGCD and AGCD respectively. The flux weighted mean metallicity of the HVCs and the polar gas ring in KGCD are $\log(Z/Z_\odot) \sim -2.4$ and $\log(Z/Z_\odot) \sim -1.7$ respectively, which are 1 – 2 orders of magnitude below HVCs in the MW (e.g. Wakker, 2001; Gibson et al., 2001; Richter et al., 2001). This points to problems with the assumed minimal SNe feedback model.

We conclude that current cosmological simulations can produce MW-size disc galaxies with similar populations of H I HVCs to those in the MW. We demonstrate that in a cosmological context, HVCs appear to be a natural byproduct of galaxy formation in an ΛCDM universe. This study focuses on only two simulated galaxies due to the limit of our computational resources. The differences between these two models, KGCD and AGCD, may demonstrate real differences in the populations of HVCs among disc galaxies. However, to understand the causes of such differences, more samples of high-resolution simulated cosmological disc galaxies would elucidate how common large HVC structures are, and what kind of evolution history is required to make such HVCs. We also emphasise that the assumptions we have made to obtain ionisation fractions, are quite simple. We need to revisit this model with a self-consistent UV background.

Chapter 5

Conclusions and Future Directions

"> Time is nature's way of making sure that everything
> doesn't happen at once.
And space is so that it doesn't all happen to you."

— Matthew L. Martin and John D Salt, *alt.religion.kibology*

5.1 Conclusions

The Λ–dominated Cold Dark Matter (ΛCDM) concordance model refined in Spergel et al. (2003) states that the Universe evolves hierarchically, whereby as the Universe expanded, the smallest Dark Matter (DM) overdensities were the first objects to collapse under their own gravitational influence (White & Rees, 1978; White et al., 1993). These DM perturbations formed the gravitational seeds of the first galaxies, and these gradually collided, forming larger structures which subsequently lead to further collapse. Most of the merger and accretion driven evolution of these objects occurred over a redshift range peaking at $z \sim 2-5$ (Murali et al., 2002), however this thesis shows these events are still ongoing and can still be seen in the local Universe today — in particular, in our own Galaxy, the Milky Way (MW). Throughout this thesis, the cannibalism of smaller objects by the MW has been studied by the use of numerical simulations, to look at both the fate of some of these smaller objects, and indeed, that of our own Galaxy.

Chapter 2: Numerical Simulations

Our simulations use GCD+ (Kawata, 1999, 2001a,b), which models the self-gravity, hydrodynamics, star formation, radiative cooling, supernovae (SNe) feedback and metal enrichment using an adaptive, tree-based Smooth Particle Hydrodynamical (SPH) algorithm. We use GCD+ in both its fully featured mode to yield high-mass resolution (and thus high spatial resolution) simulations of MW-like systems in the ΛCDM Universe, and in a cheaper N-body-only mode, where it is a high-mass, high-time resolution N-body solver used to model the Magellanic Clouds (MCs) interacting with the MW.

To visualise the outputs of these simulations and compare them to the pre-existing observational datasets, we have developed a software package to project the datasets into the observer's plane. In the cosmological simulations where the host galaxy resembles approximately the MW, the observer is taken to be an arbitrary virtual observer. In the Magellanic Stream (MS) simulations, we are able to reproduce the geometry of the MCs by construction, and thus can compare more directly against the observational data.

Chapter 3: N-body Simulations of the Magellanic Stream

We prepare a suite of simulations of the MCs as they are cannibalised by the MW system, using the N-body-only form of GCD+. We compare these simulations directly against newly available data from H I Parkes All-Sky Survey (HIPASS), performing more quantitative comparisons than previous works. We first find the configuration of initial conditions that leads to the optimum reproduction of the MS. We then perform a substantial number of simulations, varying the free parameters on a grid around this fiducial model to highlight the impact that the choice of initial boundary conditions makes on the final stream. We demonstrate which of the unknown parameters are more constrained by the match to the observed data. We find that the Small Magellanic Cloud (SMC) disc, with a scale radius of 3.5 kpc and diameter $\sim$ 7 kpc, was more extended prior to its encounters with the Large Magellanic Cloud (LMC) and MW than was assumed in previous studies such as Gardiner & Noguchi (1996) and Yoshizawa & Noguchi (2003). Models with more strongly concentrated discs are too tightly bound to be stripped of enough gaseous material to form the MS. We find that small differences in the initial orientation of the disc, differing in angles of only 20° influence the stream details significantly.

Since even small differences in the mass of the LMC have a strong bearing on the shape of the SMC orbit, and thus the stream, we refute findings by van der Marel et al. (2002) that the total mass of the LMC is only $9 \times 10^9\,\mathrm{M}_\odot$, and believe the canonical value of $2 \times 10^{10}\,\mathrm{M}_\odot$ (Weinberg, 2000) is more likely if the stream is a result of tidal stripping of the SMC. The range of dynamical friction allowed by our models, $2 \leq \ln(\Lambda) \leq 4.5$, is consistent with Binney & Tremaine (1987) and Hashimoto et al. (2003), and larger ranges of $\ln(\Lambda)$ lead to remarkably different shapes of the stream despite the small changes to the orbit.

Contrasted with these constraints provided by our simulations, we also find parameters that have little or no bearing on the final observable stream properties. The scale height of the SMC disc, the extent of the DM halo, and the final total mass of the SMC (varying the mass of the SMC for the purposes of the orbit calculation) were found to be unimportant to the evolution of the system. Increasing the initial SMC mass to the maximum allowed value of $3.6 \times 10^9\,\mathrm{M}_\odot$ lead to slightly less mass being stripped into the streams, since the SMC particles became more tightly bound to the dwarf. The extent of the DM halo has an effect on the stripped DM, but such changes are unobservable by the nature of DM, and had no effect on the gas stream. Both the velocity dispersion of the SMC disc and the ratio of H I to DM mass of the SMC halo simply scale the velocity dispersion and quantity of H I found in the final Leading Arm Feature (LAF), MS and MCs in a linear fashion.

In many of our models, including the fiducial model, we make the robust finding that the tidal interaction between the LMC and SMC and MW result in spatial and kinematical bifurcations in both the MS and LAF. The spatial bifurcation (both radial and tangential) is apparent in the HIPASS data, and the kinematical bifurcations have subsequently been conclusively observed (Stanimirovic et al., 2008). The tangential bifurcation formed at $T = -1.05\,\mathrm{Gyr}$ in our fiducial model when an impulse was imparted by the LMC onto the MS during an encounter, and the radial bifurcation formed at $T = -0.9\,\mathrm{Gyr}$ when the LMC passed through the LAF. The kinematical bifurcation formed at $T = -0.55\,\mathrm{Gyr}$ when the MS was given an impulse by the LMC at apo-Galacticon. The existence of these predicted bifurcations lend strong support for the tidal disruption origin of the MS. Furthermore, the modelled LAF is found to be very extended in the radial direction, with Galactocentric distances ranging from ~ 20 – $80\,\mathrm{kpc}$. One High Velocity Cloud (HVC) with apparent connection to the LAF is interacting with the Galactic disc at $\sim 17\,\mathrm{kpc}$ (McClure-Griffiths et al., 2008), not inconsistent with our model.

We test our fiducial model with the addition of hydrodynamics and star formation, and find the shape of the MS was largely unchanged, although the details of the stream were poorly matched because of the simplicity of the initial conditions. A more sophisticated treatment of the initial conditions would ensure that they were in equilibrium prior to the start of the simulation, and that no artificial transients caused a premature burst of star formation. A criticism levelled at tidal models in the past is that the H I column density is found observationally to decrease down the length of the MS, with similar behaviour only being seen in ram pressure models. Our hydrodynamical simulation with SNe feedback has this desired feature, a result which has not typically been seen in prior tidal models of the MS. The tip of the MS is found to be more extended than the pure N-body case, and may reflect the tentative observational results of Westmeier & Koribalski (2008).

Despite our improved understanding of the Magellanic and MW system, there are still uncertainties in both the observations and models. Recent refinements have been made to the proper motions of both MCs, and this has lead to authors concluding that the MCs may only be on their first orbit around the MW (Kallivayalil et al., 2006b,a; Besla et al., 2007; Piatek et al., 2008). There are other uncertainties in the orbits however, and a fuller treatment of the orbits would need to explore the effects of uncertain dynamical friction between the MCs themselves, and the MW. It would also be necessary to refine our understanding of the shape of the MW and LMC haloes—whether they are oblate, spherical or prolate (Helmi, 2004a,b; Johnston et al., 2005; Růžička et al., 2007).

Furthermore, high resolution, fully self-consistent hydrodynamical models have yet to be produced. The only work to include both drag and tidal forces is that of Gardiner (1999). Yoshizawa & Noguchi (2003) alternatively included hydrodynamics and star formation, and Li (1999) and Maddison et al. (2002) modelled all three bodies, but with a necessarily reduced resolution. Modelling all of the physics simultaneously introduces too many free parameters, and as such has not yet been performed. A promising method of performing a more complete exploration of this unexplored parameter space may be possible with Genetic Algorithms (GAs). Once a "goodness of fit" is quantified, GAs can be defined to reduce the volume of this parameter space that must be explored (Růžička et al., 2007; Howley et al., 2008).

We show the LAF and MS appear to be predominantly the result of tidal stripping of the SMC by the action of tidal forces exerted from the LMC and MW. Because of their proximity, the LMC and SMC offer unique opportunities to study

the evolution of two galactic systems that will eventually coalesce with the MW. The MS thus represents the closest example of hierarchical clustering in action, as the SMC and LMC are slowly cannibalised by the MW.

Chapter 4: Origin of HVCs in the Milky Way

We analyse two high-resolution, fully self consistent, cosmological simulations of $L_\star$ galaxies resembling the MW within the Local Group (LG) system, and find that HVCs are a natural byproduct of hierarchical clustering within a ΛCDM Universe. We use GCD+ in the more complete mode, solving for the evolution of the gas and stars, as well as DM, and use the same analysis package to project the simulations into the observer's plane from the vantage point of a virtual observer.

From these virtual observations, we find that H I gas clouds resembling the various distributions of Lockman et al. (2002) and Putman et al. (2002) (in flux and in kinematical and spatial distribution, and completely decoupled from stellar or DM clumps) are observed in both of these high-resolution, but otherwise unremarkable MW-like galaxies in ΛCDM simulations. We thus conclude that they are a likely universal phenomena of galaxies, formed by hierarchical clustering within the ΛCDM Universe. We suggest that all such gas-rich galaxies are still in the process of cannibalising smaller gas-rich but DM-poor systems, and indeed this suggestion is backed up by the latest observations of nearby galaxies such as M31 (Thilker et al., 2004; Westmeier et al., 2005a). Our simulations reproduce the different populations of HVCs. Large complexes like Complex C could be explained as a portion of a ring rotating in a near polar orbit. We also find large Very High Velocity Cloud (VHVC) complexes, as well as Compact High Velocity Clouds (CHVCs). Furthermore, the models predict the distributions of other highly ionised species of gas. The sky is predicted to be uniformly covered in H II, C IV, O VI, and O VI. Observations of O VI (Sembach et al., 2003) indicate that 60 – 85% sightlines show O VI and H II absorption to the limits of measurement. Our models predict lower metallicities $-4 \lesssim \log(\mathrm{Z/Z_\odot}) \lesssim -2$, compared to the observed metallicities $-1 < \log(\mathrm{Z/Z_\odot}) < 0$ (Wakker, 2001; Gibson et al., 2001; Richter et al., 2001), possibly because of the minimal SNe feedback model employed.

We find that the majority of high velocity, non-disc H I emission originates closer than 150 kpc (99% of the H I is closer in the KGCD simulation), but that most O VI-rich HVCs form a more distant population in the hot halo, with $100 < r \lesssim 500$ kpc.

These findings are consistent with the limits set of the HVCs in our own Galaxy (Danly et al., 1993; van Woerden et al., 1999; Wakker, 2001; Thom et al., 2006; Wakker et al., 2007; Thom et al., 2007; Wakker et al., 2008), and in other galaxies (Pisano et al., 2004; Thilker et al., 2004; Westmeier et al., 2005a).

We present here the successful modelling of the H I properties of HVCs within two $L_\star$ galaxies that result naturally from a self-consistent cosmological context. One could extend these models by studying the effects of ionisation from a UV background, and by testing a variety of SNe feedback models in a larger mock-catalogue of MW-like galaxies obtained from cosmological simulations.

Bibliography

Aarseth, S. J. 1963, MNRAS, 126, 223

Abadi, M. G., Navarro, J. F., Steinmetz, M., & Eke, V. R. 2003, ApJ, 591, 499

Agertz, O., Moore, B., Stadel, J., Potter, D., Miniati, F., Read, J., Mayer, L., Gawryszczak, A., Kravtsov, A., Nordlund, Å., Pearce, F., Quilis, V., Rudd, D., Springel, V., Stone, J., Tasker, E., Teyssier, R., Wadsley, J., & Walder, R. 2007, MNRAS, 380, 963

Bailin, J., et al. 2005, ApJ, 627, L17

Balsara, D. 1995, Bulletin of the American Astronomical Society, 27, 1362

Barnes, D. G., et al. 2001, MNRAS, 322, 486

Barnes, J., & Hut, P. 1986, Nature, 324, 446

Baugh, C. M., Cole, S., Frenk, C. S., & Lacey, C. G. 1998, ApJ, 498, 504

Beeson, B., Barnes, D. G., & Bourke, P. D. 2003, Publications of the Astronomical Society of Australia, 20, 300

Bekki, K., & Chiba, M. 2005, MNRAS, 356, 680

Bekki, K., Couch, W. J., Beasley, M. A., Forbes, D. A., Chiba, M., & Da Costa, G. S. 2004, ApJ, 610, L93

Ben Bekhti, N., Brüns, C., Kerp, J., & Westmeier, T. 2006, A&A, 457, 917

Bertschinger, E. 2001, ApJS, 137, 1

Besla, G., Kallivayalil, N., Hernquist, L., Robertson, B., Cox, T. J., van der Marel, R. P., & Alcock, C. 2007, ApJ, 668, 949

Binney, J., & Tremaine, S. 1987, Galactic dynamics (Princeton, NJ, Princeton University Press)

Bland-Hawthorn, J., & Maloney, P. R. 1997, Publications of the Astronomical Society of Australia, 14, 59

—. 1999, ApJ, 510, L33

Blitz, L., Spergel, D. N., Teuben, P. J., Hartmann, D., & Burton, W. B. 1999, ApJ, 514, 818

Brüns, C., et al. 2005, A&A, 432, 45

Braun, R., & Burton, W. B. 1999, A&A, 341, 437

Braun, R., & Thilker, D. A. 2004, A&A, 417, 421

Bregman, J. N. 1980, ApJ, 236, 577

Brook, C. B., Kawata, D., Gibson, B. K., & Flynn, C. 2004, MNRAS, 349, 52

Brueck, M. T., & Hawkins, M. R. S. 1983, A&A, 124, 216

Burton, W. B., Braun, R., & Chengalur, J. N. 2001, A&A, 369, 616

Calabretta, M. R., & Greisen, E. W. 2002, A&A, 395, 1077

Carraro, G., Lia, C., & Chiosi, C. 1998, MNRAS, 297, 1021

Cen, R., & Ostriker, J. P. 1993, ApJ, 417, 415

Chiappini, C., Matteucci, F., & Romano, D. 2001, ApJ, 554, 1044

Cole, S., Lacey, C. G., Baugh, C. M., & Frenk, C. S. 2000, MNRAS, 319, 168

Collins, J. A., Shull, J. M., & Giroux, M. L. 2004, ApJ, 605, 216

—. 2005, ApJ, 623, 196

—. 2007, ApJ, 657, 271

Danly, L., Albert, C. E., & Kuntz, K. D. 1993, ApJ, 416, L29+

Davies, R. D., & Wright, A. E. 1977, MNRAS, 180, 71

Davis, M., Efstathiou, G., Frenk, C. S., & White, S. D. M. 1985, ApJ, 292, 371

de Avillez, M. A. 2000, Ap&SS, 272, 23

de Heij, V., Braun, R., & Burton, W. B. 2002, A&A, 392, 417

Dehnen, W. 2001, MNRAS, 324, 273

Dickey, J. M., & Lockman, F. J. 1990, ARA&A, 28, 215

Dieter, N. H. 1965, AJ, 70, 552

Dopita, M. A., Lawrence, C. J., Ford, H. C., & Webster, B. L. 1985, ApJ, 296, 390

Eggen, O. J., Lynden-Bell, D., & Sandage, A. R. 1962, ApJ, 136, 748

Evans, N. W. 1993, MNRAS, 260, 191

Faber, S. M., & Lin, D. N. C. 1983, ApJ, 266, L17

Fang, T., Mckee, C. F., Canizares, C. R., & Wolfire, M. 2006, ApJ, 644, 174

Feast, M. W., & Walker, A. R. 1987, ARA&A, 25, 345

Ferland, G. J., Korista, K. T., Verner, D. A., Ferguson, J. W., Kingdon, J. B., & Verner, E. M. 1998, PASP, 110, 761

Fich, M., & Tremaine, S. 1991, ARA&A, 29, 409

Fox, A. J., Savage, B. D., & Wakker, B. P. 2006, ApJS, 165, 229

Fox, A. J., Savage, B. D., Wakker, B. P., Richter, P., Sembach, K. R., & Tripp, T. M. 2004, ApJ, 602, 738

Fox, A. J., Wakker, B. P., Savage, B. D., Tripp, T. M., Sembach, K. R., & Bland-Hawthorn, J. 2005, ApJ, 630, 332

Gardiner, L. T. 1999, in ASP Conf. Ser., Vol. 166, Stromlo Workshop on High-Velocity Clouds, ed. B. K. Gibson & M. E. Putman (San Francisco: ASP), 292–+, (G99)

Gardiner, L. T., & Noguchi, M. 1996, MNRAS, 278, 191, (GN96)

Gardiner, L. T., Sawa, T., & Fujimoto, M. 1994, MNRAS, 266, 567, (GSF94)

Gibson, B. K., Giroux, M. L., Penton, S. V., Putman, M. E., Stocke, J. T., & Shull, J. M. 2000, AJ, 120, 1830

Gibson, B. K., Giroux, M. L., Penton, S. V., Stocke, J. T., Shull, J. M., & Tumlinson, J. 2001, AJ, 122, 3280

Gill, S. P. D., Knebe, A., & Gibson, B. K. 2004, MNRAS, 351, 399

Gingold, R. A., & Monaghan, J. J. 1977, MNRAS, 181, 375

—. 1983, MNRAS, 204, 715

Gnedin, N. Y. 1998, MNRAS, 294, 407

Gooch, R. 1996, in Astronomical Society of the Pacific Conference Series, Vol. 101, Astronomical Data Analysis Software and Systems V, ed. G. H. Jacoby & J. Barnes, 80–+

Haines, E. 1994, in Graphic Gems IV, ed. P. Heckbert (Morgan Kaufmann), 24–46

Hardy, E., Suntzeff, N. B., & Azzopardi, M. 1989, ApJ, 344, 210

Harris, J., & Zaritsky, D. 2004, AJ, 127, 1531

—. 2006, AJ, 131, 2514

Hashimoto, Y., Funato, Y., & Makino, J. 2003, ApJ, 582, 196

Hatzidimitriou, D., Croke, B. F., Morgan, D. H., & Cannon, R. D. 1997, A&AS, 122, 507

Haud, U. 1988, A&A, 198, 125

Heller, P., & Rohlfs, K. 1994, A&A, 291, 743

Helly, J. C., Cole, S., Frenk, C. S., Baugh, C. M., Benson, A., & Lacey, C. 2003, MNRAS, 338, 903

Helmi, A. 2004a, MNRAS, 351, 643

—. 2004b, ApJ, 610, L97

Hernquist, L., & Katz, N. 1989, ApJS, 70, 419

Holmberg, E. 1941, ApJ, 94, 385

Holweger, H. 2001, in American Institute of Physics Conference Series, Vol. 598, Joint SOHO/ACE workshop "Solar and Galactic Composition", ed. R. F. Wimmer-Schweingruber, 23–+

Houck, J. C., & Bregman, J. N. 1990, ApJ, 352, 506

Howley, K. M., Geha, M., Guhathakurta, P., Montgomery, R. M., Laughlin, G., & Johnston, K. V. 2008, ArXiv e-prints, 804

Hulsbosch, A. N. M. 1978, A&A, 66, L5

Hulsbosch, A. N. M., & Wakker, B. P. 1988, A&AS, 75, 191

Ibata, R. A., Gilmore, G., & Irwin, M. J. 1994, Nature, 370, 194

Indebetouw, R., & Shull, J. M. 2004, ApJ, 605, 205

Iwamoto, K., Brachwitz, F., Nomoto, K., Kishimoto, N., Umeda, H., Hix, W. R., & Thielemann, F.-K. 1999, ApJS, 125, 439

Johnston, K. V., Law, D. R., & Majewski, S. R. 2005, ApJ, 619, 800

Jones, B. F., Klemola, A. R., & Lin, D. N. C. 1994, AJ, 107, 1333

Just, A., & Peñarrubia, J. 2005, A&A, 431, 861

Kalberla, P. M. W., Burton, W. B., Hartmann, D., Arnal, E. M., Bajaja, E., Morras, R., & Pöppel, W. G. L. 2005, A&A, 440, 775

Källander, D., & Hultman, J. 1998, A&A, 333, 399

Kallivayalil, N., van der Marel, R. P., & Alcock, C. 2006a, ApJ, 652, 1213

Kallivayalil, N., van der Marel, R. P., Alcock, C., Axelrod, T., Cook, K. H., Drake, A. J., & Geha, M. 2006b, ApJ, 638, 772

Katz, N. 1992, ApJ, 391, 502

Katz, N., & Gunn, J. E. 1991, ApJ, 377, 365

Katz, N., Weinberg, D. H., & Hernquist, L. 1996, ApJS, 105, 19

Kawata, D. 1999, PASJ, 51, 931

—. 2001a, ApJ, 558, 598

—. 2001b, ApJ, 548, 703

Kawata, D., & Gibson, B. K. 2003a, MNRAS, 340, 908

—. 2003b, MNRAS, 346, 135

Kawata, D., Gibson, B. K., & Windhorst, R. A. 2004, MNRAS, 354, 387

Kay, S. T., Pearce, F. R., Jenkins, A., Frenk, C. S., White, S. D. M., Thomas, P. A., & Couchman, H. M. P. 2000, MNRAS, 316, 374

Kennicutt, Jr., R. C., Bresolin, F., Bomans, D. J., Bothun, G. D., & Thompson, I. B. 1995, AJ, 109, 594

Kerr, F. J., & Lynden-Bell, D. 1986, MNRAS, 221, 1023

King, I. 1962, AJ, 67, 471

Knebe, A., Gill, S. P. D., Kawata, D., & Gibson, B. K. 2005, MNRAS, 357, L35

Kobayashi, C., Tsujimoto, T., & Nomoto, K. 2000, ApJ, 539, 26, (KTN00)

Kodama, T. 1997, Ph.D. Thesis

Kodama, T., & Arimoto, N. 1997, A&A, 320, 41

Komatsu, E., Dunkley, J., Nolta, M. R., Bennett, C. L., Gold, B., Hinshaw, G., Jarosik, N., Larson, D., Limon, M., Page, L., Spergel, D. N., Halpern, M., Hill, R. S., Kogut, A., Meyer, S. S., Tucker, G. S., Weiland, J. L., Wollack, E., & Wright, E. L. 2008, ArXiv e-prints, 803

Kravtsov, A. V. 2003, ApJ, 590, L1

Kravtsov, A. V., Klypin, A., & Hoffman, Y. 2002, ApJ, 571, 563

Kuijken, K., & Dubinski, J. 1994, MNRAS, 269, 13

—. 1995, MNRAS, 277, 1341

Kuilenburg, J. V. 1972, A&A, 16, 276

Larson, R. B. 1974, MNRAS, 166, 585

—. 1976, MNRAS, 176, 31

Lehner, N., Howk, J. C., Keenan, F. P., & Smoker, J. V. 2008, ArXiv e-prints, 801

Li, P. S. 1999, PhD thesis, (University of Wyoming)

Limongi, M., & Chieffi, A. 2003, in From Twilight to Highlight: The Physics of Supernovae, ed. W. Hillebrandt & B. Leibundgut, ESO Astrophysics Symposia (Springer, Berlin), 367–+

Lin, D. N. C., Jones, B. F., & Klemola, A. R. 1995, ApJ, 439, 652

Lin, D. N. C., & Lynden-Bell, D. 1977, MNRAS, 181, 59

—. 1982, MNRAS, 198, 707

Lockman, F. J. 2003, ApJ, 591, L33

Lockman, F. J., Murphy, E. M., Petty-Powell, S., & Urick, V. J. 2002, ApJS, 140, 331

Lu, L., Sargent, W. L. W., Savage, B. D., Wakker, B. P., Sembach, K. R., & Oosterloo, T. A. 1998, AJ, 115, 162

Lucy, L. B. 1977, AJ, 82, 1013

Maddison, S. T., Kawata, D., & Gibson, B. K. 2002, Ap&SS, 281, 421

Makino, J. 1991, PASJ, 43, 859

Maller, A. H., & Bullock, J. S. 2004, MNRAS, 355, 694

Maloney, P. 1993, ApJ, 414, 41

Marquarding, M. 2004, private communication

Martin, N. F., Ibata, R. A., Conn, B. C., Lewis, G. F., Bellazzini, M., & Irwin, M. J. 2005, MNRAS, 362, 906

Mastropietro, C., Moore, B., Mayer, L., Wadsley, J., & Stadel, J. 2005, MNRAS, 363, 509

Mathewson, D. S., Cleary, M. N., & Murray, J. D. 1974, ApJ, 190, 291

Mathewson, D. S., & Ford, V. L. 1984, in Proc. IAU Symp., Vol. 108, Structure and Evolution of the Magellanic Clouds, ed. S. van den Bergh & K. S. D. Boer (Reidel, Dordrecht), 125–136

Mathewson, D. S., Schwarz, M. P., & Murray, J. D. 1977, ApJ, 217, L5

Mathewson, D. S., Wayte, S. R., Ford, V. L., & Ruan, K. 1987, Proceedings of the Astronomical Society of Australia, 7, 19

McClure-Griffiths, N. M., Ford, A., Pisano, D. J., Gibson, B. K., Staveley-Smith, L., Calabretta, M. R., Dedes, L., & Kalberla, P. M. W. 2006, ApJ, 638, 196

McClure-Griffiths, N. M., Staveley-Smith, L., Lockman, F. J., Calabretta, M. R., Ford, H. A., Kalberla, P. M. W., Murphy, T., Nakanishi, H., & Pisano, D. J. 2008, ApJ, 673, L143

Moore, B., & Davis, M. 1994, MNRAS, 270, 209

Muller, E., Staveley-Smith, L., Zealey, W., & Stanimirović, S. 2003, MNRAS, 339, 105

Murai, T., & Fujimoto, M. 1980, PASJ, 32, 581

Murali, C., Katz, N., Hernquist, L., Weinberg, D. H., & Davé, R. 2002, ApJ, 571, 1

Navarro, J. F., & Benz, W. 1991, ApJ, 380, 320

Navarro, J. F., Frenk, C. S., & White, S. D. M. 1997, ApJ, 490, 493

Navarro, J. F., & Steinmetz, M. 1997, ApJ, 478, 13

Navarro, J. F., & White, S. D. M. 1993, MNRAS, 265, 271

Nidever, D. L., Majewski, S. R., & Burton, W. B. 2008, ApJ, 679, 432

Oort, J. H. 1966, Bull. Astron. Inst. Netherlands, 18, 421

Oosterloo, T., Fraternali, F., & Sancisi, R. 2007, AJ, 134, 1019

OpenDX.org. 2003, http://www.opendx.org

Peek, J. E. G., Putman, M. E., & Sommer-Larsen, J. 2008, ApJ, 674, 227

Pfalzner, S., & Gibbon, P. 1997, Many-Body Tree Methods in Physics (Cambridge University Press, Cambridge, UK)

Philip, A. G. D. 1976a, BAAS, 8, 532

—. 1976b, BAAS, 8, 352

Piatek, S., Pryor, C., & Olszewski, E. W. 2008, AJ, 135, 1024

Pisano, D. J., Barnes, D. G., Gibson, B. K., Staveley-Smith, L., Freeman, K. C., & Kilborn, V. A. 2004, ApJ, 610, L17

Press, W. H., & Schechter, P. 1974, ApJ, 187, 425

Putman, M. E., Bland-Hawthorn, J., Veilleux, S., Gibson, B. K., Freeman, K. C., & Maloney, P. R. 2003a, ApJ, 597, 948

Putman, M. E., & Moore, B. 2002, in Astronomical Society of the Pacific Conference Series, Vol. 273, The Dynamics, Structure & History of Galaxies: A Workshop in Honour of Professor Ken Freeman, ed. G. S. Da Costa & H. Jerjen, 195–+

Putman, M. E., Staveley-Smith, L., Freeman, K. C., Gibson, B. K., & Barnes, D. G. 2003b, ApJ, 586, 170

Putman, M. E., Thom, C., Gibson, B. K., & Staveley-Smith, L. 2004, ApJ, 603, L77

Putman, M. E., et al. 1998, Nature, 394, 752

—. 2002, AJ, 123, 873

Quilis, V., & Moore, B. 2001, ApJ, 555, L95

Recillas-Cruz, E. 1982, MNRAS, 201, 473

Richter, P., et al. 2001, ApJ, 559, 318

Růžička, A., Palouš, J., & Theis, C. 2007, A&A, 461, 155

Salpeter, E. E. 1955, ApJ, 121, 161

Schommer, R. A., Suntzeff, N. B., Olszewski, E. W., & Harris, H. C. 1992, AJ, 103, 447

Sembach, K. R., Wakker, B. P., Tripp, T. M., Richter, P., Kruk, J. W., Blair, W. P., Moos, H. W., Savage, B. D., Shull, J. M., York, D. G., Sonneborn, G., Hébrard, G., Ferlet, R., Vidal-Madjar, A., Friedman, S. D., & Jenkins, E. B. 2004, ApJS, 150, 387

Sembach, K. R., et al. 2003, ApJS, 146, 165

Siegel, M. H., Majewski, S. R., Gallart, C., Sohn, S. T., Kunkel, W. E., & Braun, R. 2005, ApJ, 623, 181

Simon, J. D., & Blitz, L. 2002, ApJ, 574, 726

Smecker-Hane, T. A., Cole, A. A., Gallagher, III, J. S., & Stetson, P. B. 2002, ApJ, 566, 239

Sofue, Y. 1994, PASJ, 46, 431

Spergel, D. N., et al. 2003, ApJS, 148, 175

Stanimirović, S., Staveley-Smith, L., Dickey, J. M., Sault, R. J., & Snowden, S. L. 1999, MNRAS, 302, 417

Stanimirović, S., Staveley-Smith, L., & Jones, P. A. 2004, ApJ, 604, 176

Stanimirovic, S., Hoffman, S., Heiles, C., Douglas, K. A., Putman, M., & Peek, J. E. G. 2008, ArXiv e-prints, 802

Steinmetz, M. 1996, MNRAS, 278, 1005

Steinmetz, M., & Mueller, E. 1993, A&A, 268, 391

Sternberg, A., McKee, C. F., & Wolfire, M. G. 2002, ApJS, 143, 419

Sutherland, R. S., & Dopita, M. A. 1993, ApJS, 88, 253

Swaters, R. A., van Albada, T. S., van der Hulst, J. M., & Sancisi, R. 2002, A&A, 390, 829

Tasker, E. J., & Bryan, G. L. 2008, ApJ, 673, 810

Thacker, R. J., Tittley, E. R., Pearce, F. R., Couchman, H. M. P., & Thomas, P. A. 2000, MNRAS, 319, 619

Thilker, D. A., Braun, R., Walterbos, R. A. M., Corbelli, E., Lockman, F. J., Murphy, E., & Maddalena, R. 2004, ApJ, 601, L39

Thom, C., Peek, J. E. G., Putman, M. E., Heiles, C., Peek, K. M. G., & Wilhelm, R. 2007, ArXiv e-prints, 712

Thom, C., Putman, M. E., Gibson, B. K., Christlieb, N., Flynn, C., Beers, T. C., Wilhelm, R., & Lee, Y. S. 2006, ApJ, 638, L97

Timmes, F. X., Woosley, S. E., & Weaver, T. A. 1995, ApJS, 98, 617

Tolstoy, E., Venn, K. A., Shetrone, M., Primas, F., Hill, V., Kaufer, A., & Szeifert, T. 2003, AJ, 125, 707

Tripp, T. M., Wakker, B. P., Jenkins, E. B., Bowers, C. W., Danks, A. C., Green, R. F., Heap, S. R., Joseph, C. L., Kaiser, M. E., Linsky, J. L., & Woodgate, B. E. 2003, AJ, 125, 3122

Tufte, S. L., Wilson, J. D., Madsen, G. J., Haffner, L. M., & Reynolds, R. J. 2002, ApJ, 572, L153

Tully, R. B. 1988, Nearby galaxies catalog (Cambridge and New York, Cambridge University Press)

van den Hoek, L. B., & Groenewegen, M. A. T. 1997, A&AS, 123, 305, (vdHG97)

van der Marel, R. P., Alves, D. R., Hardy, E., & Suntzeff, N. B. 2002, AJ, 124, 2639

van Kuilenburg, J. 1972, A&AS, 5, 1

van Woerden, H., Schwarz, U. J., Peletier, R. F., Wakker, B. P., & Kalberla, P. M. W. 1999, Nature, 400, 138

Wakker, B. P. 1991, A&A, 250, 499

—. 2001, ApJS, 136, 463

Wakker, B. P., Howk, J. C., Savage, B. D., van Woerden, H., Tufte, S. L., Schwarz, U. J., Benjamin, R., Reynolds, R. J., Peletier, R. F., & Kalberla, P. M. W. 1999, Nature, 402, 388

Wakker, B. P., Oosterloo, T. A., & Putman, M. E. 2002, AJ, 123, 1953

Wakker, B. P., & van Woerden, H. 1991, A&A, 250, 509

—. 1997, ARA&A, 35, 217

Wakker, B. P., York, D. G., Howk, J. C., Barentine, J. C., Wilhelm, R., Peletier, R. F., van Woerden, H., Beers, T. C., Ivezić, Ž., Richter, P., & Schwarz, U. J. 2007, ApJ, 670, L113

Wakker, B. P., York, D. G., Wilhelm, R., Barentine, J. C., Richter, P., Beers, T. C., Ivezić, Ž., & Howk, J. C. 2008, ApJ, 672, 298

Wakker, B. P., et al. 2003, ApJS, 146, 1

Wannier, P., & Wrixon, G. T. 1972, ApJ, 173, L119+

Weinberg, D. H., Colombi, S., Davé, R., & Katz, N. 2008, ApJ, 678, 6

Weinberg, M. D. 2000, ApJ, 532, 922

Weiner, B. J., & Williams, T. B. 1996, AJ, 111, 1156

Westmeier, T., Braun, R., & Thilker, D. 2005a, A&A, 436, 101

Westmeier, T., Brüns, C., & Kerp, J. 2005b, A&A, 432, 937

Westmeier, T., & Koribalski, B. S. 2008, ArXiv e-prints, 805

White, S. D. M., Efstathiou, G., & Frenk, C. S. 1993, MNRAS, 262, 1023

White, S. D. M., & Rees, M. J. 1978, MNRAS, 183, 341

Woosley, S. E., & Weaver, T. A. 1995, ApJS, 101, 181, (WW95)

Yepes, G., Kates, R., Khokhlov, A., & Klypin, A. 1997, MNRAS, 284, 235

Yoshizawa, A. 1998, PhD thesis, (Tohoku University)

Yoshizawa, A. M., & Noguchi, M. 2003, MNRAS, 339, 1135, (YN03)

Zaritsky, D., & Harris, J. 2004, ApJ, 604, 167

Zhao, H. 2004, MNRAS, 351, 891